

© 2013 Juan Sebastian Ochoa Munoz

STOCHASTIC MODELING IN COMPUTATIONAL ELECTROMAGNETICS

BY

JUAN SEBASTIAN OCHOA MUNOZ

DISSERTATION

Submitted in partial fulfillment of the requirements  
for the degree of Doctor of Philosophy in Electrical and Computer Engineering  
in the Graduate College of the  
University of Illinois at Urbana-Champaign, 2013

Urbana, Illinois

Doctoral Committee:

Professor Andreas C. Cangellaris, Chair  
Professor Weng Cho Chew  
Professor Jose E. Schutt-Aine  
Assistant Professor Maxim Raginsky

# ABSTRACT

This thesis presents methodologies for the efficient assessment of the impact of statistical variability on the performance of electromagnetic structures and systems. The proposed techniques are based on the Sparse Grid Collocation method which is a more efficient alternative than the standard Monte Carlo method.

The high dimensionality challenge associated with certain stochastic problems, defined in terms of correlated random variables, is alleviated with a random-space dimensionality reduction technique that, in combination with an a-priori sensitivity assessment, results in an accurate technique for the statistical characterization and yield estimation of stochastic electromagnetic systems. Two real-world applications demonstrate the benefits of the proposed methodologies, a pair of interconnects with random cross-sectional parameters, and a band pass microwave filter with randomly positioned loads.

The thesis focuses on methodologies for the assessment of structures exhibiting localized uncertainty, namely random changes in the geometric and material properties occurring throughout the structure under consideration. Among the proposed methodologies, a technique is developed for the stochastic electromagnetic macromodeling of two-dimensional subdomains exhibiting geometric and material uncertainty. The methodology makes use of the theory of polynomial chaos expansion and the concept of a global impedance/admittance matrix relationship defined over a circular surface enclosing the cross-sectional geometry of the domain of interest to construct a stochastic global impedance/admittance matrix boundary condition on the surrounding surface. Such a method is generalized for the broadband response of the random domains through a stochastic model order reduction technique based on the Krylov subspace projection. Numerical examples are used to demonstrate the attributes of the proposed stochastic macromodel to the solution of electromagnetic scattering problems by an ensemble of targets exhibiting

uncertainty.

Macromodeling is also employed for the assessment of signal integrity performance in high-speed interconnect structures exhibiting localized uncertainty. Specifically, two applications are studied for demonstrative purposes, the first one concerns a coaxial cable with a random permittivity profile and the second one, a multiconducting interconnect structure with variability in its routing. In the first case, an effective stochastic homogeneous model of the dielectric permittivity is constructed that is used to quantify the induced distortion of the transmitted signal in terms of a random jitter. In the second signal-integrity application, a methodology based on a passive parametric macromodeling technique is developed for the predictive analysis of the impact of interconnect routing uncertainty on their transmission properties.

The last stochastic application presents an expedient methodology for the predictive analysis of the impact of statistical disorder on the electromagnetic attributes of periodic waveguides. The proposed methodology makes use of ideas from the Anderson localization theory to derive closed-form expressions for the calculation of an effective exponential decay ratio that quantifies the impact of periodicity disorder on the transmission properties of the waveguide. The computational efficiency of the proposed method over Monte Carlo based alternatives is demonstrated through a specific example involving a periodically-loaded parallel plate waveguide.

*To Doménica, my greatest gift*

# ACKNOWLEDGMENTS

There are a number of persons that have contributed directly or indirectly to my Ph.D. studies. I would like to start acknowledging the exceptional guidance of my mentor, Professor Andreas C. Cangellaris. His inspiring motivation has been the key of the success of my studies. I thank him for the unique opportunity he gave me five years ago when he saw that a young foreign exchange student could do great things.

This material is based upon work supported by, or in part by, the US Army Research Laboratory and the US Army Research Office under grant number W911NF-10-1-0269. I would like to thank Dev Palmer for his valuable work managing the financial funds for our projects.

I want to thank Professor Costas Sarris for the fruitful discussions we had while I was a Master's degree student which gave me the insight to start my journey into the research academic world, to Thomas Savarino for his interest in my ideas and his consistent motivation to be a better researcher. Many thanks to Professor Weng-Cho Chew for inspiring me with his lectures to study electromagnetics when I was an undergraduate student and to Professor Jose Schutt-Aine for his interesting lectures on signal integrity, which yielded the foundation of my professional career. Further, thank you to Professors Maxim Raginsky and N. R. Aluru for agreeing to be part of my final defense and preliminary examination committees.

Over these years I have had many colleagues from the Electromagnetics Laboratory at the University of Illinois at Urbana-Champaign that offered me their friendship and accompanied me on my journey. Among them, Prasad Sumant guided me in my first steps of research, Joon Chung walked with me in the discovering of new ideas, Xu Chen provided me with valuable discussions in the final stages of my dissertation, and the professors in the laboratory who showed me the path in my education throughout these years.

I want to express my gratitude to the friends I made in Champaign-Urbana,

Rachel Morgan, Daniel Vivar, Juan Bernal, and many others. Thank you for being my family and making me feel at home.

I would have not been able to go through every single day without the unconditional love and infinite support of my family, specially my parents, Patricio and Silvia. Even though they have been miles away, I have felt their presence every minute in my heart. There are no words to thank them enough. Finally, my gratitude goes to Gabriela for her love, support and, above all, for the most beautiful gift I have ever received. Doménica, my precious love, thank you for being part of my life.

# CONTENTS

<b>LIST OF TABLES</b>	<b>ix</b>
<b>LIST OF FIGURES</b>	<b>x</b>
<b>LIST OF ABBREVIATIONS</b>	<b>xiv</b>
<b>Chapter 1 INTRODUCTION</b>	<b>1</b>
1.1 Motivation and Literature Review . . . . .	1
1.2 Contributions and Organization . . . . .	8
<b>Chapter 2 STOCHASTIC COLLOCATION</b>	<b>12</b>
2.1 Introduction . . . . .	12
2.2 Formulation . . . . .	13
2.3 Univariate Interpolation . . . . .	13
2.4 Multivariate Interpolation . . . . .	14
2.5 Numerical Example . . . . .	18
2.6 Concluding Remarks . . . . .	23
<b>Chapter 3 RANDOM-SPACE DIMENSIONALITY REDUCTION TECHNIQUE AND YIELD ESTIMATION</b>	<b>24</b>
3.1 Introduction . . . . .	24
3.2 Formulation . . . . .	25
3.3 Numerical Applications . . . . .	33
3.4 Concluding Remarks . . . . .	39
<b>Chapter 4 STOCHASTIC MACROMODELING</b>	<b>41</b>
4.1 Introduction . . . . .	41
4.2 Stochastic Macromodeling . . . . .	43
4.3 Solution of the Exterior Stochastic BVP . . . . .	47
4.4 Numerical Validation and Demonstration Studies . . . . .	48
4.5 Concluding Remarks . . . . .	54
<b>Chapter 5 STOCHASTIC REDUCED-ORDER MACROMODELING</b>	<b>55</b>
5.1 Introduction . . . . .	55

5.2	Deterministic Transition Matrix . . . . .	56
5.3	Multiple Scatterers . . . . .	60
5.4	Model Order Reduction . . . . .	64
5.5	Stochastic Transition Matrix with Model Order Reduction . . . . .	65
5.6	Numerical Studies . . . . .	71
5.7	Concluding Remarks . . . . .	77
<b>Chapter 6 STOCHASTIC SIGNAL INTEGRITY</b>		
<b>ANALYSIS OF INTERCONNECTS</b>		<b>78</b>
6.1	Introduction . . . . .	78
6.2	Proposed Methodology . . . . .	79
6.3	Case Study 1: Transmission Lines with Random Permittivity Profiles . . . . .	80
6.4	Case Study 2: Interconnect Routing Variability . . . . .	89
<b>Chapter 7 MODELING OF DISORDERED PERIODIC</b>		
<b>WAVEGUIDES</b>		<b>100</b>
7.1	Introduction . . . . .	100
7.2	Quantification of Uncertainty in Input Parameters . . . . .	104
7.3	Diffusion Model for Density Estimation . . . . .	106
7.4	Electromagnetic Model for Uncertainty Propagation . . . . .	108
7.5	Validation Studies . . . . .	114
7.6	The Case of Multiple Random Variables . . . . .	116
7.7	Concluding Remarks . . . . .	119
<b>Chapter 8 CONCLUSIONS</b>		<b>122</b>
8.1	Future Work . . . . .	125
<b>Appendix A INTEGRAL EQUATION SOLVER</b>		<b>128</b>
<b>Appendix B CROSS ENTROPY ALGORITHM</b>		<b>130</b>
<b>Appendix C LOCALIZATION TECHNIQUE FOR</b>		
<b>ONE-DIMENSIONAL PERIODIC STRUCTURES</b>		<b>132</b>
C.1	Small Reflections . . . . .	133
C.2	Moderate Reflections . . . . .	134
<b>BIBLIOGRAPHY</b>		<b>136</b>

# LIST OF TABLES

2.1	Relative percentage error of the mean and standard deviation of the radiation cross section integrated over the angle $\phi$ for the stochastic collocation approach with respect to Monte Carlo simulation for different accuracy levels, $k$ , for the case of TM polarization. . . . .	23
2.2	Relative percentage error of the mean and standard deviation of the radiation cross section integrated over the angle $\phi$ for the stochastic collocation approach with respect to Monte Carlo simulation for different accuracy levels, $k$ , for the case of TE polarization. . . . .	23
3.1	Correlation function $\Sigma$ of the normalized input parameters for a coupled stripline structure. . . . .	34
3.2	Simulation results for a coupled stripline structure. . . . .	35
3.3	Calculation of yield for a maximum peak crosstalk voltage. . . . .	37
3.4	Correlation function $\Sigma$ of the normalized parameters in the geometry definition of a bandpass filter ( $i = 1, 2, \dots, 6$ ). . . . .	38
3.5	Simulation results of the interpolation of the band-pass filter. . . . .	39
3.6	Calculation of yield for a maximum bandwidth of 1.05 and 1.07 GHz. . . . .	39

# LIST OF FIGURES

2.1	Radiation cross section (RCS) for TMz polarization (up) and TEz polarization (bottom) for a dielectric cylinder with random boundary given by $\rho(\chi_2, \chi_3; \phi) = \rho_o + \chi_2 \cos(2\phi) + \chi_3 \sin(2\phi)$ and permittivity $\varepsilon_r = 5(1 + \chi_1)$ . Gaussian random variables, $\chi_{1,2,3}$ have zero mean and variance 0.025. The error bars have a length of $\pm \text{std}$ , where std is the standard deviation of the RCS. The operation frequency is 0.2 GHz. The stochastic collocation approach is compared with Monte Carlo simulation as well as the calculated RCS from a cylinder defined by the mean-value parameters of the random variables.	22
3.1	For a Monte Carlo simulation (a), the full-wave solver needs to be evaluated for a large number of samples so that the PDF of the output can be estimated, while with stochastic collocation (b), a set of prescribed nodes is evaluated with the solver and an interpolation constructed and used to sample the random space to calculate the statistics of the output. . . . .	29
3.2	Process flow of the proposed methodology. . . . .	33
3.3	Cross-sectional geometry of the coupled stripline interconnect structure, showing the input parameters, assumed to be random Gaussian variables, with mean values and standard deviations as shown in the table. The units of the parameters that define the geometry are mm.	34
3.4	Probability density function of the peak cross-talk voltage of the full-order and three reduced-order systems obtained through (a) regular PCA and (b) PCA with sensitivity assessment. . . . .	36
3.5	Geometry of the bandpass filter. The model and dimensions were obtained from [1]. . . . .	37
3.6	Calculated scattering parameters for various realizations of the structure obtained via sampling of reduced input random space. . . . .	38

3.7	Comparison of the calculated probability density function of the bandpass filter bandwidth using the full-order model and reduced models of different dimensions generated through PCASA. . . . .	39
4.1	Reference geometry for the discussion of the concept of stochastic macromodeling. . . . .	43
4.2	Mean value of the magnitude of the scattered magnetic field. Error bars represent $\pm 3$ std deviation from the mean. . .	49
4.3	Array of four PEC elliptical cylinders with random axes lengths and random positions. . . . .	50
4.4	Mean value of the magnitude of the scattered magnetic field on a circle of radius 3.8 m enclosing the four cylinders. Error bars represent $\pm 3$ std deviation from the mean. . . . .	52
4.5	Mean value of the radiation cross section (RCS) of the magnetic field. Error bars represent $\pm 3$ std deviation from the mean. . . . .	52
4.6	Magnitude of the scattered electric field on a circle of radius 3.4 m. Error bars represent $\pm 3$ std deviation from the mean. . . . .	53
4.7	Mean value of the magnitude of the far electric field at $\rho = 1000/k_o$ . Error bars represent $\pm 3$ std deviation from the mean. . . . .	53
5.1	Geometry of scatterer. Scattering boundary condition is computed on contour $c$ . . . . .	57
5.2	Two scatterers in the presence of an incident field. . . . .	62
5.3	Geometry of the studied problem. The field is sampled at the position (0,1) m. . . . .	73
5.4	Monte Carlo simulation based on the analytical Mie scattering solution is compared to the <i>augmented system</i> approach of the first- and second-order and the <i>direct interpolation</i> approach. The field has been sampled at $\phi = \pi$ , $\rho = 1$ m. . . . .	74
5.5	Setup of the line source simulation. The PEC circular cylinder has a random radius and the line source is located at the position (3,0) m. . . . .	75
5.6	The simulation results of the problem to the scattering problem depicted in Fig. 5.5, obtained with the direct interpolation stochastic macromodeling and Monte Carlo solution of the analytical Mie series. The plots show the mean value (top) and standard deviation (bottom) of the $z$ -component of the scattered electric field sampled at (0,1) m with respect to the normalized wavenumber. . . . .	75

5.7	Geometry of two PEC circular cylinders each with a random radius, given by $\rho_i = 0.5(1 + \chi_i)$ , for $i = 1, 2$ and $\chi_i \sim \mathcal{N}(0, 0.1)$ . The separation distance between the centers of the cylinders is $d_{12} = 2.4$ m and the radius of the artificial boundaries is $\rho_o = 1$ m. The cylinders are impinged by a plane wave with amplitude 1 V/m directed along the $x$ -axis. . . . .	76
5.8	Radiation Cross Section (RCS) of two random cylinders with error bars representing $\pm 3$ std deviation from the mean value. The centers are 2.4 m apart and the frequency is 118 MHz. . . . .	77
6.1	Transmission lines exhibiting random variability in the permittivity along the longitudinal axes. . . . .	80
6.2	Proposed homogeneous stochastic model. . . . .	81
6.3	Transmission line discretized in sections with uniform permittivity. . . . .	82
6.4	First four principal components of the permittivity profile along the transmission line. . . . .	83
6.5	Far-end voltage samples for a number of Monte Carlo realizations of a lossless coaxial cable. The distortion in the line is manifested in terms of a random deviation of the time delay, $\Delta t$ . . . . .	86
6.6	Probability density function of the deviation of the time delay induced due to the variability in the permittivity of the line. The methodology based on stochastic collocation is compared with Monte Carlo simulation. . . . .	87
6.7	Standard deviation of the jitter as a function of (a) correlation length and (b) variance of the permittivity. . . . .	88
6.8	Proposed design flow of PCB boards in [2]. Our methodology intends to predict the behavior of the board to provide guiding in the design rules of the board. . . . .	90
6.9	Longitudinal view of a section of a planar interconnect structure consisting of two signal traces. Uncertainty in routing is defined in terms of the displacement of the $x$ coordinate of each of the two end points of the bottom wire. . . . .	92
6.10	Cross section of a coupled microstrip line. . . . .	92
6.11	Calculated mean value and standard deviation for the near-end and far-end voltages of the unperturbed line using Approach A (top) and Approach B (bottom). . . . .	98
6.12	Probability density of the far-end voltage at the middle point of the pulse width. . . . .	98
7.1	Examples of disorder in periodic waveguides. . . . .	101
7.2	Disordered array of silver nanoparticles. . . . .	101

7.3	Statistical disorder induced in the longitudinal position of the 10 middle spheres (up). Electric field sampled at (20 nm,0,z). Error bars have a height of two std( E ) (down). . . .	102
7.4	Statistical disorder induced in the transverse position of the 10 middle spheres (up). Electric field sampled at (20 nm,0,z). Error bars have a height of two std( E ) (down). . . .	103
7.5	(a) Longitudinal cross section of a disordered periodic parallel-plate waveguide. (b) The disorder is caused by a random perturbation in the length of the unit cell. . . . .	105
7.6	Estimated PDF obtained using a diffusion-mixing based estimator and KDE using as input 30 randomly chosen samples that follow a Gaussian distribution. . . . .	108
7.7	Localization factor for the periodic structure of Fig. 7.5, due to a random perturbation in the length of the unit cell following a Gaussian distribution of zero mean and standard deviation of std = 0.05. . . . .	116
7.8	Simulation times of a MATLAB code running in a 2.50 GHz Xeon CPU machine per frequency point for chains of 5, 4, 3 and 1 unit cells as a function of the sparse grid algorithm accuracy. . . . .	117
7.9	Perturbation in the imaginary part of the propagation constant per unit cell for the periodic structure of Fig. 7.5, due to a random perturbation in the length of the unit cell following a Gaussian distribution of zero mean and standard deviation of value std = 0.01, 0.05, and 0.1. . . .	117
7.10	The case of a unit cell with two sources of disorder, namely, the width and the thickness of the <i>y</i> -directed conducting strips. . . . .	118
7.11	Real part of propagation constant per unit cell for the disordered structure of Fig. 7.10 involving two sources of random disorder. . . . .	119
7.12	Imaginary part of the change in the propagation constant per unit cell for the disordered structure of Fig. 7.10 involving two sources of random disorder. . . . .	120
C.1	Schematic representation of reflections in the <i>n</i> -th cell due to perturbation. . . . .	132

# LIST OF ABBREVIATIONS

ASGC	Adaptive Sparse Grid Collocation
BVP	Boundary Value Problem
CAD	Computer Aided Design
CE	Cross Entrophy
CEM	Computational Electromagnetics
EM	Electromagnetic
EMI	Electromagnetic Interference
EMC	Electromagnetic Compatibility
FD	Finite Difference
FDTD	Finite Difference Time Domain
FE	Finite Element
FEM	Finite Element Method
HDMR	High Dimensional Model Representation
IFFT	Inverse Fast Fourier Transform
KDE	Kernel Density Estimation
MC	Monte Carlo
MISE	Mean Integrated Squared Error
MLCV	Maximum Likelihood Cross Validation
MOR	Model Order Reduction
NTL	Non-uniform Transmission Line

PC	Polynomial Chaos
PCA	Principal Component Analysis
PCASA	Principal Component Analysis with Sensitivity Analysis
PCB	Printed Circuit Board
PDF	Probability Density Function
PEC	Perfec Electric Conductor
RCS	Radiation Cross Section
RE	Relative Error
RSM	Response Surface Model
RV	Random Variable
SC	Stochastic Collocation
SGC	Sparse Grid Collocation
SI	Signal Integrity
STD	Standard Deviation
TE	Transverse Electric
TEM	Transverse Electromagnetic
TM	Transverse Magnetic

# Chapter 1

## INTRODUCTION

### 1.1 Motivation and Literature Review

The field of Computational Electromagnetics (CEM) has reached a high level of maturity due to the astonishing development of digital computers and breakthroughs in fast numerical algorithms [3]. As a matter of fact, the theory of Maxwell equations has been well known for over a century [4] and its understanding has led to the accurate solution of well-defined deterministic numerical problems in reasonable simulation times. Besides, domain decomposition methods and parallel programming techniques [5], popularized in the last decade, allow further speed up in electromagnetic (EM) simulations. Such advances have played an important role in the boom of computer industry [6], the development of military applications, the invention of imaging techniques, and the construction of wireless and radio communication systems, among many others. For example, the characterization and design of high-speed interconnects and the quantification of electromagnetic interference (EMI) effects require accurate and fast methodologies that provide the electromagnetic assessment of the circuits and systems under consideration. Even though important statistical EM applications and techniques have been developed in the topics of scattering from rough surfaces, wave propagation in random media [7], and large random cavities, much of the existing computational machinery is not meant to take into consideration the manufacturing-induced variability and/or the uncertainty raised by the lack of detailed information of the structure under consideration. Hence, we see the opportunity for the development of efficient statistical techniques that, if possible, are compatible with commercially available EM solvers and are capable of assessing the impact of uncertainty in the electromagnetic response of electronic systems. Some of the ideas that have led to the development

of the aforementioned statistical applications motivate the stochastic CEM applications proposed in this dissertation.

### 1.1.1 Manufacturing-Induced Variability

The increasing tendency of industry toward miniaturization and complexity of electronic systems results in unintended manufacturing-induced defects in the geometry and material properties of devices, structures, and systems that are manifested in the reduction of production yield. The predictive assessment of the impact of such uncertainty to inform and guide the mitigation of performance and reliability problems requires fast algorithms to comprehend the statistical component of the electromagnetic problem.

One of the most common practices in dealing with manufacturing-induced uncertainty is to rely upon the investigation of the "corner" cases of the pertinent design space. This entails the analysis of the structure for the extreme values in the ranges of the input parameters. This rudimentary approach attempts to provide some insight about the electromagnetic response of the structure and, thus, provide guidance to remedy problematic cases by either adjusting the design or by demanding better tolerances from the manufacturer, which often results in higher costs. Clearly, such an approach does not provide any meaningful answer for the statistical characterization of the performance of electronic systems. On the other hand, the rigorous mathematical method to tackle this type of problems is the Monte Carlo (MC) method. Such method proposes the random generation of samples of the input parameters that follow a certain distribution, then the computer model (EM solver) evaluates the output for the set of samples and its histogram and corresponding probability density function (PDF) and moments are estimated (see Fig. 3.1-(a)). The major disadvantage of MC, however, is the convergence that goes as the inverse square root of the number of simulations, thus requiring a large number of samples to obtain reliable results. Considering that electromagnetic simulations of realistic structures are computationally expensive, the hinderance of such an approach is obvious. Alternatively, an efficient Stochastic Collocation (SC) method based on the Smolyak algorithm [8] that has been broadly researched over the years (e.g., [9, 10, 11, 12, 13, 14, 15]) is employed and described in Chapter 2. The

method is based on multivariate interpolation and it uses an EM solver to simulate the structure for a given grid of nodes in the random space and, next, an interpolation of the response is constructed with a given set of basis functions that can be used to obtain the PDFs of the output parameters and their corresponding statistical moments.

### 1.1.2 Lack of Detailed Information

The EM analysis of increasingly complex electronic systems and structures requires the corresponding geometric information, material specifications and definitions of ports and sources. These specifications, however, might not be available at every step of the design process or, even more, they might not be easily obtained due to the high complexity of the system under consideration. Under these circumstances, the lack of a complete deterministic information in the definition of a structure for modeling/simulation, can be viewed as a source of uncertainty in the definition of the pertinent EM boundary value problem (BVP). A clear example of EM structures that present uncertainty due to the lack of information are large cavity structures where electromagnetic interference (EMI) and compatibility (EMC) applications need to account for the uncertainty raised by the partially available information. It is of particular importance to obtain the average effects and probabilities of failure of systems inside random structures like aircraft cavities [16]. That is why the methods associated with electromagnetic fields in cavities have been extensively explored in the literature and some of them have been compiled in books like *Electromagnetic Fields in Cavities* by Hill [17].

In the area of random cavities, reverberation chambers have been extensively used for emissions and immunity measurements and due to the high sensitivity of the fields with respect to the operation frequency and geometric parameters only statistical techniques are appropriate to characterize its electromagnetic behavior [17]. Over the years, a few authors have tackled the problem of the sensitivity of cavity fields from a statistical perspective [18, 19, 20, 21, 22]. Among them, Lehman [23] and Price [24] derived statistical models of the electromagnetic field variables in complex cavities and the topic has been studied by Hill [25, 26] with a plane wave integral representation of the fields where variability has been introduced through the

plane-wave coefficients that are assumed to be random variables.

The idea of treating uncertainty induced by the lack of information in large cavities can be used in other contexts where deterministic solutions have traditionally been employed. Specifically, we propose an efficient statistical assessment of the impact of uncertainty in the routing of printed circuit board (PCB) interconnects that, in their early design stages, the layout specificity is usually lacking.

### 1.1.3 Problem of High Dimensionality of Random Spaces

Efficient alternatives based on the stochastic collocation method have been used in a variety of electromagnetic problems to assess the impact of the variability in the EM response of the corresponding system. They include response surface modeling (RSM) [27, 28] that has been incorporated in the design process to account for manufacturing variability [29, 30, 31, 27]. Xiu [32, 13, 14] has proposed a mathematical foundation of sparse grid collocation for differential equations with random input parameters. Klimke [15, 33] developed an interpolation MATLAB<sup>®</sup> tool [34] based on the sparse grid interpolation scheme that makes use of an adaptive scheme [35] to sample the random space in an efficient way. Ghanem and Spanos [36] proposed to expand mechanical fields in terms of a set of orthogonal polynomials in the context of the finite element method (FEM). Such a technique, known as polynomial chaos expansion (PC) has been broadly employed in signal integrity modeling applications by Stievano [37], Manfredi [38, 39], and Rong [40], among others. Heiss [41] developed a quadrature rule toolbox that has been used in this dissertation for the calculation of the statistical moments. The SC-based methods aim at reducing the computational cost of traditional Monte Carlo by finding an approximate model of the desired output response over the space defined by the random input parameters. This approximate model lends itself to faster statistical analysis of the desired outputs. However, despite their success, the high dimensionality of the input random space for some of the problems of interest remains as a major bottleneck because the number of simulations grows exponentially with the number of dimensions in the case of tensor product grids and polynomially in the case of sparse grids [13]. While the adaptive sparse grid collocation method (ASGC) reduces

the number of necessary simulations [35] by selectively sampling the random space in an efficient way, the number of sampling points needed may still be quite large for the case of problems with a high-dimensional input random space. The high-dimensional model representation (HDMR) approach has been presented as a promising remedy to this problem [42], by representing the output as a hierarchical correlated function of the input parameters, cast in terms of an expansion from lower-order to higher-order components. Its success relies upon the assumption that the statistical behavior of the output of a physical system is primarily influenced by the first few lower-order terms in the expansion [42].

In this dissertation, another approach is proposed for reducing the dimension of the input random space and thus the number of simulations necessary for obtaining the statistics of the output response. We call this method Principal Component Analysis with Sensitivity Assessment (PCASA) and it constructs a new, reduced random space by taking into account not only the interdependencies of the input random variables but also the sensitivity of the output response on each one of the input random variables. Next, ASGC is used to sample the reduced space and obtain an interpolation of the output in terms of the reduced-space parameters. In this way, the number of simulations is considerably reduced.

#### 1.1.4 Benefits of Macromodeling in Stochastic EM Simulation

The problem of electromagnetic modeling of structures that exhibit randomness is one of significant interest to the EM community because of its relevance to several application domains such as remote sensing, EMI/EMC in electronic systems, and EM wave propagation in random media [43]. For the case of EM wave scattering by composite random structures the complexity of a Monte Carlo or stochastic collocation numerical solutions are compounded by the need to generate a discrete numerical model for each one of the geometries resulting from the sampling of the multidimensional random space defining the randomness of the structure. For example, in the context of the finite element solution of the EM boundary value problem (BVP), a new finite element grid needs to be generated for each one of the realizations of the geometry during the sampling of the random space. This

can be even more challenging for the case of multi-scale structures with fine details and intricate geometries. A way to simplify the statistical simulation is to construct a fixed macromodel boundary condition surrounding portions of linear, passive EM structures that exhibit geometric and/or material uncertainty and that can replace the uncertain object in a way that the need of meshing the entire structure in each iteration of the statistical simulation is avoided.

For the purpose of this thesis, EM scattering problems by a group of targets, some of which present uncertainty is considered. Electromagnetic scattering by targets exhibiting uncertainty has been previously studied with the use of the stochastic collocation method by Chauviere [44] and Zeng [45]. Alternatively, a methodology, based on macromodeling [46, 47] as an efficient framework to analyze the stochastic response of targets exhibiting uncertainty is explored. Specifically, parametric macromodeling [48] is used as a means to develop an interpolation of the macromodel in a given parametric space. Such techniques have been studied in detailed in recent years by Ferranti [49, 50] in the context of signal integrity. In addition, El-Moselhy [51] has developed a reduced-order macromodeling technique for the characterization of interconnects presenting variability, Sumant [52] used an FEM-based reduced-order macromodeling technique to take into account the uncertainty in micro electromechanical systems (MEMS), and Vande Ginste [53] employed a stochastic macromodeling technique to capture the dependencies of the state-space representation matrices with the input random parameters for on-chip interconnects stochastic applications. While those approaches are frequency-domain based, Zadehgol [54] published a work on stochastic electromagnetic time-domain macromodels.

In this thesis, a macromodeling methodology is proposed as a means to alleviate the repeated discretization of the computational domain in the numerical solution of the stochastic EM BVP. The proposed methodology makes use of the mathematical framework of polynomial chaos expansions [55] and SC. These are combined with the concept of network matrix representation of passive EM structures to develop a compact stochastic impedance (or admittance) matrix macromodel on a fixed boundary enclosing each one of the domains that exhibits randomness.

### 1.1.5 Global vs. Localized Variability

A stochastic problem can be recognized as either exhibiting global or localized uncertainty. Global uncertainty is understood as the uniform variability of random parameters from one structure to the next such that they are kept constant within each single structure. On the other hand, this dissertation focuses on problems with localized uncertainty, defined as the statistical variability of geometric and material parameters throughout the structure itself. Examples of EM statistical problems with local variability are wave propagation in random media like atmosphere, oceans, and biological tissue, scattering from random surfaces and the assessment of disordered periodic structures [43, 56]. They have attracted significant attention from the scientific community due to their importance in fields like telecommunication systems. For instance, Ishimaru [7] has worked extensively in wave propagation and scattering in random media, statistical models for characterization of indoor multi-path propagation has been proposed by Spencer [57] and more recently, the topic of propagation of laser beams in random media has been explored [58].

In like manner, the topic of scattering by rough surfaces is extensively rich and of importance in surface physics, remote sensing and radar data interpretation where the feature granularity size is in the order of the wavelength [59]. Many authors have devoted their research to the study of scattering from rough surfaces [60, 56, 61, 62, 63]. Among those, Mendez [64], Kim [65], and Ishimaru [66] studied the occurrence of backscattering enhancement by random rough surfaces like the case of the moon that is brighter at the full-moon stage. Wagner [59] used a Monte Carlo simulation in combination with a fast multipole method to compute the scattering of an EM wave from a two-dimensional rough surface. Li [67] used a finite difference time domain (FDTD) method for the investigation on two-dimensional rough surfaces, and Lai [68] proposed a two-dimensional domain-decomposition FDTD method to simulate wave scattering by rough surfaces. An additional application of the study of rough surfaces is the quantification of the power absorption of roughness induced in printed circuit boards (PCBs) interconnects to promote adhesion. The effect of surface roughness on the current losses has been studied by Morgan [69]. Hammerstad [70] proposed an empirical formula for calculating the power absorption enhancement factor based on Morgan's re-

sult that has been verified with the use of numerical methods [71]. This theory has evolved over the years and Tsang [72] proposed a model that calculates the roughness-induced absorption with the use of a second-order small perturbation method. Such theory has been extended to 3D [73] and the propagation loss in interconnects has been well predicted for measured surface profile data [74, 75, 76, 77].

In this thesis, we consider the problem of disordered periodic structures. This topic is of particular importance due to the degradation caused by the manufacturing-induced statistical disorder on the transmission properties of periodic structures like arrays of nanoparticles, a promising reconfigurable waveguide application in the optical regime. The effects of such disorder need to be quantified in order to obtain realistic simulations that agree with measurements that often differ from the theoretical predictions [78]. The proposed methodology is based on the localization theory proposed by Anderson [79] which has been popularized in the solid state community. The theory predicts an effective decay in the propagating modes as a result of the multiple reflections that the wave encounters as it travels through a disordered periodic structure. Kissel [80, 81] utilized Anderson's concepts to study disordered periodic mechanical structures and proposed a small-disorder expression to account for disorder. Cai [82] proposed a methodology that takes into account the multiple reflections between adjacent unit cells to approximate the impact of disorder in the transmission properties of periodic structures. In earlier studies [83], it has been demonstrated how this technique can be used to analyze the effects of statistical material/geometric disorder in the electromagnetic properties of transmission-line based metamaterial structures, where only lumped circuit elements and transmission-lines structures are employed to calculate the impact of uncertainty in metamaterial devices.

## 1.2 Contributions and Organization

The collection of stochastic applications are a sample of potential research opportunities in the stochastic modeling field. In fact, by incorporating sophisticated statistical tools to treat typical computational electromagnetic problems, one can identify a great number of opportunities that will be discussed in forthcoming chapters. The present dissertation shows the potential

in this area and the importance of considering stochastic problems for the CEM community, not only to treat uncertainties from manufacturing processes but also to deal with complexity in stages of design when complete deterministic information is not available. The statistical tools employed in this document can be used to solve a variety of problems from nanotechnology to electromagnetic compatibility applications. This thesis is an attempt to motivate the usefulness of these tools and show how we can benefit from advances in stochastic modeling and statistical analysis, as well as ideas practiced in other engineering fields in solving efficiently complex electromagnetic problems and problems exhibiting uncertainty and randomness.

Chapter 2 presents the formulation of the sparse grid stochastic collocation based on Smolyak algorithm and demonstrates the advantages of using this technique over traditional Monte Carlo through a simple scattering problem.

In Chapter 3, a methodology is presented for the expedient statistical analysis of the electromagnetic attributes of passive microwave structures exhibiting manufacturing uncertainty in geometric and material parameters. In the proposed approach, the computational complexity stemming from the high dimensionality of the random space that is often necessary to describe such uncertainty is mitigated by employing a principal component analysis [84] with sensitivity assessment in combination with an adaptive sparse grid collocation scheme. The method exploits the inherent dependencies between random parameters to reduce the number of simulations needed to extract the statistics of the desired output response. This leads to the expedient estimation of production yield by means of the cross-entropy (CE) algorithm, which provides for fast calculation of the failure probability for a given functionality criterion. The proposed methodology is demonstrated through its application to the analysis of crosstalk in coupled microstrip lines exhibiting uncertainty in their cross-sectional dimensions and material properties and the bandwidth characteristics of a bandpass filter in the presence of uncertainty.

A methodology for the development of stochastic electromagnetic macro-models for domains exhibiting geometric and material uncertainty is presented in Chapter 4. Focusing on the EM scattering problem and the case of domains in the structure under investigation exhibiting geometric/material invariance along one of the axes of the reference coordinate system, the methodology proposes the use of the theory of polynomial chaos expansion

and the concept of a global impedance/admittance matrix relationship defined over a circular surface enclosing the cross-sectional geometry of the domain of interest to construct a stochastic boundary condition, defined on the enclosing circular surface, whose elements are truncated polynomial chaos expansions over the random space defined by the random variables that parameterize the geometric and material uncertainty inside the domain. Use is made of sparse Smolyak grids to reduce the computational cost of constructing the stochastic macro-model. Numerical examples are used to demonstrate some of the attributes of the proposed stochastic macro-models to the numerical solution of electromagnetic scattering problems by an ensemble of cylindrical targets exhibiting uncertainty in their shape and relative positioning.

In Chapter 5 the ideas presented in Chapter 4 are extended to enable computationally efficient prediction of the broadband response of the random system by employing a Krylov subspace model order reduction scheme [85]. It is shown that the proposed approach is more accurate than previously published schemes [86, 87]. Furthermore, the method is employed to treat multiple scatterers with the use of the transition matrix formulation that enables the EM scattering solution by an ensemble of random targets can be simulated with no need of meshing the surrounding media when the media is homogeneous.

Next, new ideas for stochastic electromagnetic modeling pertinent to signal integrity applications are presented in Chapter 6. Specifically, a computer model is proposed for the fast predictive analysis of the impact of interconnect variability in its routing and electrical properties profiles. Through the use of a parametric macromodel of the interconnect structure and rational function interpolation in the frequency domain, the proposed model propagates structure variability described in terms of a set of properly defined random variables to broadband, stochastic scattering parameters for the transmission channel. In this manner, an efficient Monte Carlo analysis can be performed for the prediction of the statistics of the transient response of the channel due to local uncertainty.

In Chapter 7, the important class of periodic electromagnetic problems exhibiting disorder is studied. An efficient methodology is presented for the fast electromagnetic analysis of the impact of statistical disorder on their transmission properties. The proposed methodology makes use of ideas from

the Anderson localization theory to derive closed-form expressions for the calculation of an effective exponential decay ratio that quantifies the impact of periodicity disorder on the transmission properties of the waveguide. With regard to the quantification of the statistics of periodicity disorder from data obtained from a limited number of manufactured devices, a nonparametric probability density estimation process is examined and found to be satisfactory for our purposes. The computational efficiency of the proposed method over brute-force Monte Carlo based alternatives is demonstrated through specific examples involving a periodically-loaded parallel plate waveguide. Furthermore, this numerical study is used to examine the accuracy of calculating the overall change in the propagation constant of the structure due to several sources of disorder as the sum of the changes calculated with each one of the sources of disorder considered individually.

Chapter 8 concludes with a summary of the contributions and ideas for future work.

# Chapter 2

## STOCHASTIC COLLOCATION

### 2.1 Introduction

Maxwell equations describe the physics of electromagnetism and, along with appropriate boundary conditions and excitations, they can be used to obtain analytical or numerical solutions for the resulting electromagnetic fields for a wide variety of practical applications. In this chapter, we describe the statistical tools that are chosen for the purposes of this work to take into account the random variability in electrical properties and geometry of structures under consideration.

More specifically, the method used is the stochastic collocation approach. This method is an alternative to the traditional Monte Carlo method and, roughly speaking, it is aimed at the interpolation of the output in terms of the random input parameters by appropriately sampling the random space. Then, the interpolation is employed in the statistical assessment of our output of interest. This technique is a non-intrusive methodology in the sense that its application does not require modification of the EM solver. The way the random space is sampled is dictated by the Smolyak algorithm. More specifically, we rely on the mathematical theory presented by Xiu [13] to implement the Sparse Grid Collocation scheme used to propagate input uncertainty to output response. Although much attention has been devoted to its application, the derivation of the Smolyak algorithm is hardly ever presented. In this chapter, a brief derivation is shown in Section 2.4.2.

## 2.2 Formulation

In order to solve Maxwell's equation under uncertain conditions, we focus in finding a random function,  $u \equiv u(\boldsymbol{\chi}, \mathbf{x}) : \Omega \times \mathcal{D} \rightarrow \mathbb{R}$ , where  $\boldsymbol{\chi} = (\chi_1, \dots, \chi_N)$  is a finite set of  $N$  random variables that characterize the uncertainty of the problem under consideration,  $\Omega$  represents the random domain, and  $\mathbf{x} = (x_1, \dots, x_d)$  are the spatial coordinates in  $\mathbb{R}^d$  for  $d = 1, 2, 3$ . Such function is a parameterized solution of Maxwell's equations for a given electromagnetic problem that satisfies

$$\mathcal{L}_{\mathbf{x}}u(\boldsymbol{\chi}, \mathbf{x}) = h(\boldsymbol{\chi}, \mathbf{x}), \quad \mathbf{x} \in \mathcal{D} \quad (2.1)$$

with the boundary condition

$$\mathcal{B}(\boldsymbol{\chi}, \mathbf{x}; u) = g(\boldsymbol{\chi}, \mathbf{x}), \quad \mathbf{x} \in \partial\mathcal{D} \quad (2.2)$$

where  $\mathcal{L}_{\mathbf{x}}$  is a differential operator (in our particular case, Maxwell equations and their different flavors, e.g., Helmholtz, Laplace, Telegrapher's equations, and so on) that acts on the spatial domain,  $\mathcal{B}$  is a boundary operator (boundary conditions) and  $h$  and  $g$  represent source excitations.

Our goal is to construct an interpolation model of the response  $u$  in terms of those  $N$  random variables. Once we have obtained such a model, we can perform a fast Monte Carlo simulation by evaluating the interpolation, instead of running the EM solver. Alternatively, the statistical moments of the output can be obtained with a quadrature rule. In this manner, we can drastically decrease the simulation time.

Before considering multivariate interpolation, we detail the one-dimensional interpolation scheme, which is used in Section 2.4 for the development of the multivariate case.

## 2.3 Univariate Interpolation

Problem (2.1) presents statistical uncertainty which are carried to the solution  $u$ . In order to capture that uncertainty, we will proceed to find an approximation of  $u$  in terms of the random variable  $\chi$ , denoted as  $\hat{u}(\chi, \mathbf{x})$ . Such approximation is expressed in terms of a set of some basis functions,

$\ell_k(\chi)$  and function evaluations,  $u(\chi_k, \mathbf{x})$ ,

$$\hat{u}(\chi, \mathbf{x}) \equiv \mathcal{U}(u) = \sum_{r=1}^M u(\chi_r, \mathbf{x}) \ell_r(\chi), \quad (2.3)$$

where we let  $\Theta_1 = \{\chi_r\}_{r=1}^M \in \Omega$  be a set of  $M$  prescribed nodes in the one-dimensional random space  $\Omega$  and  $\mathcal{U}$  denotes a sampling operator [9, 11]. Without loss of generality, we assume that the bounded support of the random variables  $\{\chi_r\}_{r=1}^M$  is  $\Omega = [-1, 1]$ .

It is clear, then, that finding interpolation  $\hat{u}(\chi, \mathbf{x})$  is equivalent to solving  $M$  deterministic problems (2.1)-(2.2), for each nodal point  $\chi_r$ ,  $r = 1, \dots, M$  in the nodal set  $\Theta_1$  [13]. Once the interpolation has been constructed, the moments of random function can be obtained, for example,

$$E(\hat{u})(\mathbf{x}) = \sum_{r=1}^M u(\chi_r, \mathbf{x}) \int_{\Omega} \ell_r(\chi) f(\chi) d\chi, \quad (2.4)$$

where  $f(\chi)$  is the PDF of random variable  $\chi$ .

The integral in (2.4) is numerically evaluated and reduced to

$$E(\hat{u})(\mathbf{x}) = \sum_{r=1}^M u(\chi_r, \mathbf{x}) \omega_r, \quad (2.5)$$

where weights  $\omega_r$  and the nodes in set  $\Theta$  are given and chosen according to the employed quadrature rule, for instance the Gaussian quadrature rule.

## 2.4 Multivariate Interpolation

The interpolation of a multivariable function is obviously more complex. In fact, a considerable amount of research has been devoted to find appropriate selections of points  $\Theta_N = \{\chi_r\}_{r=1}^M$  that give good approximation of the unknown function to the desired accuracy level [88].

Two types of interpolation grids are explored for the implementation of stochastic collocation, namely tensor and sparse grids. While the number of nodes in a tensor grid grows exponentially with the number of dimensions of the random space, the number of nodes in a sparse grid grows much more slowly (see [13] for details). In this section, we discuss those approaches

and focus our attention toward the formulation of sparse grid interpolation methods that will be extensively used in forthcoming chapters.

### 2.4.1 Tensor Grid Interpolation

A natural way to obtain the interpolation model is the tensor product of one-dimensional sets; see equation (2.3) [13]. The approximation of function  $u : [-1, 1]^N \rightarrow \mathbb{R}$  is constructed with a tensor interpolation based on the individual one-dimensional interpolation schemes. The tensor formula is,

$$\hat{u}(\boldsymbol{\chi}, \mathbf{x}) \equiv (\mathcal{U}^{i_1} \otimes \dots \otimes \mathcal{U}^{i_N})(u) = \sum_{r_1=1}^{m_{i_1}} \dots \sum_{r_N=1}^{m_{i_N}} u(\chi_{r_1}^{i_1}, \dots, \chi_{r_N}^{i_N}, \mathbf{x}) \cdot (\ell_{r_1}^{i_1} \otimes \dots \otimes \ell_{r_N}^{i_N}), \quad (2.6)$$

where the vector of summation indices,  $\mathbf{r} = [r_1, \dots, r_N]$  count the samples in the grid, while indices  $\mathbf{i} = [i_1, \dots, i_N]$  refer to the level of interpolation. The higher the level, the more accurate approximation we get and the denser the grid is. In this method, for each sample  $\chi_k^{i_n}$  there are  $m_{i_1}$  samples in random variable 1,  $m_{i_2}$  samples in random variable 2, and so on.

The interpolation nodes are commonly chosen to be the roots of the Chebyshev polynomials of the first kind in order to optimize the integration like in equation (2.4). The nodes are given by

$$\chi_r^i = \begin{cases} -\cos \frac{\pi(r-1)}{m_i-1}, & \text{if } m_i > 1 \\ 0, & \text{if } m_i = 1 \end{cases}. \quad (2.7)$$

The grid that results from the use of such nodes is called Clenshaw-Curtis and is commonly used in numerical integration of high-dimensional spaces.

For the one-dimensional case, the number of nodes  $m_p$  depends on the parameter  $i$  and is given by

$$m_i = \begin{cases} 1, & \text{if } i = 1 \\ 2^{i-1} + 1 & \text{if } i > 1 \end{cases}. \quad (2.8)$$

The number of required nodes,  $M$ , grows exponentially with the number of nodes in each dimension. Thus, for a uniform grid,  $M = m_i^N$ , while, in general  $M = \prod_{n=1}^N m_{i_n}$ . Clearly, this number grows quickly for high-dimensional

stochastic problems. This limitation motivates the implementation of an alternative scheme, called Sparse Grid Interpolation, which reduces the high computational cost associated with tensor grids.

## 2.4.2 Sparse Grid Interpolation

The sparse grid interpolation schemes are based on the Smolyak algorithm [8] which attempts to approximate (2.6) with a simple sum of  $M$  weighted basis functions,

$$\hat{u}(\boldsymbol{\chi}, \boldsymbol{x}) = \sum_{r=1}^M u(\boldsymbol{\chi}_r, \boldsymbol{x}) L_r(\boldsymbol{\chi}). \quad (2.9)$$

### 2.4.2.1 Formulation

In order to explain the approximation taken by Smolyak we proceed with the consideration of a simple formulation presented by Ullrich [9].

Consider the convergent sequences of numbers,  $(a_{i_1})_{i_1=0}^{\infty}, \dots, (a_{i_N})_{i_N=0}^{\infty}$ . The limits are denoted by  $a^1, \dots, a^N$  with the conditions  $a_{-1} = 0$ . Therefore, we can write,

$$a^n = \sum_{i_n=0}^{\infty} (a_{i_n} - a_{i_n-1}). \quad (2.10)$$

The case of multidimensional functions is extended by considering the tensor grid formulation (2.6). The product of basis functions is analogously obtained through the product of series limits as follows

$$a^1 \cdot \dots \cdot a^N = \sum_{i_1, \dots, i_N=0}^{\infty} \prod_{n=1}^N (a_{i_n} - a_{i_n-1}). \quad (2.11)$$

Smolyak [8] proposed to approximate (2.11) by truncating the infinite summation in the following way

$$\sum_{i_1 + \dots + i_N \leq q} \prod_{n=1}^N (a_{i_n} - a_{i_n-1}), \quad q = 0, 1, \dots \quad (2.12)$$

By letting  $a_{i_n} \equiv \mathcal{U}^{i_n}(\chi_n)$ , where  $\mathcal{U}$  denotes a sampling operator, the suggested

approximation procedure results in an operator which uses samples from a sparse grid [9, 11] and we are able to approximate tensor formula (2.6) with a less computationally expensive one,

$$\hat{u}_{q,N}(\boldsymbol{\chi}, \boldsymbol{x}) = \sum_{i_1 + \dots + i_N \leq q} (\mathcal{U}^{i_1} - \mathcal{U}^{i_1-1}) \otimes \dots \otimes (\mathcal{U}^{i_N} - \mathcal{U}^{i_N-1}). \quad (2.13)$$

#### 2.4.2.2 Sparse Grid

For an easier numerical implementation of the Smolyak algorithm, we can express equation (2.13) in the form shown in [12],

$$\hat{u}_{q,N}(\boldsymbol{\chi}, \boldsymbol{x}) = \sum_{q-N+1 \leq |\mathbf{i}| \leq q} (-1)^{q-|\mathbf{i}|} \binom{N-1}{q-|\mathbf{i}|} \mathcal{U}^{i_1} \otimes \dots \otimes \mathcal{U}^{i_N}, \quad (2.14)$$

where  $|\mathbf{i}| = i_1 + \dots + i_N$ . This means that we need to consider only those indices that satisfy the inequality  $q - N + 1 \leq |\mathbf{i}| \leq q$  and thus calculate the function (our system response) for those nodes that correspond to the sparse grid given by

$$\Theta_N \equiv \mathcal{H}(q, N) = \bigcup_{q-N+1 \leq |\mathbf{i}| \leq q} (\Theta_1^{i_1} \times \dots \times \Theta_1^{i_N}). \quad (2.15)$$

This is the cornerstone of the Smolyak algorithm since it reduces the number of required nodes in the interpolation by making use of approximation (2.13). The number of required simulations of a given process is considerably less than those in the tensor grid interpolation. Several studies have been presented in literature [13, 14, 89], where the advantages due to computational savings are quantified. It is common in the literature to define the *interpolation level*,  $k$ , as  $k = q - N$ . This is a measure of the accuracy of the interpolation. The higher the level, the more points in the grid, and the more accurate the interpolation is. Furthermore, the grid nodes are chosen in a nested fashion  $\Theta^i \subset \Theta^{i+1}$ , such that, as we increase the level, only a small set of extra simulations is required.

Finally, the basis functions,  $L_r(\boldsymbol{\chi})$ , can be found from the initially targeted formula (2.9) as [88],

$$L_r(\boldsymbol{\chi}) = \sum_{j=1}^s (-1)^{q-|\mathbf{i}^j|} \binom{N-1}{q-|\mathbf{i}^j|} \cdot (\ell_{r_1}^{i_1^j} \otimes \dots \otimes \ell_{r_N}^{i_N^j}), \quad (2.16)$$

where we select those coordinates that satisfy  $q - N + 1 \leq |\mathbf{i}^j| \leq q$  and all such *distinct* grid coordinates are added to an index set  $\mathfrak{J}$  and numbered consecutively from  $j = 1$  to  $s$ , such that  $\mathfrak{J} = \{\mathbf{i}^1, \dots, \mathbf{i}^s\}$  [88].

Sparse grid interpolation is employed in Chapter 3 to assess microwave structures with uncertainty in their geometry and electrical properties. Next, a numerical example is presented where sparse grid interpolation is used as a multivariate quadrature rule (see (2.5)) to demonstrate its accuracy in the context of calculating the statistical moments of the fields in an EM scattering problem.

## 2.5 Numerical Example

The benefits of stochastic collocation and sparse grid interpolation are demonstrated through an application example that calculates the statistical moments of the radiation cross section (RCS) for a two-dimensional homogeneous dielectric cylinder with random geometry and permittivity. Similar studies have been presented in the literature [90, 45].

### 2.5.1 Statistical Characterization

The profile of an infinitely long homogeneous cylinder of constant cross section along its length and its permittivity are described in terms of random variables. For the case of the relative permittivity,

$$\varepsilon_r = \varepsilon_{ro} (1 + \chi_1), \quad (2.17)$$

where the random variable,  $\chi_1$ , follows a Gaussian distribution with zero mean.

In the case of its cross-sectional geometry, we assume the cylinder has a circular profile perturbed by the statistical variability. With the  $z$ -axis of the reference coordinate system taken to coincide with the cylinder axis, the radius of a cylinder is taken to be a periodic function of the transverse-plane

angle, we can write it in terms of a Fourier series expansion,

$$\rho(\phi) = \rho_o + \sum_{n=1}^{\infty} (a_n \cos(n\phi) + b_n \sin(n\phi)). \quad (2.18)$$

For the case of a circular cylinder, expression (2.18) is reduced to a simple constant value,  $\rho_o$ . For our purposes, two random variable are introduced to define the random perturbation from the circular cross section as follows.

$$\rho(\chi_2, \chi_3; \phi) = \rho_o + \chi_2 \cos(2\phi) + \chi_3 \sin(2\phi). \quad (2.19)$$

The random variables  $\chi_{2,3}$  are i.i.d. (independent and identically distributed) zero-mean Gaussian random variables. Furthermore, they are also assumed independent of  $\chi_1$ . In this way, we can characterize a cylinder with a distorted profile and uncertain permittivity in terms of three independent random variables.

## 2.5.2 Stochastic Simulation

An integral equation solver is employed for our purposes and the technical details are presented in Appendix A. The radiation cross section, RCS, is defined by

$$RCS(\phi, \phi^{inc}) = \lim_{\rho \rightarrow \infty} 2\pi\rho \frac{|\mathbf{E}^{sc}(\rho, \phi)|}{|\mathbf{E}^{inc}(\rho, \phi^{inc})|}, \quad (2.20)$$

$$RCS(\phi, \phi^{inc}) = \lim_{\rho \rightarrow \infty} 2\pi\rho \frac{|\mathbf{H}^{sc}(\rho, \phi)|}{|\mathbf{H}^{inc}(\rho, \phi^{inc})|}, \quad (2.21)$$

where  $(\mathbf{E}^{sc}, \mathbf{H}^{sc})$  denote the scattered electric and magnetic fields observed in direction  $\phi$  and  $(\mathbf{E}^{inc}, \mathbf{H}^{inc})$  denote the incident fields observed in direction  $\phi$  [91].

Given the proposed statistical framework, the mean of the radiation cross section,

$$\mu_{RCS}(\mathbf{x}) = \int_{\Omega} RCS(\boldsymbol{\chi}, \mathbf{x}) p(\boldsymbol{\chi}) d\boldsymbol{\chi} \quad (2.22)$$

and its variance,

$$\sigma_{RCS}^2(\mathbf{x}) = \int_{\Omega} RCS^2(\boldsymbol{\chi}, \mathbf{x}) p(\boldsymbol{\chi}) d\boldsymbol{\chi} - \mu_{RCS}^2, \quad (2.23)$$

are calculated. Even though Monte Carlo simulation is the most direct way to estimate the statistical moments, its convergence is very slow and it becomes impractical for complex structures that require expensive computations. Instead, an efficient multivariate quadrature rule, based on the sparse Smolyak algorithm is employed for the numerical calculation of the statistics of the RCS [89, 13]. After invoking (2.5), (2.22) and (2.23) are estimated through the weighted summation of function evaluations,

$$\mu_{RCS}(\phi) \approx \sum_{r=1}^M RCS(\boldsymbol{\chi}_r, \phi) p(\boldsymbol{\chi}_r) w_r, \quad (2.24)$$

and

$$\sigma_{RCS}^2(\phi) \approx \sum_{r=1}^M RCS^2(\boldsymbol{\chi}_r, \phi) p(\boldsymbol{\chi}_r) w_r - \mu_{RCS}^2(\phi). \quad (2.25)$$

Equations (2.24) and (2.25) require  $M$  function evaluations, where  $M$  is significantly smaller than the number involved in a tensor product grid and it is determined by the accuracy level. More details on the calculation of the Smolyak grid nodes,  $\boldsymbol{\chi}_r$ , and weights,  $w_r$ , for a given level of accuracy can be found in [13] and [41].

### 2.5.3 Discussion

The perturbed circular homogeneous dielectric cylinder with  $\varepsilon_{ro} = 5$  and  $\rho_o = 0.5$  m, is impinged by a plane wave propagating along the  $+x$ -axis with electric field amplitude of 1 V/m in the transverse magnetic (with respect to  $z$ ) polarization (TMz) or magnetic field amplitude of 1 A/m in the transverse electric (with respect to  $z$ ) polarization (TEz). For the numerical simulation, the boundary of the cylinder was divided into 500 sections. The mean and standard deviation of the RCS are computed for an accuracy level of 4 [41]. The maximum number of nodes in the sparse grid is 69, requiring 69 numerical solutions of the electromagnetic problem. This number of solutions is considerably less than the tensor grid approach that requires 4913 grid nodes

for the same one-dimensional nodes, and even less than the number required by a Monte Carlo simulation that has a convergence inversely proportional to the square root of the number of iterations meaning that quadrupling the number of sampled points only halves the error. The number of MC samples is typically chosen to be larger than  $10^4$ .

The variance of Gaussian random variables in (2.17) and (2.18) is 0.025 and its mean is zero. Figure 2.1 presents the numerical results where the mean of the RCS is shown along with error bars of length  $\pm\text{std}$  (standard deviation). In general, we observe that there is an excellent agreement with the Monte Carlo result. Also included in the figure is the calculated RCS for the deterministic case of a cylinder of radius and permittivity obtained using the mean values of the three random variables. We clearly see that the mean RCS does not correspond to the one obtained from the “mean-values simulation”. Therefore, to get accurate simulations of scattering problems with uncertain targets, we need to take into account the variability in geometry and electromagnetic properties of objects instead of simply solving for the deterministic problem defined by the mean values of the random parameters.

Tables 2.1 and 2.2 present the percentage errors of the means and standard deviations with respect to the MC simulation defined as follows

$$error = \frac{1}{2\pi} \sqrt{\int_{\phi} |\eta_{SC}(\phi) - \eta_{MC}(\phi)|^2 d\phi}, \quad (2.26)$$

where  $\eta$  denotes the mean and standard deviation of the RCS for the stochastic collocation and Monte Carlo simulations. It is clear that as the *level*  $k$  increases, the number of simulations increases as well as the accuracy. This parameter can be easily used for convergence assessment of the approach due to the nested construction of the sparse grid. In this manner, if a higher accuracy is required, only an extra number of simulations are needed. On the other hand, the increasing number of numerical solutions as the random dimensions increase can still become a computational bottleneck. In view of this, a dimensionality reduction scheme is considered in Chapter 3 to alleviate the computational burden associated with high-dimensional problems.

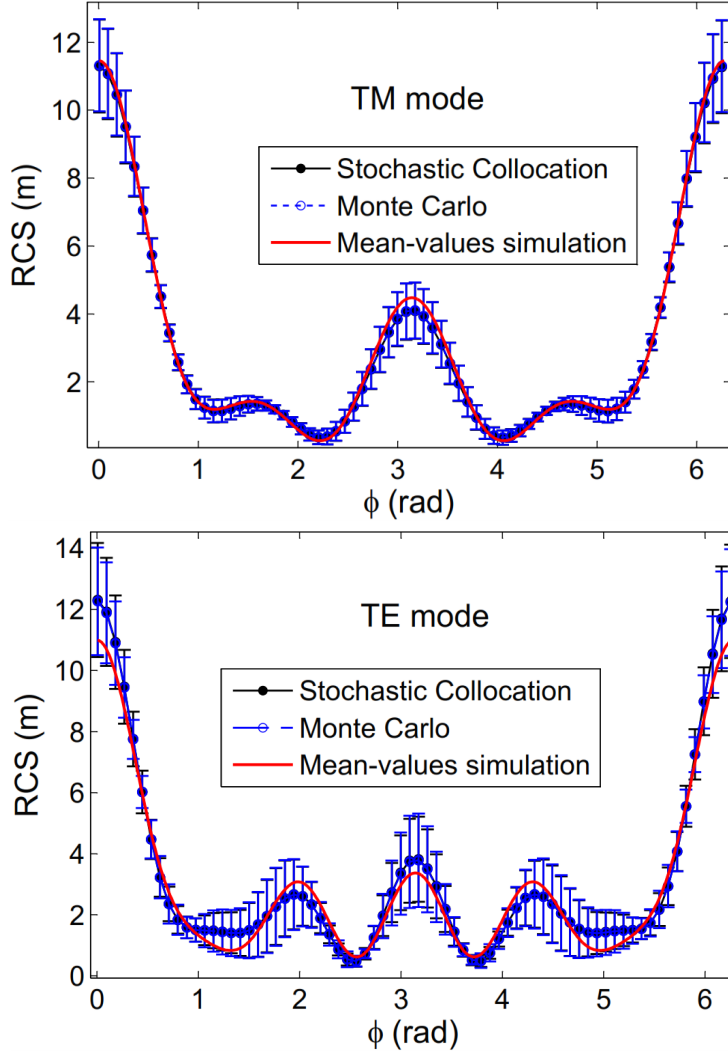


Figure 2.1: Radiation cross section (RCS) for TMz polarization (up) and TEz polarization (bottom) for a dielectric cylinder with random boundary given by  $\rho(\chi_2, \chi_3; \phi) = \rho_o + \chi_2 \cos(2\phi) + \chi_3 \sin(2\phi)$  and permittivity  $\varepsilon_r = 5(1 + \chi_1)$ . Gaussian random variables,  $\chi_{1,2,3}$  have zero mean and variance 0.025. The error bars have a length of  $\pm \text{std}$ , where std is the standard deviation of the RCS. The operation frequency is 0.2 GHz. The stochastic collocation approach is compared with Monte Carlo simulation as well as the calculated RCS from a cylinder defined by the mean-value parameters of the random variables.

Table 2.1: Relative percentage error of the mean and standard deviation of the radiation cross section integrated over the angle  $\phi$  for the stochastic collocation approach with respect to Monte Carlo simulation for different accuracy levels,  $k$ , for the case of TM polarization.

$k$	2	3	4	5
No. Simulations	7	25	69	165
% Error( $\mu$ )	0.422	0.233	0.083	0.116
% Error(std)	7.051	2.087	1.304	0.997

Table 2.2: Relative percentage error of the mean and standard deviation of the radiation cross section integrated over the angle  $\phi$  for the stochastic collocation approach with respect to Monte Carlo simulation for different accuracy levels,  $k$ , for the case of TE polarization.

$k$	4	5	6	7
No. Simulations	69	165	351	681
% Error( $\mu$ )	0.365	0.209	0.532	0.197
% Error(std)	5.550	5.766	4.235	3.319

## 2.6 Concluding Remarks

In this chapter, we have presented the framework for sparse grid stochastic collocation that will be employed in the following chapters for the proposed stochastic modeling methodologies. By interpolating a given output function in terms of input random parameters, it is possible to obtain the statistics of the output fields, signals or quantities of interest in an expedient way. Besides, the moments of the fields can be obtained with an efficient quadrature rule based on the sparse grid interpolation as demonstrated with the example provided. Therefore, traditionally expensive Monte Carlo simulation can be avoided in favor of more efficient methodologies, which is an essential capability for statistical electromagnetic modeling.

## Chapter 3

# RANDOM-SPACE DIMENSIONALITY REDUCTION TECHNIQUE AND YIELD ESTIMATION

### 3.1 Introduction

In this chapter sparse grid interpolation is employed to obtain a statistical characterization of the performance of microwave structures under uncertainty. Particularly, we take advantage of inherent statistical dependencies among random parameters to orthogonalize the random space and reduce its dimensionality. The analysis is also employed to calculate the production yield of the structures under consideration.

As already discussed in the Chapter 2, stochastic collocation is an efficient alternative to the traditional Monte Carlo method. It aims to reduce the computational cost of brute force Monte Carlo techniques by constructing an approximate model of the desired output response over the random space defined by the random input parameters and by making use of efficient sampling schemes to enable faster statistical analysis. Despite its notable advantages, it is often the case that the dimension of the random space is so high that computation efficiency is still an issue. In fact, the number of simulations grows exponentially with the number of dimensions of the random space for the tensor grid interpolation and polynomially for sparse grid interpolation. Consequently, for this reason it is still an open problem of continued research interest. For example, a model-order reduction based approach was proposed recently to tackle the computational cost of a high-dimensional random space of the input parameters [92]. In advancing new methods, an important attribute of significant interest to the designer is for these methods to be seamlessly compatible with commercially available electromagnetic field solvers. This attribute is one that is emphasized in the methodology proposed in this chapter.

The proposed methodology makes use of the Principal Component Analy-

sis (PCA) method to relax the computational complexity of an input random space of high dimension. This approach has been successfully applied in previous works [93, 94] to orthogonalize extracted equivalent circuit parameters of microwave circuits. For our purposes, an implementation is proposed to include an a-priori sensitivity assessment to “weigh” the input random variables according to their level of impact on the desired output response quantities [95, 96]. The resulting modified PCA method is called Principal Component Analysis with Sensitivity Assessment (PCASA). Next, the Adaptive Sparse Grid Collocation (ASGC) method is used to adaptively sample the reduced space and obtain an interpolation of the output in terms of the reduced-space parameters. In this way, the number of electromagnetic field simulations necessary for the construction of the interpolation of the output response function over the reduced random space is considerably reduced. Finally, given the interpolation function of the output, its statistics can be calculated quickly using Monte Carlo (MC). In particular, the scheme from [97] based on the Cross Entropy (CE) algorithm is used to efficiently calculate the production yield of microwave structures in the presence of input parameter uncertainty.

The chapter is organized as follows. Section 3.2 presents the details of the proposed methodology. In Section 3.3, two microwave structures, a coupled microstrip line and a bandpass filter, are used to demonstrate the attributes of the proposed method. The chapter concludes with a summary of the key elements of the proposed methodology.

## 3.2 Formulation

Consider a stochastic electromagnetic boundary value problem (BVP) with  $N$  input random variables,  $\boldsymbol{\xi} = (\xi_1, \dots, \xi_N)$  that, for our purposes, are assumed to be Gaussian, with mean values,  $\mu_i, i = 1, 2, \dots, N$ , and standard deviations,  $\text{std}_i, i = 1, 2, \dots, N$ . The input random space is redefined with the use of the normalized random variables (RVs),  $\chi_i, i = 1, 2, \dots, N$ , defined such that

$$\xi_i = \mu_i + \text{std}_i \chi_i. \quad (3.1)$$

These random variables are associated with the definition of the BVP; thus, they are associated with geometric and/or electromagnetic properties of the materials that define the structure to be analyzed. Following [30], and in the context of propagation of uncertainty from input to output, they define the first of three levels of abstraction. The second level is defined by intermediate parameters that are computed toward the eventual computation of the electromagnetic response of the structure under a given excitation. For example, for the case of a multi-conductor transmission line system and under the assumption of quasi-transverse electromagnetic (quasi-TEM) wave propagation, the second level of parameters involves the per-unit-length parameters resistance, inductance, conductance and capacitance matrices that govern wave propagation in the system. More generally, for a passive microwave multi-port system, its scattering parameters define the second level of abstraction. Finally, the third-level parameters are the desired output response parameters. For example, for the aforementioned multi-conductor transmission line system, these parameters may be the transient voltages at the transmission line ports obtained for a specific length of the line and a specific set of excitation and termination conditions.

Dimensionality reduction is applied at the first abstraction level to reduce the full-order random space of dimension  $N$  to a reduced-order random space of size  $n < N$ . Reduced dimensionality leads to the acceleration of ASGC, which obtains an interpolation model for the desired output response over the random space. The aim is to reduce significantly the number of required simulations for obtaining the statistics of the output response by adaptively sampling the reduced-order random space. To elaborate, consider a tensor grid interpolation over the random space. The number of simulations for the full-order case is  $m^N$ , where  $m$  is the number of sampling points in each dimension, while for the reduced-order case,  $m^n$  simulations are required. Even with a factor of two reduction of the dimensionality of the random space, the number of simulations for the reduced-order model equals the square root of those for the original problem. The algorithm used for random-space dimensionality reduction is described next.

### 3.2.1 Principal Component Analysis with Sensitivity Assessment

First, we take advantage of the correlation, if any, between the input variables parameters to reduce the random space through an orthogonalization of the random space. Toward this objective, Principal Component Analysis (PCA) is used [84]. More specifically, the random space is orthogonalized by finding the non-correlated components of the random input vector of length  $N$ , which are linear combinations of the original variables. Then, the reduced space is defined in terms of those  $n < N$  components with largest variances.

PCA works well for a number of problems where the dimensionality is so large that it is impossible to use a sparse grid interpolation for statistical assessment. For example, random profiles can be described as a finite sequence of correlated random variables (see Section 7.2) and their principal components can be extracted to simplify the statistical characterization. However, PCA does not take into account the importance of each parameter with respect to the output but only the amount of variation of each parameter. Clearly, this can be a limitation to correctly define the reduced-order random space. Therefore, the selection of the reduced set of variables needs to be also guided by the requirement for the selected variables to be those with the most considerable impact on the response. For this purpose, sensitivity coefficients,  $c_i$ , are defined to measure the individual impact of each input variable on the output of interest,  $u(\chi)$ , through the equation,

$$c_i = \frac{\sqrt{E(u(\chi_i) - u(0))^2}}{\max_j(\sqrt{E(u(\chi_j) - u(0))^2})}. \quad (3.2)$$

It is evident from the definition that the sensitivity coefficient measures the relative deviation of the output with respect to the non-perturbed case when only the  $i$ -th random variable changes. If  $m_1$  is the number of nodes in the one-dimensional quadrature rule used for the one-dimensional integration in (2),  $N \cdot m_1$  electromagnetic simulations are required for the calculation of the  $N$  sensitivity coefficients. These extra calculations increase the complexity of our algorithm; however, as demonstrated in Section 3.3, they significantly improve the accuracy of the proposed method.

Once the sensitivity coefficients are computed, they are used to “weigh” the parameters,  $\chi'_i = c_i \chi_i, i = 1, 2, \dots, N$ . Then, the reduced-order random

vector,  $\boldsymbol{\chi}_{red} \in \mathbb{R}^n$ , is found through the transformation

$$\boldsymbol{\chi}_{red} = Q^T \boldsymbol{\chi}', \quad (3.3)$$

where the superscript  $T$  denotes matrix transposition and the matrix  $Q \in \mathbb{R}^{N \times n}$  is built with columns the  $n$  eigenvectors of the correlation matrix  $\Sigma \in \mathbb{R}^{N \times N}$  for the  $N$  random variables of the vector  $\boldsymbol{\chi}$  with largest deviations, given by their corresponding eigenvalues,  $\lambda_i, i = 1, 2, \dots, N$ . The degree of the variation captured by the reduced-order random space is given by the cumulative percentage of total variation,

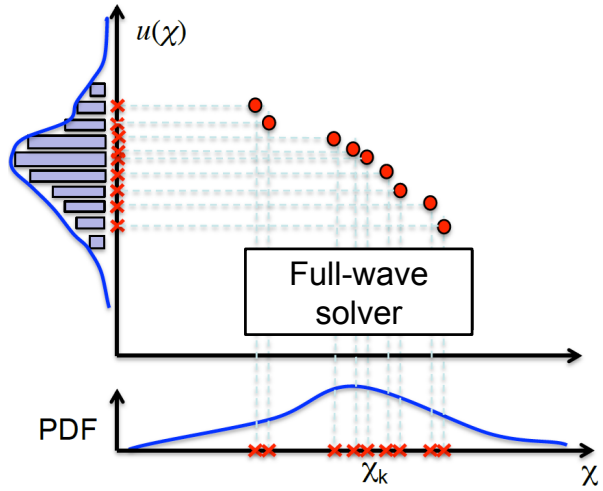
$$C_r = 100 \frac{\sum_{i=1}^n \lambda_i}{\sum_{i=1}^N \lambda_i}. \quad (3.4)$$

This serves as a measure of the accuracy of the approximation and provides a criterion to decide on the dimension  $n$  of the reduced-order space.  $C_r > 90$  is recommended.

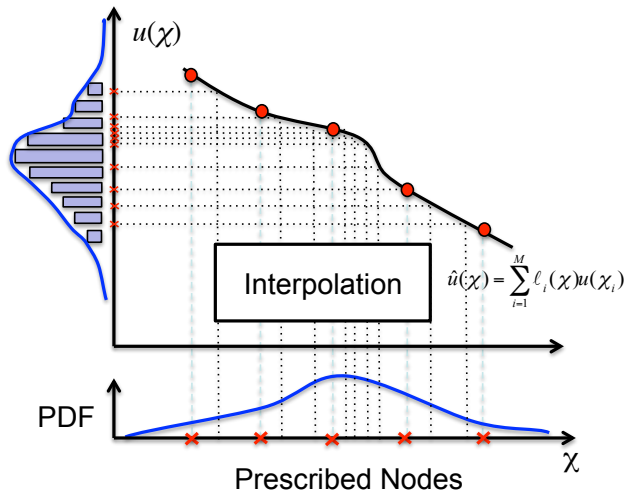
### 3.2.2 Sparse Grid Interpolation

The dimensionality reduction stage of the approach is followed by the construction of an interpolation of the output on the reduced random space. This interpolation is subsequently used to calculate the statistics of the output and the corresponding production yield. Figure 3.1 demonstrates the advantages of constructing an interpolation for statistical modeling over using MC. As shown in Fig. 3.1-(b) the number of full-wave solver simulations are only needed to construct the interpolation. Once it is constructed, the evaluation of the function is done much more efficiently.

Even though there are several interpolation schemes that can be used, like polynomial chaos expansion [36], response surface model [29], or high-dimensional model representation (HDMR) [42], these approaches might not be the most suitable for the rare-event calculations required for yield estimation because of their low accuracy in the distribution tails of the parameters. In view of this, we employ a sparse grid interpolation using piecewise linear basis functions, making use of the MATLAB Sparse Grid Interpolation toolbox of [34]. This toolbox makes use of the Smolyak Algorithm [8]. The key attributes of the interpolation are summarized in the following. The reader



(a)



(b)

Figure 3.1: For a Monte Carlo simulation (a), the full-wave solver needs to be evaluated for a large number of samples so that the PDF of the output can be estimated, while with stochastic collocation (b), a set of prescribed nodes is evaluated with the solver and an interpolation constructed and used to sample the random space to calculate the statistics of the output.

is referred to [33] for more details.

As discussed in Chapter 2, the Smolyak scheme approximates the general tensor product multivariate interpolation formula (2.13)

$$\hat{u}_{q,n}(\boldsymbol{\chi}) = \hat{u}_{q-1,n} + \sum_{|\mathbf{i}|=q} (\mathcal{U}^{i_1} - \mathcal{U}^{i_1-1}) \otimes \dots \otimes (\mathcal{U}^{i_n} - \mathcal{U}^{i_n-1}), \quad (3.5)$$

where  $\hat{u}_{n-1,n} = 0$ ,  $|\mathbf{i}| = i_1 + \dots + i_n$ ,  $q \geq n$  is a parameter that defines the level of the interpolation,  $k = n - q$ , and operant  $\mathcal{U}$  represents the interpolation operator in each dimension,

$$\mathcal{U}^i(u) = \sum_{r=1}^{m_i} u(\chi_r^i) \ell_r(\chi^i). \quad (3.6)$$

In (3.6),  $\ell_r$  is the basis functions associated with the  $r$ -th grid value of the parameter, and  $\mathcal{U}^0 = 0$ . The number of nodes,  $m_i$ , depends on the particular grid choice and the value of  $i$ . Clenshaw-Curtis-type sparse grids, as presented in equations (2.7) and (2.8), are employed.

Equation (3.5) suggests that the interpolation accuracy can be increased without having to discard previous results [15]. The key advantage of the Smolyak formula is that we only need to compute the output using the typically computationally expensive electromagnetic solver at the sparse grid nodes only,

$$\mathcal{H}(q, n) = \bigcup_{q-n+1 \leq |\mathbf{i}| \leq q} (\Theta_1^{i_1} \times \dots \times \Theta_1^{i_n}). \quad (3.7)$$

The grid nodes are chosen in a nested fashion  $\Theta^i \subset \Theta^{i+1}$ , such that, as we increase the level, only a small set of extra simulations is required. Furthermore, the hierarchical construction of the interpolation provides for a dimension-adaptive scheme [35], so that more interpolation points are assigned to the variable that results in larger changes of the output.

### 3.2.3 Efficient Calculation of Yield

Once the scheme for the efficient interpolation of the random space has been constructed we can proceed with the calculation of the desired statistics of

the output response. For example, the mean, standard deviation, and PDF of the output can be calculated for a complete statistical characterization of the output. Another important quantity is yield, understood as the number of units out of the total number of units produced that fail certain performance criteria required for acceptable unit functionality. A straightforward way to compute yield is through the calculation of the probability of failure using Monte Carlo. Given a predefined threshold of the desired output response that quantifies failure, the number of cases where the response exceeds the threshold divided by the total number of cases considered is the failure probability or yield,

$$y = \frac{1}{M} \sum_{i=1}^M I_{\{u(\chi) \geq \gamma\}}, \quad (3.8)$$

where  $I_{\{C\}} = 1$ , if condition  $C$  is true, and  $I_{\{C\}} = 0$ , otherwise.

Obviously, component design is carried out in a manner that maximizes yield; thus,  $y$  in (3.8) is a very small number. Therefore, a brute force Monte Carlo approach to the calculation of yield is computationally expensive. For example, in the case that only one component out of a total of 10,000 fails, at least 10,000 simulations are required to calculate the probability of failure, and many more to get good confidence in our estimation. This makes evident the fact that yield estimation is essentially a *rare-event* probability calculation. Even though the evaluation of our interpolation function is considerably more computationally efficient than running the EM solver, the large number of iterations required by this type of simulation could constitute not only a bottleneck in the efficiency of the methodology but also a memory problem due to the large-sized sets of evaluation values. Fortunately, a robust algorithm has been developed in the statistical community based on the *importance sampling* technique [98] called the *cross-entropy* method (CE) [99, 97]. This algorithm allows the fast calculation of rare event probabilities by changing the sampling PDF which increases the convergence of the simulation. The CE algorithm, presented in [97] and reviewed in Appendix B, is used to calculate the yield for very small failure probabilities and can be also applied to find non-small values of yield.

The formulation of CE is based on the importance sampling technique that calculates a probability  $y$  of a function of random parameters  $\boldsymbol{\chi}$  with given probability density function (PDF),  $f(\boldsymbol{\chi})$ , to exceed a certain threshold,  $\gamma$ ,

by changing the sampling PDF to another one,  $g(\boldsymbol{\chi})$ , that is more heavily distributed near the value of the threshold than the original PDF. The change in sampling PDF is done as follows,

$$y = \int I_{\{u(\boldsymbol{\chi}) \geq \gamma\}} f(\boldsymbol{\chi}) d\boldsymbol{\chi} = \int I_{\{u(\boldsymbol{\chi}) \geq \gamma\}} W(\boldsymbol{\chi}) g(\boldsymbol{\chi}) d\boldsymbol{\chi}, \quad (3.9)$$

where the *likelihood ratio*,  $W(\boldsymbol{\chi})$  is defined as  $W(\boldsymbol{\chi}) = f(\boldsymbol{\chi})/g(\boldsymbol{\chi})$ . Notice that the right-hand side of (3.9) can be estimated with

$$y = \frac{1}{M} \sum_{i=1}^M I_{\{u(\boldsymbol{\chi}) \geq \gamma\}} W(\boldsymbol{\chi}), \quad (3.10)$$

where we sample with respect to the distribution  $g(\boldsymbol{\chi})$ . In this way, the number of required MC simulations is considerably reduced for a given convergence criterion. CE provides an efficient adaptive technique to find the corresponding PDF,  $g(\boldsymbol{\chi})$ .

Gaussian PDFs are used for the input parameters which have been normalized. As a consequence, the set of principal components are independent random variables and the joint distribution,  $f(\boldsymbol{\chi})$ , with zero mean is the product of the individual Gaussian PDFs of each principal component. Also, we assume that the principal components are constrained to the vector range  $[-3\mathbf{std}, 3\mathbf{std}]$ , where  $\mathbf{std}$  is the vector of variances of the distributions of the principal components. In real-world situations, the range should be provided by the manufacturer. Appendix B provides an iterative algorithm to find an appropriate Gaussian PDF,  $g(\boldsymbol{\chi})$ , with mean vector  $\boldsymbol{v}$  which is used in (3.10) to sample the random domain more efficiently than the original distribution. This is accomplished by calculating the mean value of the desired PDF in an iterative way so that the distribution is shifted toward the value of the predefined threshold. As a result, the probability of the rare event increases when sampled using this newly defined distribution. This shifting process can lead, however, to the sampling of parameters in non-defined ranges. We avoid this issue by modifying the width of the computed PDF. This is done in step 3 of the algorithm by setting the standard deviation vector to  $\mathbf{std}_t = \mathbf{std}_0 - |\boldsymbol{v}_t|/3$ , where  $t$  denotes the iteration index. In this way, the range  $[\boldsymbol{v}_t - 3\mathbf{std}_t, \boldsymbol{v}_t + 3\mathbf{std}_t]$  where the new distribution is constrained, is a subset of the original range,  $[-3\mathbf{std}, 3\mathbf{std}]$ , so that the parameters are sampled only in the predefined domain.

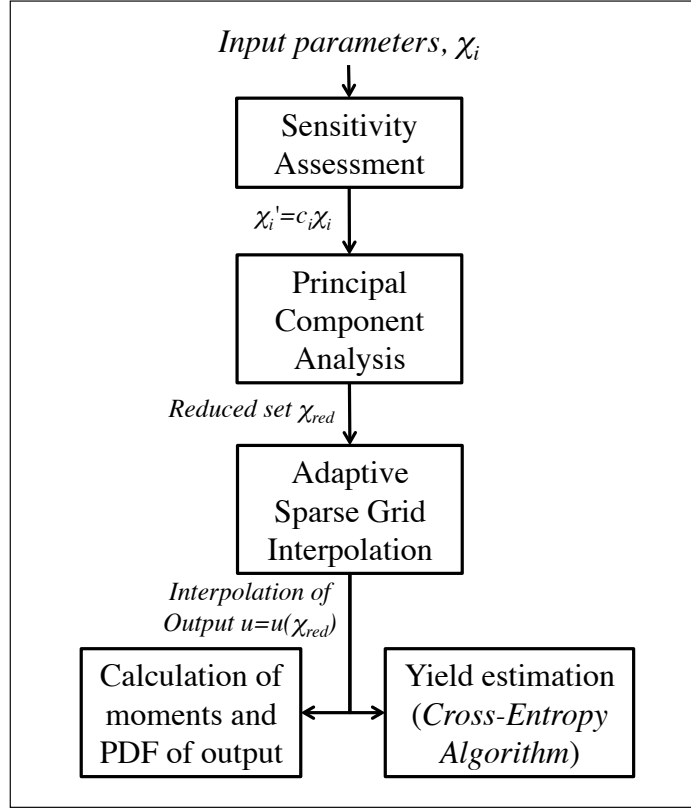


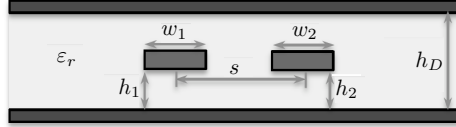
Figure 3.2: Process flow of the proposed methodology.

This is the final step of the proposed methodology that is summarized in Fig. 3.2. The next section presents two numerical applications that demonstrate the efficiency and accuracy of the proposed statistical process.

### 3.3 Numerical Applications

#### 3.3.1 Pair of Interconnects Exhibiting Variability

First, we consider the case of a pair of coupled stripline interconnects of cross-sectional geometry depicted in Fig. 3.3. The random input parameters are the cross-sectional dimensions  $s$ ,  $w_1$ ,  $w_2$ ,  $h_D$ ,  $h_1$ ,  $h_2$ , and the relative permittivity,  $\varepsilon_r$ , of the insulating substrate. All random variables are assumed



	$s$	$w_1$	$w_2$	$h_D$	$h_1$	$h_2$	$\epsilon_r$
$\mu$	3.5	1.5	1.5	4.0	1.75	1.75	4.4
std	0.15	0.2	0.2	0.4	0.1	0.1	0.25

Figure 3.3: Cross-sectional geometry of the coupled stripline interconnect structure, showing the input parameters, assumed to be random Gaussian variables, with mean values and standard deviations as shown in the table. The units of the parameters that define the geometry are mm.

Table 3.1: Correlation function  $\Sigma$  of the normalized input parameters for a coupled stripline structure.

$s$	$w_1$	$w_2$	$h_D$	$h_1$	$h_2$	$\epsilon_r$
1	0.213	0.163	0.007	0.068	0.060	-0.002
	1	0.160	-0.0011	0.180	0.007	0.032
		1	-0.031	0.006	0.125	-0.032
			1	0.360	0.250	0.0022
				1	0.250	-0.016
					1	0.009
						1

gaussian with mean values and standard deviations given in the accompanying table in Fig. 3.3. Furthermore, the correlation matrix for their normalized values is given in Table 3.1.

For this type of structure, in the context of signal integrity, crosstalk voltage at the ports of one of the interconnects when the other one is excited is an undesirable quantity that qualifies as a failure criterion. Therefore, for the purposes of this study, we will use the crosstalk voltage at the far end of one of the two wires as the failure criterion for the calculation of yield in the presence of uncertainty in the input parameters.

ANSYS<sup>®</sup> Q3D Extractor<sup>®</sup> [100] has been used for the RLGC parameters extraction. The insulating dielectric material is epoxy FR4, the conductors are copper, and the length of the traces is 5 cm. One trace is driven at one end by a voltage source of input resistance of 50  $\Omega$ , generating a trapezoidal pulse of amplitude 5 V, turn-on delay time of 20 ns, rise and fall times of 2 ns, and width of 6 ns. The remaining three ports are terminated with 50  $\Omega$

Table 3.2: Simulation results for a coupled stripline structure.

	No. of Simulations		ISE (1/V) in probability density	
$n$	PCA	PCASA	PCA	PCASA
3	117	109	8.542	0.975
4	157	161	13.138	0.784
5	115	153	2.104	0.127
Full order		293	Reference Solution	

resistors.

For the sensitivity analysis part of the PCASA algorithm, a quadrature rule with three nodes was employed. This step adds 14 extra simulations to the process. The dimensionality reduction algorithm was applied next to reduce the seven-dimensional random space to reduced spaces of dimension 3, 4, and 5. The construction of the interpolant for the calculation of the cross-talk voltage in terms of these reduced-order parameters was done with the tool *spinterp* [9]. The adaptive sampling process stopped when a relative tolerance of 0.05 was achieved. Once the model was created, it was used to compute the probability density functions of the cross-talk voltage for the case of the standard PCA and the proposed PCASA.

The effect of the dimensionality reduction is quantified in Table 3.2. The advantage of employing the reduced order model is evident in terms of the number of sampling points required for convergence to a given tolerance and the obtained accuracy. Focusing on columns 2 and 3 in Table 3.2, we observe that, while the original full-order system needs 293 simulations, the reduced-order systems require a smaller number and, as expected, the smaller the order of the reduced system, the smaller the number of simulations. Furthermore, as evident from Fig. 3.4, the incorporation of sensitivity assessment in PCA improves the accuracy of the reduced-order model. This improvement comes at the cost of an increased number of simulations, as clearly seen in the comparison between PCASA and PCA in Table 3.2; however, the mean integrated squared error (MISE) is considerably reduced when the sensitivity assessment is performed. Also, for the same number of simulations, PCASA yields lower error values. Finally, we comment that the cumulative percentage of total variation for  $n = 5$  is 99.5%, for  $n = 4$  is 93.2%, and for  $n = 3$ , 80.9%, which is reflected in the MISE of the results.

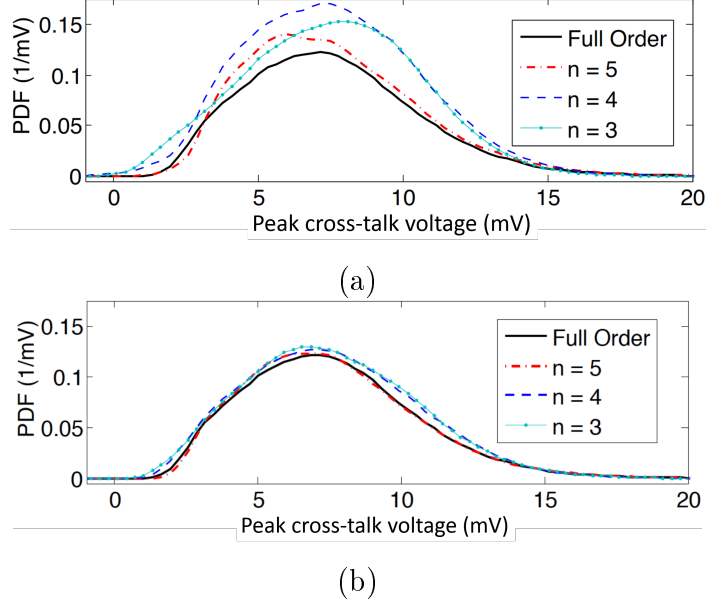


Figure 3.4: Probability density function of the peak cross-talk voltage of the full-order and three reduced-order systems obtained through (a) regular PCA and (b) PCA with sensitivity assessment.

**Calculation of yield.** Next, the estimation of the yield is carried out using the CE method assuming crosstalk thresholds of 23 mV and 26 mV. For this purpose, the reduced system of  $n = 5$  was used and the values  $\rho = 0.02$  and  $M = 10^3$  were used for the CE algorithm. The performance of the CE algorithm is compared with Monte Carlo and the results are shown in Table 3.3. We observe that the probability of failure values are similar for the Monte Carlo and CE cases and they differ as the threshold increases, because that makes the calculation more expensive. A quantity used to measure the accuracy of the approach is the relative error (RE) defined as the standard variation of the yield divided by its value. Even though the relative error is lower for the CE case, the number of iterations needed in the simulation is one order of magnitude lower than the Monte Carlo calculation and so is the CPU time. This demonstrates that the proposed approach yields more accurate results with less computational effort.

### 3.3.2 Bandpass Filter

The second study examines the impact of geometric uncertainty on the filtering properties of a bandpass filter. Specifically, we focus on the effect of

Table 3.3: Calculation of yield for a maximum peak crosstalk voltage.

	$\gamma$	$P(v_{xt} > \gamma)$	std( $y$ )/ $y$	No. iter.	CPU time
MC	23 mV	$3.6 \times 10^{-4}$	0.477	$10^4$	10.34 s
CE	23 mV	$3.74 \times 10^{-4}$	0.1854	$10^3$	1.432 s
MC	26 mV	$5.88 \times 10^{-5}$	0.2691	$5 \times 10^5$	535 s
CE	26 mV	$6.32 \times 10^{-5}$	0.154	$5 \times 10^4$	52.7 s

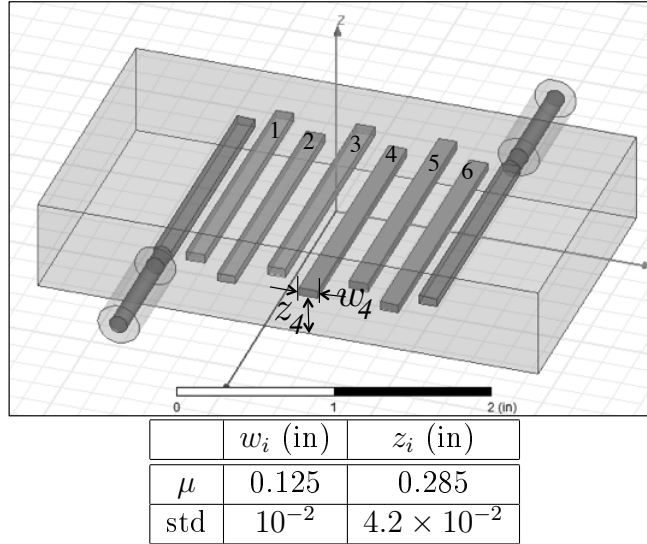


Figure 3.5: Geometry of the bandpass filter. The model and dimensions were obtained from [1].

variability on the 3 dB bandwidth of the filter. For our purpose, the filter considered is the bandpass filter described in Ansoft’s HFSS<sup>®</sup> [100] tutorial document [1] has been used for the RLGC parameters extraction. The filter has six internal rods that are assumed to exhibit uncertainty in their position and dimensions as indicated in Fig. 3.5 and the accompanying table that includes the mean values and standard deviations of the twelve geometric parameters involved. These parameters are assumed to be Gaussian random variables with correlation matrix for their normalized values given in Table 3.4. It is evident from the correlation matrix that the dependencies are stronger for adjacent rods.

The scattering parameters of the filter were computed for the sparse grid nodes over reduced-order random spaces of different dimensions. For such purpose, ANSYS<sup>®</sup> HFSS<sup>®</sup> was employed. Some of the corresponding plots are depicted in Fig. 3.6, making evident the impact of geometric uncertainty on the filter 3 dB bandwidth, which was originally intended to be 1 GHz

Table 3.4: Correlation function  $\Sigma$  of the normalized parameters in the geometry definition of a bandpass filter ( $i = 1, 2, \dots, 6$ ).

$w_i$	$w_{i+1}$	$w_{i+2}$	$w_{i+3}$	$z_i$	$z_{i+1}$	$z_{i+2}$	$z_{i+3}$
1	0.36	0.09	0.01	0.152	0.0024	0	0
	1	0.36	0.09	0.0024	0.152	0.0024	0
		1	0.36	0	0.0024	0.152	0.0024
			1	0	0	0.0024	0.152
				1	0.694	0.354	0.057
					1	0.694	0.354
						1	0.694
							1

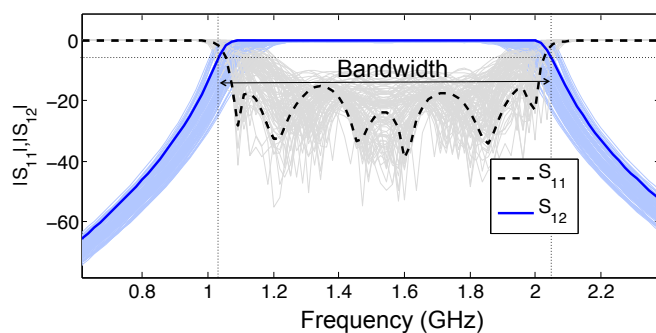


Figure 3.6: Calculated scattering parameters for various realizations of the structure obtained via sampling of reduced input random space.

centered at 1.5 GHz.

The calculated probability density functions of the bandwidth using reduced models of different order are depicted in Fig. 3.7 and compared with the full-order model. Very good correlation is observed. A comparison of the proposed PCASA algorithm with the traditional PCA is depicted in Table 3.5. Its improved accuracy is evident. Additionally, such accuracy is obtained at one third the computational cost of working with the full-order case for the case of a reduced model of order 5, and roughly one half of the computational cost of working with the full-order model for the case of a reduced model of order 9.

**Calculation of yield.** In the final step of our methodology we estimate the yield with the CE algorithm. The system with a reduced dimension of 9 has been employed for this purpose, and the values  $\rho = 0.005$  and  $M = 10^3$  were used in the implementation of the CE algorithm. Results are

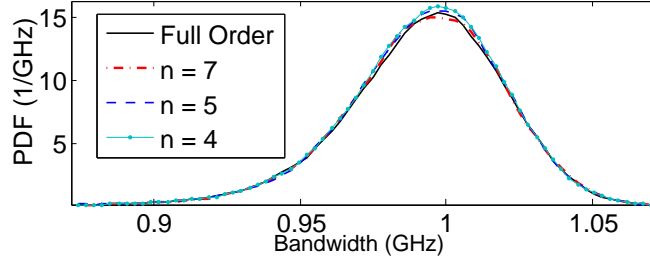


Figure 3.7: Comparison of the calculated probability density function of the bandpass filter bandwidth using the full-order model and reduced models of different dimensions generated through PCASA.

Table 3.5: Simulation results of the interpolation of the band-pass filter.

	No. of Simulations		ISE (1/GHz) in probability density	
$n$	PCA	PCASA	PCA	PCASA
5	29	57	0.0189	0.0153
7	59	55	0.0582	0.0029
9	63	67	0.0652	0.00181
Full order	143		Reference Solution	

shown in Table 3.6 where we observe a dramatic drop in the yield as the threshold increases from 1.05 GHz to 1.07 GHz. Also depicted in the table are comparisons between Monte Carlo and the CE algorithm, indicating the superior efficiency and accuracy of the latter.

### 3.4 Concluding Remarks

In this chapter an efficient methodology has been proposed for the reduction of the dimensionality of the input random space of stochastic electromagnetic problems associated with the modeling of passive microwave components

Table 3.6: Calculation of yield for a maximum bandwidth of 1.05 and 1.07 GHz.

	$\gamma$ (GHz)	$P(BW > \gamma)$	$\text{std}(y)/y$	No. iter.	CPU time
MC	1.05	$12 \times 10^{-4}$	0.104	$10^5$	1412 s
CE	1.05	$12 \times 10^{-4}$	0.137	$10^4$	144.3 s
MC	1.07	$6.7 \times 10^{-6}$	0.362	$10^6$	975 s
CE	1.07	$6.7 \times 10^{-6}$	0.147	$10^5$	99.5 s

in the presence of input parameters uncertainty. The methodology makes use of a modified principal component analysis and an adaptive sparse grid collocation scheme to expedite the sampling of the random space through the construction of efficient interpolants for the output response quantity of interest without jeopardizing accuracy. The methodology has been employed to calculate the production yield of the structures with uncertainty. For this purpose, the cross-entropy algorithm has been successfully applied as an efficient alternative to Monte Carlo simulations, offering a tenfold reduction in yield calculation for the cases considered. In addition to its efficiency, the resulting algorithm for yield calculation has been demonstrated to exhibit superior accuracy.

## Chapter 4

# STOCHASTIC MACROMODELING

### 4.1 Introduction

Up to this point, stochastic collocation has been employed in combination with EM solvers to perform statistical assessment of the performance of microwave structures exhibiting uncertainty in their material and geometric parameters. The algorithm dictates the sparse grid points in the random space defined by the input random parameters of the structure under consideration at which the response is to be calculated toward the implementation of a faster means of calculating the statistics of the response. Special emphasis is placed on avoiding any modification to the EM solver. In other words, we want the methodology for expedient stochastic modeling to be non-intrusive. In this and forthcoming chapters we present methodologies based on the Finite Elements Method (FEM) and Sparse Grid Collocation to extract stochastic macromodels of domains exhibiting uncertainty as presented in [101]. Such models are used next to extract the statistical moments of the fields in stochastic scattering problems.

Over the years, the term macromodeling has been used in scientific and engineering modeling and simulation to describe a variety of things. In the context of electromagnetic (EM) modeling and simulation, macromodeling is widely understood to mean the process through which a compact physical or mathematical model is defined to describe the EM attributes of a portion of the system, the detailed description of which requires a large number of degrees of freedom (state variables) for its modeling. In this context, low-order, EM macromodels have been used extensively for a variety of applications. These include, expedient calculation of the broadband response of passive EM devices; use of domain decomposition techniques for the EM field modeling of electrically-large structures of high complexity; and the abstrac-

tion of distributed portions of composite systems that include both lumped circuit components and distributed electromagnetic structures.

In this chapter we describe a methodology for the macromodeling of portions of linear, passive EM structures that exhibit geometric and/or material uncertainty. In particular, we are interested in structures formed as an ensemble of multiple domains, with the aforementioned material and geometric uncertainty occurring in some or all of these domains but not in the medium in which these domains are immersed. Figure 4.1 depicts a representative example of such a composite structure.

The problem of electromagnetic modeling of structures that exhibit randomness is one of significant interest to the electromagnetics community because of its relevance to several application domains such as remote sensing, EMI/EMC in electronic systems, and EM wave propagation in random media. For the case of EM wave scattering by composite random structures like the one depicted in Fig. 4.1, the complexity of a Monte Carlo numerical solution is compounded by the need to generate a discrete numerical model for each one of the geometries resulting from the sampling of the multi-dimensional random space defining the randomness of the structure. For example, in the context of the finite element solution of the EM boundary value problem (BVP), a new finite element grid needs to be generated for each one of the realizations of the geometry during the Monte Carlo sampling of the random space.

In this chapter a macromodeling methodology as proposed in [101] is presented as a means to alleviate the repeated discretization of the computational domain in the numerical solution of the stochastic EM BVP. The proposed methodology makes use of the mathematical framework of polynomial chaos expansions and stochastic collocation [36, 13, 32, 14], which has been applied recently to the numerical solution of a variety of EM BVPs (see [44, 102, 103, 86, 87] for representative examples). These are combined with the concept of network matrix representation of passive EM structures (see Chew [104] for details) to develop a compact stochastic impedance (or admittance) matrix macromodel on a fixed boundary enclosing each one of the domains that exhibits randomness. In this manner, only a single numerical grid is needed for the Monte Carlo solution of the EM scattering by the ensemble of the random domains.

The proposed approach is described in Section 4.2. Section 4.3 presents

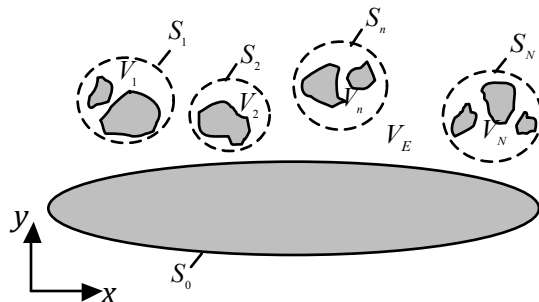


Figure 4.1: Reference geometry for the discussion of the concept of stochastic macromodeling.

examples from the application of the method to the two-dimensional scattering by arrays of conducting cylinders exhibiting geometric randomness. The chapter concludes with some remarks on future extensions of the method.

## 4.2 Stochastic Macromodeling

As suggested in the introduction, the electromagnetic structures of interest to this discussion are composite structures comprising several subdomains, with a good number of them exhibiting uncertainty in their material and/or geometric composition. The EM analysis of such a structure using, for example, a Monte Carlo (MC) process, requires the development of as many finite elements (FE)/ finite difference (FD) models (including the generation of an FE/FD mesh for each model) as the samples in the random space used in the MC process. One way to reduce the associated computational cost is by removing the need for the repeated mesh generation. The way stochastic macromodeling makes this possible is demonstrated in this section.

To fix ideas, we will consider the case of electromagnetic wave scattering by a collection of targets embedded in an unbounded linear host medium. While the geometric and material attributes of each one of the targets exhibit a statistically defined randomness, the host medium does not. Figure 4.1 serves as a representative example of such a structure. Any randomness in geometric attributes or material properties occurs only inside the  $N$  regions  $V_1, V_2, \dots, V_N$  bounded by surfaces  $S_1, S_2, \dots, S_N$  respectively. The exterior medium, including the volume bounded by surface  $S_0$ , is assumed to be fixed

in terms of its geometric attributes and its electromagnetic properties. In view of this, it is immediately apparent that, under the assumption that the  $N$  surfaces  $S_1, S_2, \dots, S_N$  are fixed, the domain  $V_E$  bounded by these  $N$  surfaces and the surface at infinity is a fixed domain free from any geometric or material uncertainty. The way the randomness of the interiors of the domains  $V_n, n = 1, 2, \dots, N$  manifests itself in the solution of the exterior BVP in  $V_E$  is through the boundary conditions on the surfaces. This, then, suggests the idea of a stochastic macromodel for each one of the  $N$  subdomains in terms of a global surface impedance relationship on  $S_n, n = 1, 2, \dots, N$ . The way this is done is described next.

#### 4.2.1 Global Impedance Matrix

For the purposes of this discussion, let the geometry of Fig. 4.1 be the cross-sectional geometry of an infinitely long cylindrical scatterer. Under the assumption that both the cross-sectional geometry of the scatterer and the exciting electromagnetic field are  $z$  invariant, the pertinent electromagnetic boundary value problem is a two-dimensional one. Focusing on the case of TE $_z$  polarization, where the magnetic field is linearly polarized in the  $z$  direction, we assume, without loss of generality, that  $S_n$  is a circle. A local reference coordinate system is introduced, with the origin the center of the circular boundary  $S_n$ . Fourier series expansions in the polar angle  $\phi$  are used to represent the tangential electric and tangential magnetic fields on  $S_n$ . For each Fourier mode in the expansion of the tangential magnetic field on  $S_n$  the solution of the interior BVP in  $V_n$  yields a tangential electric field on  $S_n$ . In this manner, a global impedance condition is established on  $S_n$ , defined in terms of the matrix relationship,

$$\xi_k = \sum_{m=-N_{mod}}^{N_{mod}} Z_{km}^{(n)} h_m, \quad k = 0, \pm 1, \dots, \pm M, \quad (4.1)$$

where  $\xi_m, h_m$  are, respectively, the coefficients in the Fourier series expansions of the tangential electric field and the tangential magnetic field on  $S_n$ ,

$$E_\phi \approx \sum_{m=-N_{mod}}^{N_{mod}} \xi_m e^{jm\phi}, \quad H_z \approx \sum_{m=-N_{mod}}^{N_{mod}} h_m e^{jm\phi}. \quad (4.2)$$

The truncation of the expansions in (4.2) is necessary for the numerical implementation of (4.1). The important observation here is that the global impedance matrix, defined through (4.1), (4.2), serves as an electromagnetic macromodel for the region  $V_n$ . Once the impedance matrices for all domains  $V_n, n = 1, 2, \dots, N$ , are available, the solution to the exterior electromagnetic BVP in  $V_E$  due to an arbitrary excitation at the frequency of interest is computed in a straightforward fashion. In the presence of geometric and/or material uncertainty in  $V_n$ , the elements of the global impedance matrix  $\mathbf{Z}^{(n)}$  can be used to account for the impact of the randomness of the region to the electromagnetic response of the overall structure. By abstracting the randomness of the interior region on the global impedance matrix defined on a fixed boundary, a single numerical grid is necessary for the solution of the exterior BVP. In the next subsection, a process is described for abstracting the randomness in the geometric and/or material properties of the region  $V_n$  to the elements of the global impedance matrix  $\mathbf{Z}^{(n)}$  on the fixed boundary  $S_n$ .

#### 4.2.2 Stochastic Global Impedance Matrix

Let  $\boldsymbol{\chi} = (\chi_1, \chi_1, \dots, \chi_D)$  denote the set of independent random variables necessary for describing the uncertainty in  $V_n$ . In the case of statistically dependent random variables, the methodology proposed in Chapter 3 can be used to orthogonalize the random space. Furthermore, let  $\rho(\boldsymbol{\chi})$  denote their joint probability density function. The objective is to develop a systematic and expedient process for obtaining a global impedance matrix  $\mathbf{Z}^{(n)}$  that serves as an accurate macromodel of the electromagnetic attributes of  $V_n$  for any point in the  $D$ -dimensional probability space  $\Omega$  defined by  $\boldsymbol{\chi} = (\chi_1, \chi_1, \dots, \chi_D)$ .

#### 4.2.3 Polynomial Chaos Expansion

Toward this objective, use is made of the machinery of polynomial chaos expansion of random functions in  $\Omega$ . Following the ideas in [14], a truncated polynomial chaos expansion [55] of  $Z_{km}^{(n)}$  is of the form

$$Z_{km}^{(n)} \approx \sum_{i=0}^P c_i \Gamma_i(\boldsymbol{\chi}), \quad (4.3)$$

where  $\Gamma_i(\boldsymbol{\chi})$  are multidimensional orthogonal polynomials with regard to the inner product,

$$\langle \Gamma_i \Gamma_j \rangle \equiv \int_{\Omega} \Gamma_i(\boldsymbol{\chi}) \Gamma_j(\boldsymbol{\chi}) \rho(\boldsymbol{\chi}) d\boldsymbol{\chi} = \delta_{ij} \|\Gamma_i\|^2. \quad (4.4)$$

The type of random variables dictates the family of the polynomials to be used [32]. For example, for the case of Gaussian random variables, Hermite polynomials are used. A detailed description and list of multidimensional polynomials are provided in [36]. The number of terms,  $P$ , included in the truncated polynomial chaos expansion depends on the dimensionality  $D$  of the random space and the highest-order  $p$  of the multidimensional polynomials used, and is given by

$$P + 1 = \frac{(D + p)!}{D! p!}. \quad (4.5)$$

In view of (4.3), the coefficients in the polynomial chaos approximation of (4.3) are computed using the orthogonality relation (4.4),

$$c_i = \frac{1}{\|\Psi_i\|^2} \int_{\Omega} Z_{km}^{(n)} \Gamma_i(\boldsymbol{\chi}) \rho(\boldsymbol{\chi}) d\boldsymbol{\chi}. \quad (4.6)$$

Clearly, the expedient calculation of the integral in (4.6) calls for an efficient multivariate quadrature rule on  $\Omega$ . For example, use of the Smolyak sparse grid quadrature [89, 41] leads to the approximation of (4.6) through the summation (see 2.5),

$$c_i \approx \frac{1}{\|\Psi_i\|^2} \sum_{r=1}^M Z_{km}(\boldsymbol{\chi}_r) \Gamma_i(\boldsymbol{\chi}_r) \rho(\boldsymbol{\chi}_r) w_r, \quad (4.7)$$

where the number of nodes,  $M$ , is significantly less than the one required by a tensor product rule. The selection of the quadrature points, their weights  $w_r$ , and the level of accuracy that dictates the sparsity of the Smolyak grid are presented in Chapter 2 and they are well documented in the literature (see [41, 89, 105] for details).

Equations (4.3) and (4.7) define the desired stochastic global impedance

matrix macromodel of the random domain  $V_n$ . The process for its construction is summarized in terms of the following algorithm.

#### Algorithm

1. Choose the dimension of the global impedance matrix and, hence, the number of Fourier modes used in the expansion of the tangential electric and magnetic fields on  $S_n$ .
2. Represent geometric/material randomness in terms of  $D$  independent random variables  $\boldsymbol{\chi} = (\chi_1, \chi_2, \dots, \chi_D)$ .
3. Choose polynomial family and order for truncated polynomial chaos expansion.
4. Generate a Smolyak grid on probability  $D$  dimensional random space  $\Omega$ .
5. For each point  $\boldsymbol{\chi}_r, r = 1, 2, \dots, R$  on the Smolyak grid, solve the deterministic interior BVP to obtain  $\mathbf{Z}^{(n)}(\boldsymbol{\chi}_r)$ .
6. Using the matrices obtained in step 5, calculate the coefficients in the polynomial chaos expansion of  $\mathbf{Z}^{(n)}$  using (4.7).

### 4.3 Solution of the Exterior Stochastic BVP

Once the stochastic global impedance matrices on the fixed circular boundaries  $S_n, n = 1, 2, \dots, N$ , have been constructed, the numerical solution of the electromagnetic scattering problem by the union of the  $N + 1$  targets,  $V_n, n = 1, 2, \dots, N$  amounts to solving an exterior electromagnetic BVP in  $V_E$ . As already stated, since the circular boundaries are fixed, the finite element solution of this exterior BVP requires a single numerical grid. The randomness of each one of the  $N$  regions manifests itself in terms of the polynomial chaos expansions of the elements of its stochastic impedance matrix. With  $D_n$  denoting the number of independent random variables used to parameterize the uncertainty in  $V_n$ , the dimension of the random space  $\Omega_E$  for the exterior stochastic BVP is  $D_E = \sum_{n=1}^N D_n$ . Irrespective of the process

used for the solution of the exterior stochastic BVP, the global impedance matrix on each one of the circular boundaries  $\Omega_E$  is readily computed from its polynomial chaos expansion for each sample in the random space.

## 4.4 Numerical Validation and Demonstration Studies

In this section, several numerical examples involving electromagnetic wave scattering by arrays of infinitely long cylinders are used to validate the proposed methodology and demonstrate its key attributes.

### 4.4.1 Single Cylinder with Random Radius

We begin with the problem of  $TE_z$  time-harmonic uniform plane wave scattering by a perfect electric cylindrical conductor of circular cross section and of random radius,  $a = 0.80(1+\chi)$  m, where  $\chi$  is a Gaussian random variable with zero mean and standard variation of 0.06. The cylinder is immersed in free space and its axis coincides with the  $z$ -axis of the reference coordinate system. The amplitude of the incident magnetic field is 1 A/m and its angular frequency is  $9 \times 10^8$  rad/s. The availability of an analytic solution for this problem makes possible the use of a standard Monte Carlo analysis to calculate the reference solution for the statistics of the scattered magnetic field on a circle of radius 1.2 m centered at the origin. Use of  $10^4$  sampling points in the Monte Carlo process yielded an accuracy of  $10^{-5}$  in the calculation of the mean value of the magnitude of the scattered magnetic field.

Next, the problem was solved making use of the stochastic global impedance condition defined over the circle of radius 1.2 m. The polynomial chaos approximation of the elements of the impedance matrix is in terms of Hermite polynomials up to the third order. The dimension of the impedance matrix is 11. Since the dimension of the random space is 1, the Smolyak grid reduces to a simple Gaussian quadrature rule. For accuracy level of 5, a Smolyak involving five grid points is required for the calculation of the integrals in (4.7). Since the random space for the exterior stochastic BVP is the same with that for the interior, the same Smolyak grid used for the construction of the global impedance matrix is used for solving the exterior stochastic BVP. The mean and variance of the magnitude of the scattered magnetic field thus

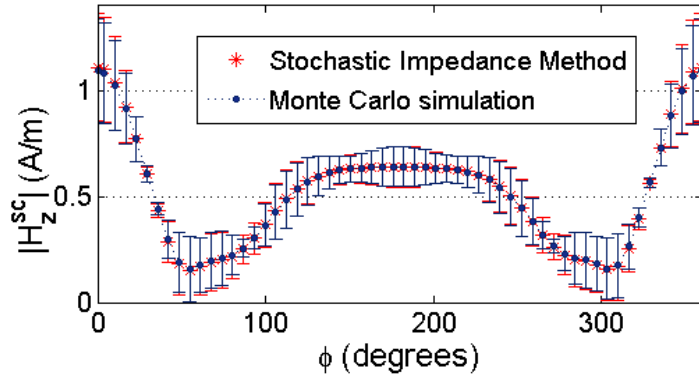


Figure 4.2: Mean value of the magnitude of the scattered magnetic field. Error bars represent  $\pm 3$ std deviation from the mean.

computed are compared with those obtained analytically in Fig. 4.2. The error bars represent a  $\pm 3$ std deviation with respect to the mean. Very good agreement is observed. More specifically, the average error in the mean value of the magnitude of the scattered magnetic field between the analytical and the numerical solution, averaged over all angles, is 1.20%.

#### 4.4.2 Four Elliptical Cylinders – TE<sub>z</sub> Polarization

Next, the case of TE<sub>z</sub> wave scattering by an array of four elliptical cylinders is considered. All cylinders are perfect electric conductors, and the background medium is free space. The angular frequency of the excitation is  $9 \times 10^8$  rad/s. In the absence of any statistical variability, the centers of the four cylinders coincide with the vertices of a square of side 2.4 m (see Fig. 4.3). The randomness in the cross-sectional geometry is introduced through a set of four independent random variables for each cylinder. Two of them,  $\chi_1$ ,  $\chi_2$ , are associated with the lengths  $2a$  and  $2b$  of the major axis (along the  $x$ -axis) and minor axis (along the  $y$ -axis), respectively, of the elliptical cylinder. More specifically, with the two random variables taken to be Gaussian of mean value of 0 and standard deviation of 0.025, the lengths of the two axes (in meters) are given by

$$2a(\chi_1) = 1.4(1 + \chi_1), \quad 2b(\chi_2) = 1.4(1 + \chi_2). \quad (4.8)$$

The other two random variables,  $\chi_x$ ,  $\chi_y$ , control the random displacement

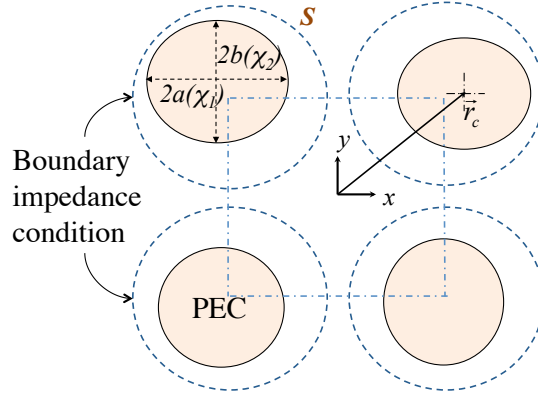


Figure 4.3: Array of four PEC elliptical cylinders with random axes lengths and random positions.

of the center of the cylinder from the vertex of the reference square. The position of the center is given by

$$\vec{r}_c = \vec{r}_o + \hat{x}\chi_x + \hat{y}\chi_y, \quad (4.9)$$

where  $\vec{r}_o$  denotes the corresponding position of the vertex of the square. Variables  $\chi_x$  and  $\chi_y$  are Gaussian random variables of zero mean value and standard deviation of 0.025 m. Even though the same four variables are being used to quantify the geometric uncertainty for each one of the four cylinders, when considering the four-cylinder array, the four sets of random variables are assumed to be independent. Thus, the randomness of the cross-sectional geometry is parameterized in terms of 16 independent random variables.

Depicted in Fig. 4.3 are the four fixed circular boundaries on which stochastic global impedance boundary conditions will be defined, one for each one of the four cylinders. The center for each circle coincides with corresponding vertex of the reference square formed by the unperturbed centers of the four cylinders in the array. The radius of each circle is such that the cylinder associated with it remains enclosed by it for all points in the four-dimensional domain in the random space defined by the random variables  $\chi_1, \chi_2, \chi_x, \chi_y$ . For this specific example, this radius was taken to be 1 m. Given that the random variables are Gaussian distributions, orthogonal Hermite polynomials are used for the polynomial chaos expansion of the elements of the stochastic impedance matrix. The calculation of the coefficients in the polynomial chaos expansion using polynomials of up to second order is carried out efficiently through the use of a Smolyak sparse

grid, on the four-dimensional random space. More specifically, for the case considered here, a Kronrod–Patterson rule [41], [105] of accuracy level 5 was used, resulting in 201 points on the four-dimensional random space. For each point on the Smolyak grid, a finite element solution of the interior BVP was used to calculate a global impedance matrix of dimension 21. The computed matrices were subsequently used for the calculation of the coefficients in the polynomial chaos expansion of the stochastic impedance matrix making use of (4.7).

With the stochastic global impedance matrix available on each one of the four circular boundaries, a finite element model was used for the solution of the exterior stochastic BVP with excitation by a uniform, time-harmonic plane wave propagating in the  $+x$  direction with magnetic field amplitude of 1 A/m. Since the circular stochastic impedance boundaries are fixed, a single finite element mesh is needed for the discretization of the geometry. The only changes to the finite element matrix are those associated with the specific values of the stochastic impedance matrices on the four boundaries for each sample realization in the 16-dimensional random space. Rather than a standard Monte Carlo process, a Smolyak sparse grid of accuracy level 3 was used to extract the statistics of the scattered fields and the radar cross section. The number of points in the sparse Smolyak grid is 513. The mean and variance of the output parameters are computed by performing the integration over the random space. These integrals are approximated by weighted summations of the scattered field, computed at each one of the 513 nodes as previously described,

$$\langle |H_z^{sc}(\rho, \phi)| \rangle \approx \sum_{r=1}^{513} |H_z^{sc}(\rho, \phi, \boldsymbol{\chi}_r)| \rho(\boldsymbol{\chi}_r) w_r, \quad (4.10)$$

$$var(|H_z^{sc}(\rho, \phi)|) \approx \sum_{r=1}^{513} |H_z^{sc}(\rho, \phi, \boldsymbol{\chi}_r)|^2 \rho(\boldsymbol{\chi}_r) w_r - \langle |H_z^{sc}(\rho, \phi)| \rangle^2. \quad (4.11)$$

The calculated scattered magnetic field, sampled on a circle of radius 3.4 m centered at the center of the reference square defined by the unperturbed centers of the four cylinders is depicted in Fig. 4.4. More specifically, shown in the figure is the mean value of the magnitude of the scattered magnetic field along with error bars that indicate a  $\pm 3$ std deviation from the mean

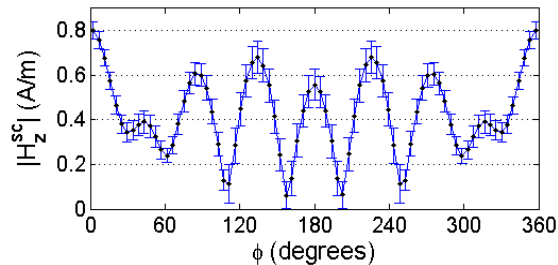


Figure 4.4: Mean value of the magnitude of the scattered magnetic field on a circle of radius 3.8 m enclosing the four cylinders. Error bars represent  $\pm 3$ std deviation from the mean.

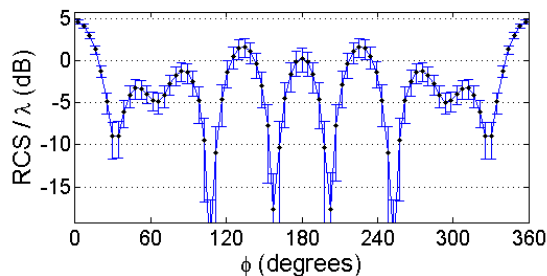


Figure 4.5: Mean value of the radiation cross section (RCS) of the magnetic field. Error bars represent  $\pm 3$ std deviation from the mean.

value. The radar cross section (RCS) is depicted in Fig. 4.5. Again, the mean value is plotted, along with error bars that denote  $\pm 3$ std deviation from the mean.

#### 4.4.3 Array of Elliptical Cylinders – TMz Polarization

The final numerical study considers the case where the polarization of the excitation is TMz with the electric field linearly polarized along the  $z$ -axis. For this case and in view of the fact that for the two-dimensional BVP considered the governing equation is the scalar Helmholtz equation for the  $z$ -component of the magnetic field, a global admittance matrix is used instead of a global impedance matrix. The global admittance matrix relates the Fourier coefficients in the expansion of the tangential magnetic field on each one of the circular boundaries  $S_n$  to the Fourier coefficients in the expansion of the tangential electric field.

For this case, the four-cylinder array depicted in Fig. 4.3 is illuminated by a time-harmonic, line current source of current phasor of 1 A, angular

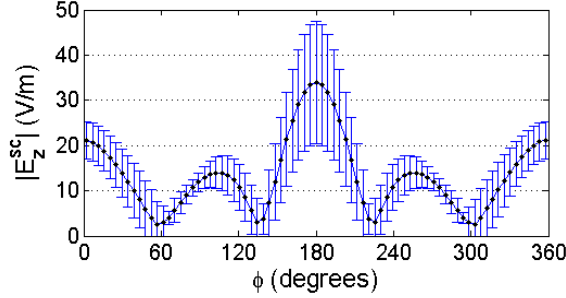


Figure 4.6: Magnitude of the scattered electric field on a circle of radius 3.4 m. Error bars represent  $\pm 3$ std deviation from the mean.

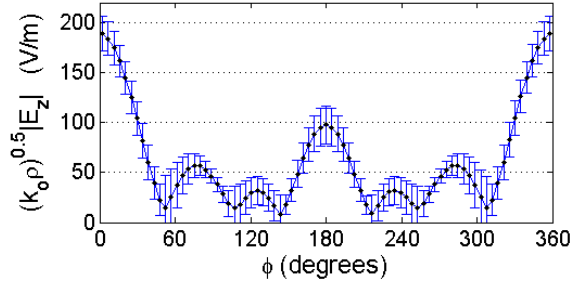


Figure 4.7: Mean value of the magnitude of the far electric field at  $\rho = 1000/k_o$ . Error bars represent  $\pm 3$ std deviation from the mean.

frequency  $9 \times 10^8$  rad/s, and placed at position  $(3, 0)$  m with its axis parallel to the  $z$ -axis. The development of the global stochastic admittance matrix, used on each one of the circular boundaries, was carried out following the same choices for Hermite polynomial chaos expansion order and Smolyak grid accuracy level as in the computation of the impedance matrix for the TEz case.

Using expressions (4.10) and (4.11) the mean and the variance of the magnitude of the  $z$ -component of the scattered electric field were computed. Depicted in Fig. 4.6 is the mean value of the magnitude of the scattered electric field recorded on a circle of radius 3.4 m with its center at the center of the reference square of the four-cylinder array configuration. Also depicted in the figure are error bars indicating  $\pm 3$ std deviation from the mean. The large deviation obtained in the forward scattering direction (on the side of the array where the line source is placed) is attributed to the close proximity of the source to the cylinders. Also depicted in Fig. 4.7 is the mean value of the magnitude of the total electric field for a distance in the far-field region. Again, the error bars represent  $\pm 3$ std deviation from the mean.

## 4.5 Concluding Remarks

In this chapter, a methodology has been proposed and numerically demonstrated for the development of stochastic macromodels of sub-domains of a complex electromagnetic structure exhibiting geometric and/or material randomness. Under the assumption that the randomness inside the sub-domain is parameterized in terms of a set of independent random variables, the proposed methodology abstracts the randomness in the sub-domain in terms of a stochastic global impedance or admittance matrix defined on a fixed surface enclosing the sub-domain. The elements of the matrix are given in terms of truncated polynomial chaos expansions on the random space defined by the independent random variables.

As demonstrated through the numerical examples presented, use of such stochastic macromodels alleviates the computational complexity of the solution of the random scattering problem by eliminating the need for the repeated numerical discretization (e.g., the repeated mesh generation) for the entire structure for each sampling point in the Monte Carlo process.

While the proposed methodology was presented in the context of two-dimensional EM scattering, its extension to three dimensions is rather straightforward. For example, for the case of an ensemble of multiple three-dimensional objects, global stochastic impedance boundary conditions can be defined on spherical surfaces enclosing each object.

Another extension of the proposed macromodeling involves the case where the elements of the stochastic global impedance matrix are functions of frequency. As already demonstrated in [52] and [86], this extension generalizes the concept of stochastic global impedance macromodeling – in a manner consistent with the concept of network matrix representation of passive EM multi-ports – to provide for a broadband stochastic macromodel of a portion of a composite structure exhibiting material and/or geometric randomness. Chapter 5 presents the development of the broadband response.

## Chapter 5

# STOCHASTIC REDUCED-ORDER MACROMODELING

### 5.1 Introduction

In Chapter 4, a stochastic macromodeling methodology was proposed to account for the uncertainty in geometric and material properties of random subdomains. One substantial limitation of the methodology is that it is only valid for a specific frequency. In view of such a constraint, we turn our attention to its generalization for broadband stochastic modeling. Particularly, we are concerned with the development of efficient ways to account for uncertainty (randomness) in geometric and material properties in the finite element modeling of electromagnetic wave phenomena in complex structures with a reduced-order model technique. Along the same lines as the contributions from Chapter 4, of particular interest are structures where such uncertainty is localized, occurring in a finite number of regions inside the structure. For such cases, the numerical electromagnetic analysis of the structure can be expedited by eliminating the repeated mesh generation in a Monte Carlo process required for each sampling point in the random space defined by the independent random variables that parameterize the uncertainty in the structure.

Toward this objective, we develop a stochastic finite-element macromodel for each one of the random regions, with each macromodel defined over a fixed surface enclosing the associated random region. In this manner, the geometry exterior to the union of the random regions is deterministically defined. Thus, a single finite element mesh needs to be generated for the discretization of the overall structure. The only thing that changes for each sample in the Monte Carlo process is the stochastic macromodel for each one of the random regions.

A Krylov subspace Model Order Reduction (MOR) methodology [85] is

used to reduce the size of the finite element model that discretizes the interior of the random region and a sparse stochastic collocation method is used to develop reduced-order macromodels of the state-space representation matrices that are expressed in terms of generalized polynomial chaos expansions over the random space for the region [87].

Numerical studies of electromagnetic wave scattering by random targets are used to highlight the attributes of the proposed stochastic finite element macromodels and demonstrate the computational benefits from their utilization in the numerical modeling of electromagnetic wave interaction with complex structures exhibiting uncertainty. For each iteration of the stochastic simulation, the macromodel defined on the fixed boundary enclosing the random region is used to compute the corresponding transition matrix [104] that relates the coefficients of the tangential scattered and incident fields on the boundary interpolated in terms of appropriate sets of spatial expansion functions. In addition, the transition-matrix formulation is used to solve scattering problems with multiple targets by employing a recursive formulation based on the addition theorem proposed by Chew [104].

## 5.2 Deterministic Transition Matrix

Transition matrix is a well-known concept [104] that relates the incoming modes with the scattered ones by expanding the fields in terms of the Fourier harmonics in the two-dimensional case and the spherical harmonics for the three-dimensional case. In this section, we present a two-dimensional transition matrix formulation in the FEM context to set the deterministic tools for the stochastic transition matrix representation formulated in Section 5.4.

Consider a two-dimensional electromagnetic scattering problem with transverse magnetic polarization. The scatterer is immersed in free space as shown in Fig. 5.1 and bounded by a fictitious circular boundary  $c$  corresponding to the circle with radius  $\rho = \rho_o$ . A finite element method is used to discretize the domain  $\mathcal{D}$  and reduce the Maxwell's equations to a linear system of equations. The Galerkin technique reduces the vector wave equation to [85]

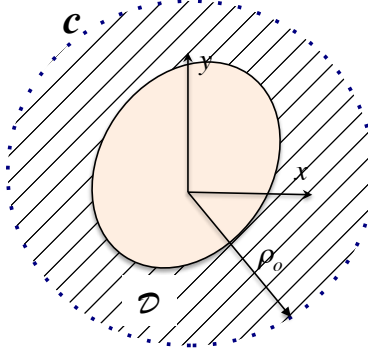


Figure 5.1: Geometry of scatterer. Scattering boundary condition is computed on contour  $c$ .

$$\iint_{\mathcal{D}} (\nabla \times \mathbf{w}_i) \cdot (\nabla \times \mathbf{H}) ds - \iint_{\mathcal{D}} k_o^2 \mathbf{H} \cdot \mathbf{w}_i ds = -j\omega\epsilon_o \int_c (\hat{\mathbf{n}} \times \mathbf{E}_z) \cdot \mathbf{w}_i dl, \quad (5.1)$$

where  $\mathbf{w}_i$  represents the vector basis functions used to expand the magnetic field,

$$\mathbf{H} \approx \sum_{i=1}^{N_e} \mathbf{w}_i x_{h,i}. \quad (5.2)$$

In (5.2), we assume that the spatial domain has been discretized into  $N_e$  finite elements. In order to consider losses we would need to replace  $j\omega\epsilon_o$  by  $j\omega\epsilon_o + \sigma$ .

The incident fields can be expressed in terms of an expansion of the modes. For the  $n$ -th Bessel mode of the incident field we have,

$$E_{z,n}^{inc} = J_n(k\rho) e^{jn\phi}. \quad (5.3)$$

While on the boundary  $c$ , the corresponding  $\phi$ -component of the magnetic field is

$$H_{\phi,n}^{inc} = -\frac{j}{\eta_o} J'_n(ka) e^{jn\phi}. \quad (5.4)$$

The corresponding scattered fields are cast in terms of expansions of Hankel modes. In order to keep the size of the problem small while preserving

the accuracy of the solutions, the number of modes,  $2N_{mod} + 1$ , should be chosen so that  $N_{mod}$  is slightly larger than  $k_o\ell/2$ , where  $\ell$  denotes the largest dimension of the cross section of the scatterer [91, 106]. The coefficients  $T_{mn}$  of the expansion of the scattered fields correspond to the coefficients of the transition matrix,  $\mathbf{T}$ , that relates the amplitudes of the cylindrical modes of the incident and the scattered fields.

$$E_{z,n}^{sc} \approx \sum_{m=-N_{mod}}^{N_{mod}} T_{mn} H_m^{(2)}(ka) e^{jm\phi}, \quad (5.5)$$

$$H_{\phi,n}^{sc} \approx -\frac{j}{\eta_o} \sum_{m=-N_{mod}}^{N_{mod}} T_{mn} H'_m{}^{(2)}(ka) e^{jm\phi}. \quad (5.6)$$

The total  $\phi$ -component of the magnetic field,  $H_\phi = H_\phi^{inc} + H_\phi^{sc}$  on the boundary  $c$  is

$$\sum_{i=1}^{N_e} \hat{\phi} \cdot \mathbf{w}_i x_{h,i} = -\frac{j}{\eta_o} J'_n(ka) e^{jn\phi} - \frac{j}{\eta_o} \sum_{m=-N_{mod}}^{N_{mod}} T_{mn} H'_m{}^{(2)}(ka) e^{jm\phi}. \quad (5.7)$$

Next, by making use of the orthogonality condition of the Fourier harmonics, we get

$$\mathbf{B}^H \mathbf{X}_h = -\frac{2\pi j}{\eta_o} (\mathbf{J}' + \mathbf{H}'^{(2)} \mathbf{T}), \quad (5.8)$$

where the first term of the right-hand side corresponds to the incident magnetic field, while the second term corresponds to the reflected field. The  $(m,m)$ -th entries of diagonal matrices  $\mathbf{J}'$  and  $\mathbf{H}'^{(2)} \in \mathbb{C}^{2N_{mod}+1 \times 2N_{mod}+1}$  are the derivative of the Bessel/Hankel functions of order  $m$ . Also, matrix  $\mathbf{B} \in \mathbb{C}^{N_e \times 2N_{mod}+1}$  has zero entries except for the elements on the artificial circular boundary  $c$ , for which

$$B_{c_{in}} = \int_{c_i} \hat{\phi} \cdot \mathbf{w}_i e^{jn\phi} d\phi, \quad (5.9)$$

where  $c = c_1 \cup c_2 \dots \cup c_{N_c}$  and each sub-contour  $c_i$  corresponds to each mesh element on the boundary. Also, the  $n$ -th column of matrix  $\mathbf{X}_h \in \mathbb{C}^{N_e \times 2N_{mod}+1}$  contains the magnetic field evaluated at angle  $\phi_i$  for the  $n$ -th Bessel mode.

Let us consider now the right-hand side of the weak statement (5.1),

$$-j\omega\varepsilon_o \int_c (\hat{\mathbf{n}} \times \mathbf{E}_z) \cdot \mathbf{w}_i dl = j\omega\varepsilon_o\rho_o \int_0^{2\pi} E_{z,n} \hat{\phi} \cdot \mathbf{w}_i(\phi) d\phi. \quad (5.10)$$

Expressing (5.10) in matrix notation and using (5.1) we obtain,

$$(\mathbf{Z} + s^2\mathbf{P})\mathbf{X}_h = s\varepsilon_o\rho_o\mathbf{B}(\mathbf{J} + \mathbf{H}^{(2)}\mathbf{T}), \quad (5.11)$$

where  $s = j\omega$  and state-space representation matrices  $\mathbf{Z}$  and  $\mathbf{P} \in \mathbb{R}^{N_e \times N_e}$  are given by

$$Z_{ij} = \iint_{\Omega} (\nabla \times \mathbf{w}_i) \cdot (\nabla \times \mathbf{w}_j) ds, \quad (5.12)$$

$$P_{ij} = \varepsilon_o\mu_o \iint_{\Omega} \mathbf{w}_i \cdot \mathbf{w}_j ds. \quad (5.13)$$

Finally, by replacing expression (5.8) into (5.11), we get transition matrix  $\mathbf{T}$ ,

$$\mathbf{T} = -(\mathbf{H}'^{(2)} - j\eta_o\mathbf{Y}\mathbf{H}^{(2)})^{-1}(\mathbf{J}' - j\eta_o\mathbf{Y}\mathbf{J}), \quad (5.14)$$

where the admittance matrix  $\mathbf{Y} \in \mathbb{C}^{2N_{mod}+1 \times 2N_{mod}+1}$  is defined as

$$\mathbf{Y} = \frac{s\rho_o\varepsilon_o}{2\pi} \mathbf{B}^H (\mathbf{Z} + s^2\mathbf{P})^{-1} \mathbf{B}, \quad (5.15)$$

and it is the one described in Chapter 4. The transition-matrix formulation offers the advantage of avoiding the mesh of the surrounding media of the scatterer, provided that such media is homogeneous. The following subsection illustrates the use of the transition matrix in a scattering problem.

### 5.2.1 Using Transition Matrix in a Scattering Problem

Once the transition matrix has been described, we can use it to find the scattered field from any incident wave. For such a purpose, we express the incident electric field in terms of Bessel modes and Fourier harmonics expansion,

$$E_z^{inc} \approx \sum_{n=-N_{mod}}^{N_{mod}} a_n J_n(k\rho) e^{jn\phi}. \quad (5.16)$$

The corresponding scattered field is given in a similar manner,

$$E_z^{sc} \approx \sum_{m=-N_{mod}}^{N_{mod}} b_m H_m^{(2)}(k\rho) e^{jm\phi}. \quad (5.17)$$

On the other hand, for each incident Bessel mode, we have a corresponding series of scattered Hankel modes,

$$E_z^{sc} \approx \sum_n \sum_m a_n T_{mn} H_m^{(2)}(k\rho) e^{jm\phi}. \quad (5.18)$$

Equating (5.17) and (5.18), we get

$$\mathbf{b} = \mathbf{T}\mathbf{a}. \quad (5.19)$$

Finally, the scattered field is

$$\mathbf{x}_e^{sc} = \mathbf{\Xi}\mathbf{H}^{(2)}\mathbf{T}\mathbf{a}, \quad (5.20)$$

where the  $(i, m)$ th entry of matrix  $\mathbf{\Xi}$  is  $e^{jm\phi_i}$  and the entries of vector  $\mathbf{x}_e^{sc}$  correspond to the  $z$ -component of the electric field evaluated at angles  $\phi_i$  at a given radius  $\rho$ .

### 5.3 Multiple Scatterers

So far the transition matrix has been formulated for one single scatterer. Such methodology is an important building block for the study of targets exhibiting stochastic variability and the statistical methodology employing such a concept will be presented in forthcoming sections. In this section, we turn our attention to a transition-matrix based methodology proposed by Chew [104] for the deterministic solution of the electromagnetic scattering by multiple objects. For our purposes, addition theorem is used to change the coordinate system of the electromagnetic fields, that are expressed in terms of wave functions. As a result, an expression for an effective transition matrix is constructed that takes into account the presence of other objects in

the space. Additionally, the application of the formulation avoids the need of meshing the medium in which the scatterer is immersed if such a medium is homogeneous. This attribute results in a more efficient numerical solution of the scattering problem than the formulation proposed in Chapter 4.

### 5.3.1 Addition Theorem

Addition theorem arises in a variety of scattering problems. It expresses the wave functions in one coordinate system, denoted  $i$ , in terms of wave functions of another coordinate system, denoted  $l$  [104].

For the case of cylindrical coordinates, the addition theorem is [104, 91]

$$H_m^{(2)}(k\rho_i)e^{-jm\phi_i} = \begin{cases} \sum_{n=-\infty}^{\infty} J_{n-m}(kd_{il}) H_m^{(2)}(k\rho_l)e^{-jn\phi_l+j(n-m)\phi_d} & \rho_l > d_{il} \\ \sum_{n=-\infty}^{\infty} H_{n-m}^{(2)}(kd_{il}) J_m(k\rho_l)e^{-jn\phi_l+j(n-m)\phi_d} & \rho_l < d_{il} \end{cases}, \quad (5.21)$$

where  $\phi_d$  is the angle formed by the vector that starts at the origin of the coordinate system  $l$  and ends at the center of the coordinate system  $i$ . The parameter  $d_{il}$  is the distance between the origin of the two coordinate systems.

In matrix notation, the addition theorem results in the following transformations

$$\Xi \mathbf{H}^{(2)}(k\rho_i) = \Xi \mathbf{J}(k\rho_l) \boldsymbol{\alpha}^{li}, \quad \rho_l < d_{li}, \quad (5.22)$$

$$\Xi \mathbf{H}^{(2)}(k\rho_i) = \Xi \mathbf{H}^{(2)}(k\rho_l) \boldsymbol{\beta}^{li}, \quad \rho_l > d_{li}, \quad (5.23)$$

$$\Xi \mathbf{J}(k\rho_i) = \Xi \mathbf{J}(k\rho_l) \boldsymbol{\beta}^{li}. \quad (5.24)$$

The last expression was obtained by taking the regular part of (5.22) [104]. In (5.22), (5.23), and (5.24), matrices  $\boldsymbol{\alpha}^{li}$  and  $\boldsymbol{\beta}^{li}$  are given by

$$\alpha_{m,n}^{li} = J_{m-n}(kd_{li})e^{j(n-m)\phi_d}, \quad (5.25)$$

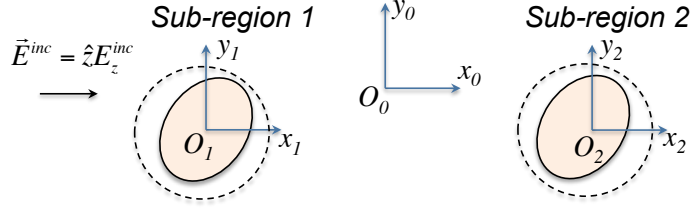


Figure 5.2: Two scatterers in the presence of an incident field.

$$\beta_{m,n}^{li} = H_{m-n}^{(2)}(kd_{li})e^{j(n-m)\phi_a}. \quad (5.26)$$

### 5.3.2 Two Scatterers

In this section, the formulation of the two-dimensional electromagnetic scattering by two objects will be detailed while, for the case of three or more targets, the reader is referred to [104, 107]. Transverse magnetic polarization is assumed as shown in Fig. 5.2, where the geometry of the problem under consideration is depicted. The incident electric field can be expanded in terms of Bessel modes (see (5.16)) and, in matrix notation, it is

$$\mathbf{x}_e^{inc} = \mathbf{\Xi} \mathbf{J}(k\rho_0) \mathbf{a}, \quad (5.27)$$

where the incident field is measured with respect to coordinate system  $O_0$ . The corresponding scattered field is also expressed in terms of Bessel modes,

$$\mathbf{x}_e^{sc} = \mathbf{\Xi} \mathbf{H}^{(2)}(k\rho_1) \mathbf{b}_1 + \mathbf{\Xi} \mathbf{H}^{(2)}(k\rho_2) \mathbf{b}_2. \quad (5.28)$$

Therefore, the total electric field is given by

$$\mathbf{x}_e^{sc} = \mathbf{\Xi} \mathbf{J}(k\rho_0) \mathbf{a} + \mathbf{\Xi} \mathbf{H}^{(2)}(k\rho_2) \mathbf{b}_2 + \mathbf{\Xi} \mathbf{H}^{(2)}(k\rho_1) \mathbf{b}_1. \quad (5.29)$$

Notice that the electric field in (5.29) is expressed in terms of outgoing harmonics in the self-coordinates of the scatterers [104]. To remedy this obstacle, we invoke addition theorem to cast the field in terms of wave functions with respect to one single coordinate system,

$$\mathbf{x}_e = \Xi \mathbf{H}^{(2)}(k\rho_1) \boldsymbol{\beta}^{10} \mathbf{a} + \Xi \mathbf{H}^{(2)}(k\rho_1) \boldsymbol{\alpha}^{12} \mathbf{b}_2 + \Xi \mathbf{H}^{(2)}(k\rho_1) \mathbf{b}_1. \quad (5.30)$$

In (5.30), the first two terms can be viewed as the incident field impinging on the scatterer 1 while the third term is the scattered field from scatterer 1. Next, by definition of the transition matrix (5.19),

$$\mathbf{b}_1 = \mathbf{T}_{1(1)}(\boldsymbol{\beta}^{10} \mathbf{a} + \boldsymbol{\alpha}^{12} \mathbf{b}_2), \quad (5.31)$$

where  $\mathbf{T}_{1(1)}$  is the transition matrix for the isolated scatterer 1 and the parenthesized 1 indicates that it is for one scatterer [104]. Similarly, for the second scatterer,

$$\mathbf{b}_2 = \mathbf{T}_{2(1)}(\boldsymbol{\beta}^{20} \mathbf{a} + \boldsymbol{\alpha}^{21} \mathbf{b}_1). \quad (5.32)$$

Finally, (5.31) and (5.32) can be combined to obtain

$$\mathbf{b}_i = \mathbf{T}_{i(2)} \boldsymbol{\beta}^{i0} \mathbf{a}, \quad (5.33)$$

where  $\mathbf{T}_{i(2)}$  is the two-scatterer transition matrix for the  $i$ -th scatterer. It relates the total scattered field due to the  $i$ -th scatterer to the incident field amplitude when two scatterers are present and is given by [104]

$$\mathbf{T}_{i(2)} \boldsymbol{\beta}^{i0} = (I - \mathbf{T}_{i(1)} \boldsymbol{\alpha}^{il} \mathbf{T}_{i(1)} \boldsymbol{\alpha}^{li}) \mathbf{T}_{i(1)} (\boldsymbol{\beta}^{i0} + \boldsymbol{\alpha}^{il} \mathbf{T}_{l(1)} \boldsymbol{\beta}^{l0}), \quad (5.34)$$

where  $i, l = 1, 2$  and  $i \neq l$  and  $\boldsymbol{\beta}^{i0}$  was included so that the matrix is defined with respect to the self-coordinates of the scatterers.

Therefore, the scattering problem by two objects can be solved by evaluating (5.34), (5.33) and (5.28). The methodology for solving scattering problems involving three or more scatterers is described in [104], where the author Chew proposes a recursive algorithm based on the ideas described in this section to find matrices  $\mathbf{T}_{n(N)}$  that are used to compute the scattered field.

Our proposed formulation is based on the FEM characterization of the targets. Such a description is done in terms of state-space representation matrices that typically have a large size. Therefore, before describing the

use of the discussed techniques in the context of random EM scattering, we introduce a model order reduction methodology to reduce the dimensionality of the problem and, as a consequence, the computational effort associated with the calculation of the macromodel.

## 5.4 Model Order Reduction

The dimension of matrices  $\mathbf{Z}$ ,  $\mathbf{P}$  and  $\mathbf{B}$  (and, hence, the order of the model) depends on the selection of the mesh density. To obtain a good accuracy, a relatively high-dense mesh is often required, especially for targets exhibiting high complexity due to fine features. As a consequence, the dimension of such matrices and the computational cost of the method increases. Model Order Reduction (MOR) provides an alternative to alleviate the computational burden by generating a transformation  $\mathbf{F}$ , which reduces the dimensionality of the problem while preserving the accuracy of the solution. Specifically, the MOR technique with the equation structure preserved, described in [108, 85] is used in the present formulation.

Admittance matrix,  $\mathbf{Y}$ , is expanded at  $s_o$ , which corresponds to a central frequency,  $\omega_o$ , as follows,

$$\mathbf{Y} = -\frac{s}{\eta_o} \mathbf{B}^H \sum_{i=0}^{\infty} \mathbf{r}_i (s - s_o)^i, \quad (5.35)$$

where  $\mathbf{B}^t \mathbf{r}_i$  is the block moment of  $\mathbf{Y}$ .

The moments  $r_i$  can be recursively calculated as

$$\left\{ \begin{array}{l} \mathbf{r}_o = \mathbf{R}, \\ \mathbf{r}_1 = \mathbf{A}_1 \mathbf{r}_o, \\ \mathbf{r}_i = \mathbf{A}_1 \mathbf{r}_{i-1} + \mathbf{A}_2 \mathbf{r}_{i-2}, \quad i \geq 2, \end{array} \right. \quad (5.36)$$

where

$$\begin{aligned} \mathbf{R} &= (\mathbf{Z} + s_o^2 \mathbf{P})^{-1} \mathbf{B}, \\ \mathbf{A}_1 &= -(\mathbf{Z} + s_o^2 \mathbf{P})^{-1} (2s_o \mathbf{P}), \\ \mathbf{A}_2 &= -(\mathbf{Z} + s_o^2 \mathbf{P})^{-1} \mathbf{P}. \end{aligned} \quad (5.37)$$

The generated Krylov subspace is

$$\mathcal{K}_q(\mathbf{A}_1, \mathbf{A}_2; \mathbf{R}) = \text{colsp}[\mathbf{r}_o, \mathbf{r}_1, \dots, \mathbf{r}_{n-1}, r_o, r_1, \dots, r_l], \quad (5.38)$$

where  $q$  is the order of the subspace,  $r_i$  is the  $i$ -th column of the matrix  $\mathbf{r}_n$ ,  $n = \lfloor q/(2N_{mod} + 1) \rfloor$ , and  $l = q - n \cdot (2N_{mod} + 1)$ . It is desired that the dimension of the Krylov subspace  $q$  is much smaller than  $N_e$ . The bases of the Krylov subspace are orthogonalized via the Gram-Schmidt process, to obtain the orthonormal bases,

$$\mathbf{F} = [F_1, F_2, \dots, F_q]. \quad (5.39)$$

Next, we apply the transformation in order to reduce the order of the matrices as follows,

$$\begin{aligned} \tilde{\mathbf{Z}} &= \mathbf{F}^H \mathbf{Z} \mathbf{F}, & \tilde{\mathbf{P}} &= \mathbf{F}^H \mathbf{P} \mathbf{F}, \\ \tilde{\mathbf{B}} &= \mathbf{F}^H \mathbf{B}. \end{aligned} \quad (5.40)$$

Finally, the reduced-order admittance matrix is approximated by

$$\tilde{\mathbf{Y}} = \frac{1}{2\pi} \tilde{\mathbf{B}}^H (\tilde{\mathbf{Z}} + s^2 \tilde{\mathbf{P}})^{-1} (s \varepsilon_o \rho_o \tilde{\mathbf{B}}). \quad (5.41)$$

The corresponding transition matrix can be obtained from (5.41) by using transformation (5.14). This is a frequency-dependent model valid for values of  $s$  near  $s_o$ . Next, we can use this frequency-dependent model to replace the target by a circular boundary and solve a scattering problem with any given incident field for any frequency in the given frequency range.

## 5.5 Stochastic Transition Matrix with Model Order Reduction

Next, we combine the MOR process described above with the polynomial chaos formulation of Section 4.2.3 to obtain a reduced order model where its matrices are cast in terms of an expansion of orthogonal polynomials over the random space. We will make use of the Smolyak sparse grid algorithm to evaluate the expansion coefficients of the matrices to reduce computational cost. Thus, these matrices become functions of the set of random variables describing the geometry and material properties of the target. Finally, the

statistics of the scattered fields for any source and any frequency in the bandwidth of validity of the macromodel can be calculated.

We will use a simple example to explain the approach, namely, the case of scattering by a PEC circular cylinder with random radius given by the expression

$$\rho = \hat{\rho}(1 + \chi), \quad (5.42)$$

where the random variable  $\chi$  follows a Gaussian distribution with zero mean and standard deviation *std*.

Following the formulation presented in [52, 86], we consider the reduced-order random version of equation (5.11) in matrix notation,

$$(\tilde{\mathbf{Z}}_{rand} + s^2 \tilde{\mathbf{P}}_{rand}) \tilde{\mathbf{X}}_{h,rand} = s \varepsilon_o a \tilde{\mathbf{B}}_{rand} (\mathbf{H}^{(1)} + \mathbf{H}^{(2)} \tilde{\mathbf{T}}_{rand}). \quad (5.43)$$

By using the polynomial chaos expansion, matrices  $\tilde{\mathbf{Z}}_{rand}$ ,  $\tilde{\mathbf{P}}_{rand}$ ,  $\tilde{\mathbf{Y}}_{rand}$ ,  $\tilde{\mathbf{X}}_{h,rand}$ , and  $\tilde{\mathbf{T}}_{rand}$  are expanded in terms of an orthonormal set of polynomials,  $\Gamma_i(\chi)$ . For instance, matrix  $\tilde{\mathbf{B}}_{rand}$  is expressed as a truncated summation of orthonormal polynomials as follows,

$$\tilde{\mathbf{B}}_{rand} \approx \sum_{i=0}^P \mathbf{B}_i \Gamma_i(\chi). \quad (5.44)$$

More specifically, the one-dimensional Hermite polynomials are used given the Gaussian distribution of the random variable. The truncated expansion up to  $P = 2$  involves polynomials up to the second order,

$$\begin{aligned} \Gamma_0(\chi) &= 1, \\ \Gamma_1(\chi) &= \chi, \\ \Gamma_2(\chi) &= \frac{1}{\sqrt{2}}(\chi^2 - 1). \end{aligned} \quad (5.45)$$

The Smolyak algorithm is used to compute the coefficients in (5.44) in an expedient way. Making use of the orthogonality of the basis polynomials,

$$\mathbf{B}_i = \int_{\Omega_{rand}} \tilde{\mathbf{B}}_{rand}(\chi) \Gamma_i(\chi) f(\chi) d\chi, \quad (5.46)$$

where  $f(\chi)$  is the PDF of Gaussian random variable  $\chi$ .

The Smolyak algorithm allows us to replace previous multivariate inte-

grals by a finite summation with reduced number of function evaluations (see Chapter 2),

$$\mathbf{B}_i \approx \sum_{r=1}^M \tilde{\mathbf{B}}_{rand}(\chi_r) \Gamma_i(\chi_r) w_r. \quad (5.47)$$

Therefore, the FEM solver needs to be used  $M$  times to characterize the random matrices of the scatterer.

### 5.5.1 Approach 1: Augmented System

Sumant et al. [86] proposed a stochastic FEM methodology to account for the uncertainties in a electromagnetic problem. This approach reduces the stochastic FEM problem to a deterministic one, from which the statistics of the fields can be computed. For such purposes, we replace the random matrices in (5.43) by their corresponding polynomial series expansions,

$$\begin{aligned} & (\mathbf{Z}_o + \mathbf{Z}_1\Gamma_1 + \mathbf{Z}_2\Gamma_2 + s^2(\mathbf{P}_o + \mathbf{P}_1\Gamma_1 + \mathbf{P}_2\Gamma_2)) \\ & (\mathbf{X}_{ho} + \mathbf{X}_{h1}\Gamma_1 + \mathbf{X}_{h2}\Gamma_2) = s\varepsilon_o a (\mathbf{B}_o + \mathbf{B}_1\Gamma_1 + \mathbf{B}_2\Gamma_2) \\ & (\mathbf{J} + \mathbf{H}^{(2)}(\mathbf{T}_o + \mathbf{T}_1\Gamma_1 + \mathbf{T}_2\Gamma_2)). \end{aligned} \quad (5.48)$$

Next, we multiply (5.48) by  $\Gamma_i(\chi) f(\chi)$  and integrate over the random space. For  $i = 0$ , we obtain:

$$\begin{aligned} & (\mathbf{Z}_o + s^2\mathbf{P}_o)\mathbf{X}_{ho} + (\mathbf{Z}_1 + s^2\mathbf{P}_1)\mathbf{X}_{h1} + (\mathbf{Z}_2 + s^2\mathbf{P}_2)\mathbf{X}_{h2} = \\ & s\varepsilon_o a (\mathbf{B}_o\mathbf{J} + \mathbf{B}_o\mathbf{H}^{(2)}\mathbf{T}_o + \mathbf{B}_1\mathbf{H}^{(2)}\mathbf{T}_1 + \mathbf{B}_2\mathbf{H}^{(2)}\mathbf{T}_2), \end{aligned} \quad (5.49)$$

for  $i = 1$ ,

$$\begin{aligned} & (\mathbf{Z}_o + s^2\mathbf{P}_o)\mathbf{X}_{h1} + (\mathbf{Z}_1 + s^2\mathbf{P}_1)(\mathbf{X}_{h1} + \sqrt{2}\mathbf{X}_{h2}) + \\ & + (\mathbf{Z}_2 + s^2\mathbf{P}_2)\sqrt{2}\mathbf{X}_{h1} = s\varepsilon_o a (\mathbf{B}_o\mathbf{H}^{(2)}\mathbf{T}_1 + \\ & \mathbf{B}_1(\mathbf{J} + \mathbf{H}^{(2)}\mathbf{T}_o + \sqrt{2}\mathbf{H}^{(2)}\mathbf{T}_2) + \sqrt{2}\mathbf{B}_2\mathbf{H}^{(2)}\mathbf{T}_1), \end{aligned} \quad (5.50)$$

and for  $i = 2$ ,

$$\begin{aligned} & (\mathbf{Z}_o + s^2\mathbf{P}_o)\mathbf{X}_{h2} + \sqrt{2}(\mathbf{Z}_1 + s^2\mathbf{P}_1)\mathbf{X}_{h1} + \\ & (\mathbf{Z}_2 + s^2\mathbf{P}_2)(\mathbf{X}_{ho} + 2\sqrt{2}\mathbf{X}_{h2}) = s\varepsilon_o a (\mathbf{B}_o\mathbf{H}^{(2)}\mathbf{T}_2 + \\ & \sqrt{2}\mathbf{B}_1\mathbf{H}^{(2)}\mathbf{T}_1 + \mathbf{B}_2(\mathbf{J} + \mathbf{H}^{(2)}\mathbf{T}_o + 2\sqrt{2}\mathbf{H}^{(2)}\mathbf{T}_2)). \end{aligned} \quad (5.51)$$

Collecting previous equations into an augmented equation, we obtain

$$(\mathbf{Z}_{aug} + s^2 \mathbf{P}_{aug}) \mathbf{X}_{h,aug} = s \varepsilon_o a \mathbf{B}_{aug} (\mathbf{J}_{aug} + \mathbf{H}_{aug}^{(2)} \mathbf{T}_{aug}), \quad (5.52)$$

where the augmented matrices are given by

$$\mathbf{Z}_{aug} = \begin{bmatrix} \mathbf{Z}_o & \mathbf{Z}_1 & \mathbf{Z}_2 \\ \mathbf{Z}_1 & \mathbf{Z}_o + \sqrt{2} \mathbf{Z}_2 & \sqrt{2} \mathbf{Z}_1 \\ \mathbf{Z}_2 & \sqrt{2} \mathbf{Z}_1 & \mathbf{Z}_o + 2\sqrt{2} \mathbf{Z}_2 \end{bmatrix}, \quad (5.53)$$

$$\mathbf{P}_{aug} = \begin{bmatrix} \mathbf{P}_o & \mathbf{P}_1 & \mathbf{P}_2 \\ \mathbf{P}_1 & \mathbf{P}_o + \sqrt{2} \mathbf{P}_2 & \sqrt{2} \mathbf{P}_1 \\ \mathbf{P}_2 & \sqrt{2} \mathbf{P}_1 & \mathbf{P}_o + 2\sqrt{2} \mathbf{P}_2 \end{bmatrix}, \quad (5.54)$$

$$\mathbf{B}_{aug} = \begin{bmatrix} \mathbf{B}_o & \mathbf{B}_1 & \mathbf{B}_2 \\ \mathbf{B}_1 & \mathbf{B}_o + \sqrt{2} \mathbf{B}_2 & \sqrt{2} \mathbf{B}_1 \\ \mathbf{B}_2 & \sqrt{2} \mathbf{B}_1 & \mathbf{B}_o + 2\sqrt{2} \mathbf{B}_2 \end{bmatrix}, \quad (5.55)$$

$$\mathbf{X}_{h,aug} = \begin{bmatrix} \mathbf{X}_{ho} \\ \mathbf{X}_{h1} \\ \mathbf{X}_{h2} \end{bmatrix}, \quad \mathbf{J}'_{aug} = \begin{bmatrix} \mathbf{J}' \\ 0 \\ 0 \end{bmatrix}, \quad (5.56)$$

$$\mathbf{H}'_{aug}^{(2)} = \begin{bmatrix} \mathbf{H}'^{(2)} & 0 & 0 \\ 0 & \mathbf{H}'^{(2)} & 0 \\ 0 & 0 & \mathbf{H}'^{(2)} \end{bmatrix}, \quad (5.57)$$

and

$$\mathbf{T}_{aug}^{(2)} = \begin{bmatrix} \mathbf{T}_o \\ \mathbf{T}_1 \\ \mathbf{T}_2 \end{bmatrix}. \quad (5.58)$$

In a similar fashion, the tangential component of the magnetic field on the circular boundary can be expressed as an interpolation of orthogonal Hermite polynomials. The random reduced version of equation (5.8) is given by

$$\tilde{\mathbf{B}}_{rand}^H \tilde{\mathbf{X}}_{h,rand} = -\frac{2\pi j}{\eta_o} (\mathbf{J}' + \mathbf{H}'^{(2)} \mathbf{T}_{rand}). \quad (5.59)$$

Next, by using the same approach as the one employed to obtain (5.52), we have

$$\mathbf{B}_{aug}^H \mathbf{X}_{h,aug} = -\frac{2\pi j}{\eta_o} (\mathbf{J}'_{aug} + \mathbf{H}'_{aug}{}^{(2)} \mathbf{T}_{aug}). \quad (5.60)$$

Using (5.60) into (5.52) we get,

$$\begin{aligned} \mathbf{T}_{aug} = & -(\mathbf{H}'_{aug}{}^{(2)} - j\eta_o \mathbf{Y}_{aug} \mathbf{H}'_{aug}{}^{(2)})^{-1} \\ & (\mathbf{J}'_{aug} - j\eta_o \mathbf{Y}_{aug} \mathbf{J}_{aug}), \end{aligned} \quad (5.61)$$

where

$$\mathbf{Y}_{arg} = \frac{s\epsilon_o a}{2\pi} \mathbf{B}_{aug}^H (\mathbf{Z}_{aug} + s^2 \mathbf{P}_{aug})^{-1} \mathbf{B}_{aug}. \quad (5.62)$$

In this manner, we have reduced a random problem to a deterministic expression of dimension three times larger than the original one.

#### 5.5.1.1 Using Transition Matrix in Stochastic Scattering Problems

Following the same formulation as the deterministic problem described in Section 5.2.1, the scattered electric field is computed,

$$\mathbf{x}_{e,rand}^{sc} = \mathbf{\Xi} \mathbf{H}^{(2)} \mathbf{T}_{rand} \mathbf{a}, \quad (5.63)$$

where matrix  $\mathbf{\Xi}_{im} = e^{jm\phi_i}$ , and the entries of vector  $\mathbf{x}_{e,rand}^{sc}$  correspond to the random  $z$ -component of the electric field evaluated at angles  $\phi_i$  at a given radius  $\rho$ . The stochastic problem can be reduced to the deterministic augmented expression

$$\mathbf{x}_{e,aug}^{sc} = \mathbf{\Xi}_{aug} \mathbf{H}_{aug}^{(2)} \mathbf{T}_{aug} \mathbf{a}, \quad (5.64)$$

where

$$\mathbf{\Xi}_{aug} = \begin{bmatrix} \mathbf{\Xi} & 0 & 0 \\ 0 & \mathbf{\Xi} & 0 \\ 0 & 0 & \mathbf{\Xi} \end{bmatrix}, \quad (5.65)$$

$$\mathbf{x}_{e,aug}^{sc} = \begin{bmatrix} \mathbf{x}_{e,o}^{sc} \\ \mathbf{x}_{e,1}^{sc} \\ \mathbf{x}_{e,2}^{sc} \end{bmatrix}. \quad (5.66)$$

In (5.66),  $\mathbf{x}_{e,j}^{sc}$  represents the  $j$ -th expansion vector coefficient of the poly-

nomial chaos representation of the scattered electric field evaluated at angles  $\phi_i$  on the boundary  $c$ . It can be shown that the mean and standard deviation of the scattered electric field are  $mean(\mathbf{x}_{e,rand}^{sc}) = \mathbf{x}_{e,o}^{sc}$  and  $std(\mathbf{x}_{e,rand}^{sc}) = \sqrt{|\mathbf{x}_{e,1}^{sc}|^2 + |\mathbf{x}_{e,2}^{sc}|^2}$ .

### 5.5.2 Approach 2: Direct Interpolation

Instead of expanding the full-order matrices and coming up with an augmented deterministic system, the reduced-order random matrices,  $\tilde{\mathbf{Z}}_{rand}$ ,  $\tilde{\mathbf{P}}_{rand}$ , and  $\tilde{\mathbf{B}}_{rand}$  can be expanded in terms of the polynomial chaos and their coefficient matrices, stored. Such coefficients characterize the random object under consideration. For example, for the case of matrix  $\tilde{\mathbf{Z}}_{rand}$ , we have

$$\tilde{\mathbf{Z}}_{rand} \approx \sum_{i=0}^P \mathbf{Z}_i \Gamma_i(\chi), \quad (5.67)$$

where the matrix coefficients  $\mathbf{Z}_i$ ,  $i = 1, 2, \dots, P$  characterize the random scatterer.

Once the random matrices have been characterized, one can proceed to compute the statistics of the scattered field by computing the reduced-order admittance/impedance matrix and the corresponding transition matrix. The clear advantage of this method is that the size of the final system does not increase with the order of the employed interpolation polynomials as in the first approach. On the other hand, the formulation does not present the advantage of obtaining the mean and standard deviation directly as the augmented-system approach does. The formulation is summarized in the following algorithms.

Algorithm: Characterization of random scatters

1. Choose the dimension of the global impedance matrix and, hence, the number of Fourier modes used in the expansion of the tangential electric and magnetic fields on the boundary surrounding the target.
2. Represent geometric/material randomness in terms of  $D$  independent random variables  $\chi = (\chi_1, \chi_2, \dots, \chi_D)$ .

3. Choose the polynomial family and order for the truncated polynomial chaos expansion.
4. Generate a Smolyak grid on the probability space  $\Omega$ .
5. For each point  $\boldsymbol{\chi}_r, r = 1, 2, \dots, M$ , on the Smolyak grid, solve the deterministic interior BVP to obtain the reduced macromodel in terms of the state-space representation matrices,  $\tilde{\mathbf{Z}}(\boldsymbol{\chi}_r), \tilde{\mathbf{P}}(\boldsymbol{\chi}_r), \tilde{\mathbf{B}}(\boldsymbol{\chi}_r)$ .
6. Using the matrices obtained in step 5, calculate the coefficients in the polynomial chaos expansion of  $\tilde{\mathbf{Z}}(\boldsymbol{\chi}), \tilde{\mathbf{P}}(\boldsymbol{\chi}), \tilde{\mathbf{B}}(\boldsymbol{\chi})$ .

Algorithm: Computation of statistics of scattered field

1. For each realization in the random space,  $\boldsymbol{\chi}_r$ , where  $r = 1, 2, \dots, M_{sc}$ 
  - (a) Compute matrices  $\mathbf{Y}(\boldsymbol{\chi}_k)$  and  $\mathbf{T}(\boldsymbol{\chi}_k)$  by evaluating equations (5.15) and (5.14). For the case of  $N$  targets, compute matrices  $\mathbf{T}_{i(1)}(\boldsymbol{\chi}_{i,k})$  and  $\mathbf{T}_{i(N)}(\boldsymbol{\chi}_{i,k}), i = 1, 2, \dots, N$  as indicated in Section 5.3 and reference [104].
  - (b) Find the scattered field for a given incidence by evaluating (5.20) or (5.29).
2. Gather results and calculate the statistics of the scattered field at the frequency of interest.

## 5.6 Numerical Studies

The proposed formulation has been used to characterize an infinitely long PEC circular cylinder of radius

$$\rho = 0.5(1 + \chi)\text{m}, \quad (5.68)$$

where  $\chi$  is a Gaussian random variable with zero mean and standard deviation 0.1. The cylinder is immersed in free space and is centered at the origin of the reference coordinate system. The enclosing boundary is a circle of radius  $\rho_o = 1$  m centered at the origin as depicted in Fig. 5.3. The number

of employed Fourier modes is  $(2N_{mod} + 1) = 11$  and the expansion point used in the stochastic MOR technique is  $s_o = 10^7 \text{rad/s}$ . As a result, the FEM state-space representation matrices are reduced to a size  $q = 33$  and an interpolation over the random space of matrices  $\tilde{\mathbf{Z}}_{rand}$ ,  $\tilde{\mathbf{P}}_{rand}$ , and  $\tilde{\mathbf{B}}_{rand}$  is obtained in terms of orthonormal polynomials as described in (5.67). In order to obtain the expansion coefficients of the polynomial chaos (PC) expansion, an integration grid of accuracy level  $k = 5$  requires only five electromagnetic solutions of the structure in the one-dimensional random space.

With this interpolation available, we can proceed with finding the statistics of the scattered field for a given excitation using any one of the two proposed approaches. Validations are provided through comparisons with corresponding Monte Carlo solutions of the analytical formulation of plane wave scattering. Additionally, a TMz current line source is considered and an example involving two random scatterers is simulated by using a recursive algorithm proposed by Chew [104].

### 5.6.1 Single Cylinder with Random Radius and Plane Wave Incidence

The *augmented system* and the *direct interpolation* approaches are applied to solve the random EM scattering problem shown in Fig. 5.3 with the geometric perturbation defined in (5.68). The amplitude of the transverse-magnetic (TMz) polarized incident field is 1 V/m and the position of the sampled scattered electric field is indicated in Fig. 5.3. The results are compared with  $2 \times 10^4$  Monte Carlo solutions of the analytical Mie series [109]. In contrast with the MC simulation our methodology requires only five evaluations of the macromodel to calculate the corresponding transition matrices by means of (5.15) and (5.14) and the scattered field with (5.19) and (5.17). Such values were used in a one-dimensional quadrature rule to find the statistical moments of the scattered electric field.

Figure 5.4 shows the mean and standard deviation of the  $z$ -component of the scattered electric field with respect to the normalized wavenumber,  $k_o \rho_o$ , for the case of an incident plane wave impinging the scatterer as shown in Fig. 5.3, calculated with four techniques. The first of such methods is the Monte Carlo simulation of the analytical Mie series which is assumed to be

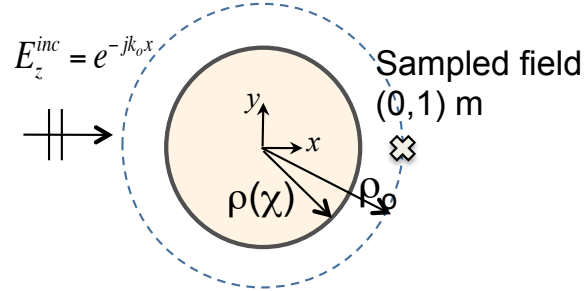


Figure 5.3: Geometry of the studied problem. The field is sampled at the position (0,1) m.

our reference solution. The *augmented system* approach is also employed with first- and second-order polynomials, as well as the *direct interpolation* approach. In general, we observe that the farther the wavenumber is from the selected expansion point, the worse the accuracy is in our numerical approaches, as expected from the construction of the MOR technique. Additionally, it is clear that the *augmented system* approach of first- and even second- order is less accurate than the *direct interpolation* approach. Due to its better convergence, the *direct interpolation* technique is used in the remaining numerical studies.

### 5.6.2 Single Cylinder with Random Radius and Line Current Excitation

In our next example, we consider the same PEC cylinder structure from the previous example with a random radius given by expression 5.68. In this case, the cylinder is illuminated by a time harmonic line source with magnitude 1A located at position (3,0)m as indicated in Fig. 5.5. Results of the simulation are shown in Fig. 5.6 where we have depicted the mean and standard deviation of the scattered electric field as a function of the wavenumber sampled at the coordinates (0,1)m and obtained with  $2 \times 10^4$  Monte Carlo solutions of the analytical Mie series as well as with the reduced-order *direct interpolation* technique that employs only five evaluations to calculate the corresponding statistical moments of the electric field. In general, we observe a good agreement between the numerical and analytical approaches. Additionally, with this example we can demonstrate the versatility of the stochastic macromodel that can be used for any incident field.

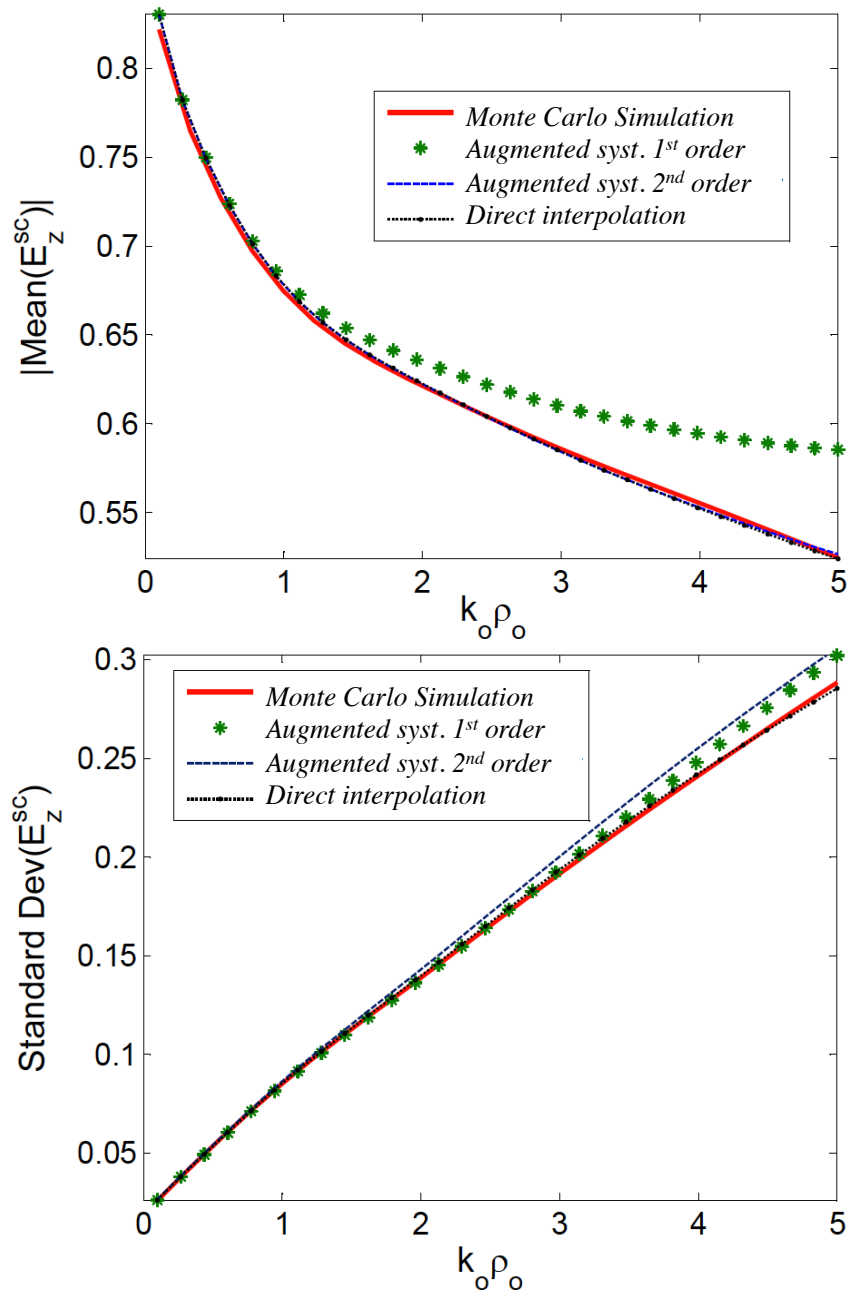


Figure 5.4: Monte Carlo simulation based on the analytical Mie scattering solution is compared to the *augmented system* approach of the first- and second-order and the *direct interpolation* approach. The field has been sampled at  $\phi = \pi$ ,  $\rho = 1$  m.

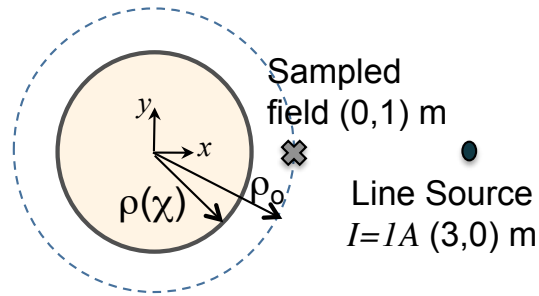


Figure 5.5: Setup of the line source simulation. The PEC circular cylinder has a random radius and the line source is located at the position  $(3, 0)$  m.

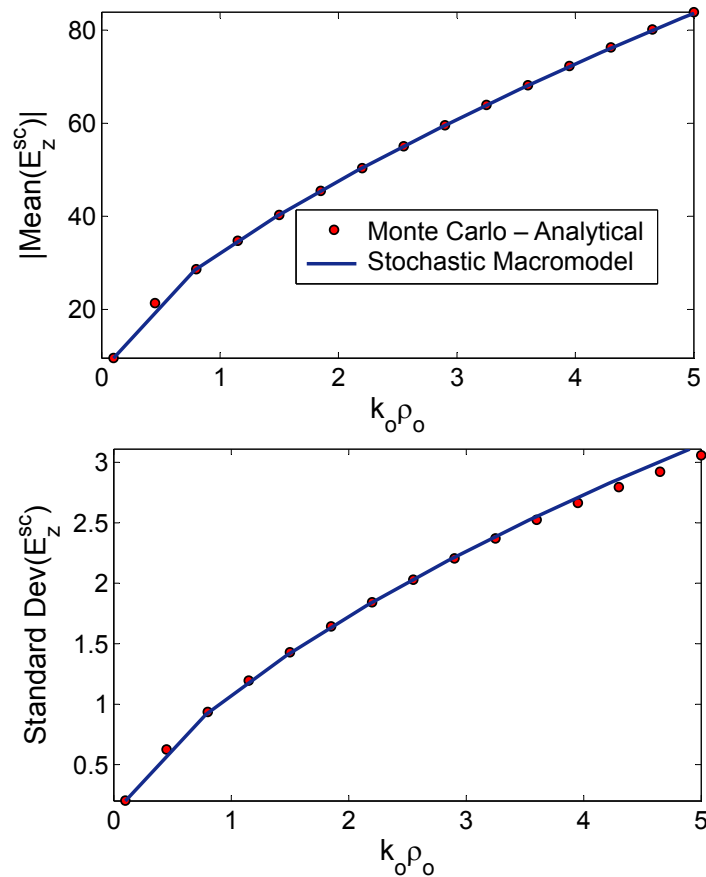


Figure 5.6: The simulation results of the problem to the scattering problem depicted in Fig. 5.5, obtained with the direct interpolation stochastic macromodeling and Monte Carlo solution of the analytical Mie series. The plots show the mean value (top) and standard deviation (bottom) of the  $z$ -component of the scattered electric field sampled at  $(0, 1)$  m with respect to the normalized wavenumber.

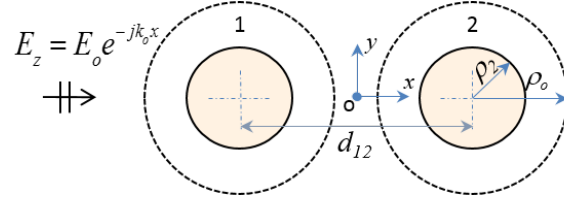


Figure 5.7: Geometry of two PEC circular cylinders each with a random radius, given by  $\rho_i = 0.5(1 + \chi_i)$ , for  $i = 1, 2$  and  $\chi_i \sim \mathcal{N}(0, 0.1)$ . The separation distance between the centers of the cylinders is  $d_{12} = 2.4$  m and the radius of the artificial boundaries is  $\rho_o = 1$  m. The cylinders are impinged by a plane wave with amplitude 1 V/m directed along the  $x$ -axis.

### 5.6.3 Two Cylinders with Plane Wave Incidence

One last example employing the reduced-order macromodel of the PEC circular cylinder structure shown in Fig. 5.3 with random radius given by (5.68) is considered. Specifically, two of such structures located 2.4 m apart from each other as depicted Fig. 5.7 are illuminated by a plane-wave with transverse-magnetic polarization and electric field magnitude of 1 V/m. The stochastic collocation scheme employs 29 evaluations of the macromodel and electric field corresponding to a sparse grid of dimension two and accuracy level,  $k = 3$ .

The reduced-order stochastic macromodeling approach based on the *direct interpolation* formulation was used in combination with the transition-matrix based algorithm for multiple scatterers described in Section 5.3.2 to calculate the radiation cross section of the structure from Fig. 5.7. Such formulation was validated with the full-order stochastic macromodeling approach that follows the formulation from Chapter 4, where a stochastic admittance matrix boundary condition is imposed in each one of the artificial fixed boundaries surrounding the objects. In contrast with the full-order macromodel, the reduced-order model does not require the meshing of the surrounding media because the targets are immersed in a homogeneous medium, resulting in a more computationally efficient methodology.

The radiation cross sections obtained by means of the two methods are shown in Fig. 5.8. It is clear that good agreement is observed in both approaches while the reduced-order methodology is computationally more efficient due to the reduction in the size of the state-space representation matrices and the absence of the surrounding mesh.

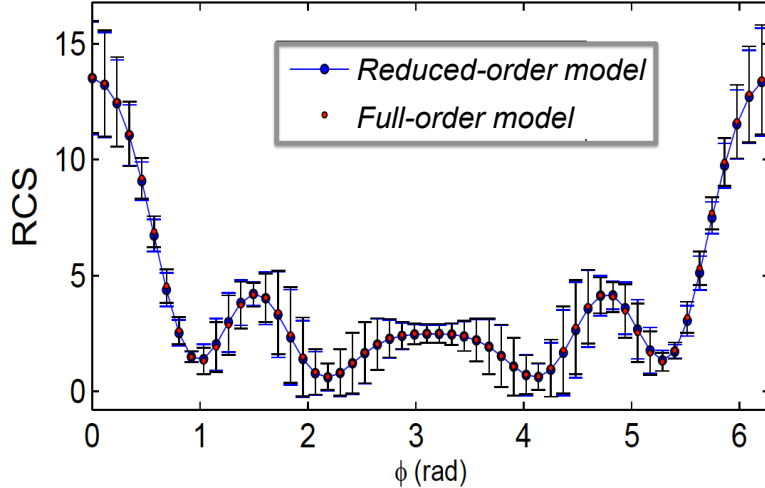


Figure 5.8: Radiation Cross Section (RCS) of two random cylinders with error bars representing  $\pm 3\text{std}$  deviation from the mean value. The centers are 2.4 m apart and the frequency is 118 MHz.

## 5.7 Concluding Remarks

A formulation to study electromagnetic scattering by targets exhibiting uncertainty was proposed. The methodology characterizes the reduced-order state-space FEM matrices in terms of an expansion of orthogonal polynomials of the random variables that characterize the uncertainty. The result is a stochastic broadband macromodel of the subdomain that is employed next in the solution of stochastic scattering problems. In the iterations of a stochastic collocation scheme transition matrix that relates the wave functions of the incident field with the outgoing wave functions of the scattered field is computed. The use of a transition matrix avoids the need of meshing the surrounding media of the targets provided that the media is homogeneous. Additionally, the methodology can handle multiple scatterers by using a recursive algorithm based on the addition theorem.

Several scattering problems have been used to assess the accuracy of the methodology by comparing the simulations with Monte Carlo solutions of the Mie series for cylindrical objects. It is demonstrated that the proposed framework is more accurate than previously published works [86]. With regard to the efficiency of the reduced-order macromodeling technique, it comes from the reduction of the size of the state-space representation matrices and the absence of the surrounding mesh.

## Chapter 6

# STOCHASTIC SIGNAL INTEGRITY ANALYSIS OF INTERCONNECTS

### 6.1 Introduction

Another important application of computational electromagnetics concerns the study of the degradation of electrical signals as they are transmitted in electronic circuits known as signal integrity. The existing numerical tools for the accurate deterministic predictive models is well understood and rigorous solvers [6] are available. In recent years, several researchers have published a number of papers [38, 39, 37, 48, 110] that treat the problem of high-speed interconnects exhibiting uncertainty. For most of the mentioned works, the variability is assumed to occur from one structure to the next so that the geometry and electrical properties are uniform within each manufactured structure, in other words, they treat problems with global variability. The intention of this chapter is to focus on variability that exists localized within the structure itself, resulting in nonuniform geometries and electrical properties within an interconnect link. Due to the complexity of this kind of problem, only a limited number of stochastic applications are found in the literature (e.g. [40, 111, 112]) .

In this chapter, a general methodology is proposed in Section 6.2 and two study cases are analyzed. The first one, presented in Section 6.3 is a methodology for the assessment of interconnects with random permittivity profiles, and the second example, shown in Section 6.4 is a methodology for the assessment of the impact of the interconnect routing variability on signal degradation. For our purposes, as in previous chapters, stochastic macromodeling techniques are employed.

## 6.2 Proposed Methodology

Even though the statistical approaches to treat signal integrity applications exhibiting uncertainty might vary from case to case, a general algorithm can be recognized to perform statistical assessment of interconnects. The first step is the definition of the random space in terms of a finite set of random variables and their corresponding PDFs and correlations. If possible, principal component analysis (see Chapter 3) is applied to orthogonalize and reduce the dimensionality of the random space. Next, a parametric frequency-domain macromodel of the structure is extracted. Such a model is usually given by the scattering parameters. With the macromodel in hand, an efficient Monte Carlo simulation is performed. In each MC iteration, the load and source conditions are imposed and the voltage waves are computed. The final result is given by the time-domain voltage curves computed with an inverse fast Fourier transform (IFFT) applied to the frequency-domain signals. After gathering these simulations, the statistics of the voltage signals can be computed. The algorithm is summarized next.

### Algorithm

1. Characterize the random space in terms of a finite set of random variables.
2. Use Principal Component Analysis to orthogonalize and reduce the random space.
3. Extract a frequency-domain parametric macromodel of the structure.
4. Perform a Monte Carlo simulation using the macromodel. For each iteration of the simulation:
  - (a) Generate a large set of random samples of the input random parameters.
  - (b) Evaluate the macromodel for each sample.
  - (c) Impose load and source conditions.
  - (d) Calculate the set of voltage curves.
  - (e) Apply IFFT to extract the time-domain curves.

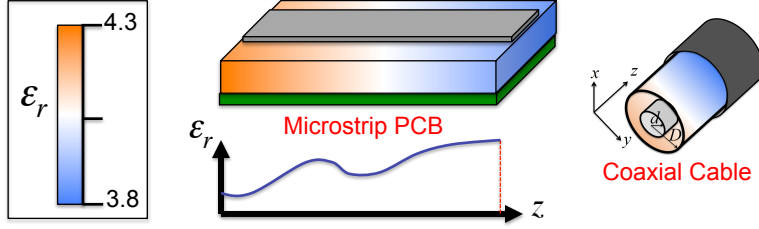


Figure 6.1: Transmission lines exhibiting random variability in the permittivity along the longitudinal axes.

5. Gather results and calculate the statistics of the time-domain signals.

Next, two stochastic examples exhibiting uncertainty are evaluated and the proposed methodology is employed to perform the statistical assessment.

### 6.3 Case Study 1: Transmission Lines with Random Permittivity Profiles

For this particular signal integrity example, we assume that a coaxial cable presents variability in permittivity of the dielectric of its substrate as shown in Fig. 6.1. Such permittivity changes throughout the longitudinal direction of the cable. Our goal is to present a homogenization methodology to capture the variability in the permittivity of transmission lines in terms of an effective permittivity that simplifies the statistical electromagnetic simulation of the structure, as shown in Fig. 6.2.

The permittivity profile is presented as a correlated chain of  $N$  random variables. The dimensionality of the input space is reduced to an  $n$  dimensional random space by means of Principal Component Analysis (PCA). Therefore, the complexity of the model is reduced and subsequent calculations are simplified. With this context in mind, we recognize that we are dealing with a non-uniform transmission line (NTL) problem. The traditional approach to solve an NTL is based on the concatenation of ABCD matrices [113]. The idea of the mentioned approach is to describe the overall electromagnetic response of the system by taking the product of the individual ABCD matrices corresponding to each segment with uniform properties as it is done in the next example. In the present study case, however, we make use of a frequency-domain one-dimensional Finite Element Method (FEM)

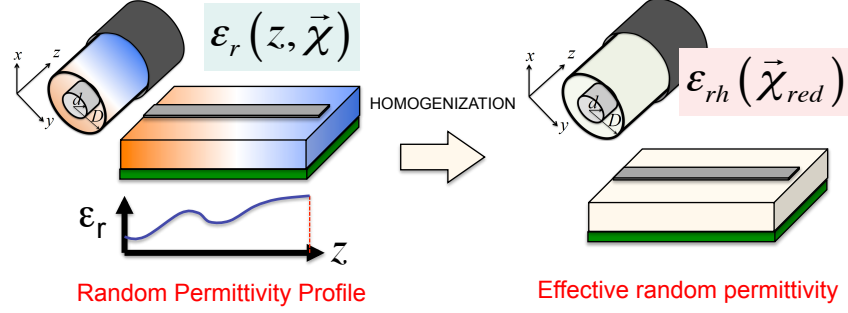


Figure 6.2: Proposed homogeneous stochastic model.

for the electromagnetic simulation in combination with a Polynomial Chaos (PC) expansion formulation [36] to characterize the impact of uncertainty on the transmission properties of the line as a function of the input random parameters. Sparse grid integration is also employed to reduce the cost of the integration associated with the PC construction.

It is found that the random non-uniformity is manifested as a perturbation in the propagation constant which results in a deviation of the propagation time suffered by the wave as it travels down the random structure. The quantification of the induced jitter is necessary for the appropriate signal integrity assessment of the line since it can potentially introduce undesired distortion and synchronization defects.

### 6.3.1 Statistical Characterization

The permittivity of the surrounding medium is assumed to vary along the longitudinal dimension of the line ( $z$ -direction) according to the expression

$$\epsilon_r(z_i) = \epsilon_{rm} + \text{std}(\epsilon_{ri})\chi_i, \quad (6.1)$$

where  $\chi_i$  is assumed to be a Gaussian random variable with zero mean and unit variance, and  $\epsilon_{rm}$  and  $\text{std}(\epsilon_{ri})$  are the mean and standard deviation of the permittivity measured at every position. It is assumed that these quantities are constant for all the segments of the line as shown in Fig. 6.3. The correlation between two random variables corresponding to two different positions,  $z_i$  and  $z_j$  is assumed to follow a Gaussian function that depends on the separation between such positions and is given by

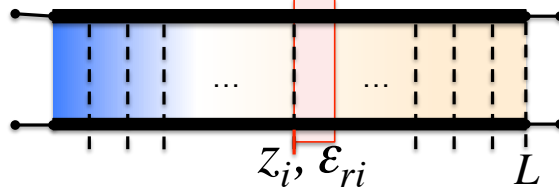


Figure 6.3: Transmission line discretized in sections with uniform permittivity.

$$\Sigma_{ij} = e^{-(|z_i - z_j|/\ell)^2}, \quad (6.2)$$

where parameter  $\ell$  is known as correlation length and quantifies the size of the permittivity fluctuations in the dielectric. This function ensures that the profile is continuous and smooth. Other properties, such as the conductivity, cross section or even random bending of the wires can be considered to vary in a similar fashion.

Once the permittivity has been defined it is noticed that the number of random variables equals the number of elements used in the discretization of the transmission line,  $N$ . Also, the length of each discrete section,  $dl = L/N$  must satisfy the condition  $dl < \min\{\lambda_{min}/10, \ell/10\}$  in order to ensure that the EM solution and statistical description of the profile are accurate.

As already mentioned, the goal is to obtain a stochastic effective permittivity constant that can then be used as a homogeneous property of an uniform line with equivalent transmission properties. Such permittivity is interpolated in terms of a set of basis functions of the input random variables. For a particular realization of the permittivity profile, this homogeneous constant is obtained with an FEM solver that extracts the scattering parameters and the corresponding propagation constant from which the effective permittivity is calculated. The computational effort required by the interpolation technique is related to the dimensionality of the problem. For example, in the case of a tensor grid interpolation [14], the number of required FEM simulations grows exponentially with the number of dimensions of the random space as  $q^N$ , where  $q$  is the number of samples taken along each random variable. Such computational barrier can be overcome by reducing the original random space of dimension  $N$  to a space of size  $n \ll N$  composed by the uncorrelated components presenting the largest variability. The reduced dimensionality algorithm is described next.

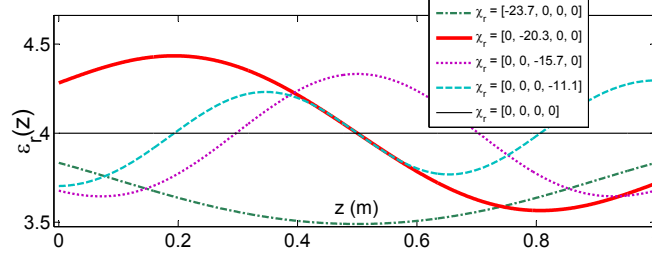


Figure 6.4: First four principal components of the permittivity profile along the transmission line.

### 6.3.2 Random Space Dimensionality Reduction

As already pointed out, the number of random variables  $N$  equals the number of FEM grid segments of the structure. Since a relatively large number of discretized segments is required to obtain accurate results, the dimension of the random space grows accordingly. Therefore, advantage is taken of the existing correlation between the variables to reduce the random space through a Principal Component Analysis (PCA). Figure 6.4 presents the permittivity profiles of the first four principal orthogonal components of the considered transmission line of length  $L = 1$  m, correlation length  $\ell = 25$  cm, mean permittivity,  $\varepsilon_{rm} = 4$  and  $\text{std}(\varepsilon_{ri}) = 0.15$ . The ratio  $L/\ell = 4$  is the minimum number of components required to obtain an accurate model. For this example, such number of components provide a cumulative percentage variation of 94%.

### 6.3.3 Construction of Stochastic Homogeneous Model

With the statistical framework in hand, the electromagnetic simulation and subsequent homogenization are described. For each FEM simulation associated with the construction of the interpolation of the effective homogeneous permittivity model, the position-dependent RLGC parameters of the line are required. In the case of a coaxial cable, there is a straightforward relation between capacitance per unit length and permittivity,

$$C(z) = \frac{2\pi\varepsilon_o\varepsilon_r(z)}{\ln(D/d)}, \quad (6.3)$$

where  $D$  and  $d$  are the external and internal radius of the cable, respectively. When other structures are studied, for example a stripline, a polynomial

expansion can be employed to characterize the RLGC parameters in terms of the varying material properties and/or geometry as described in [37].

We proceed to find a representation of the effective homogeneous permittivity constant through a polynomial chaos expansion [36] ,

$$\tilde{\varepsilon}_r(\boldsymbol{\chi}_{red}) = \sum_{i=0}^P \alpha_i \Gamma_i(\boldsymbol{\chi}_{red}), \quad (6.4)$$

where the multivariate polynomials  $\Gamma_i(\boldsymbol{\chi}_{red})$  depend on the type of random variables. For the case of Gaussian random variables, Hermite polynomials are employed. The number of polynomials,  $P$ , is given by  $(n+p)!/n!p!$  where  $p$  is the maximum order of the employed polynomials. At this point, we see the benefits of using PCA since it reduces the number of required polynomials. Coefficients  $\alpha_i$ 's of expansion (6.4) are obtained by integrating in the random domain  $\Omega$  and by making use of the orthogonality condition of the polynomials,

$$\alpha_i = \int_{\Omega} \tilde{\varepsilon}_r(\boldsymbol{\chi}_{red}) \Gamma_i(\boldsymbol{\chi}_{red}) \rho(\boldsymbol{\chi}_{red}) d\boldsymbol{\chi}_{red}. \quad (6.5)$$

Such integrals are efficiently computed with the use of a sparse grid quadrature rule, so that integral shown above is approximated to a summation of function evaluations by employing the multivariate quadrature tool provided by Heiss [41]:

$$\alpha_i \simeq \sum_{j=1}^M \tilde{\varepsilon}_r(\boldsymbol{\chi}_{red}^j) \Gamma_i(\boldsymbol{\chi}_{red}^j) w_j, \quad (6.6)$$

where the values of  $w_j$  and  $\boldsymbol{\chi}_{red}^j$  are given by the corresponding multivariate quadrature rule.

For this type of integration scheme the number of required simulations,  $M$  is given by the number of dimensions of the random space,  $M \sim 2^k n^k / k!$  for large  $n$ , where  $k$  is known as the accuracy level of the Smolyak algorithm [13]. Again, by using PCA the number of simulations has been reduced and the model simplified.

For each iteration of our sparse grid algorithm, the EM simulator yields the scattering parameters of the structure. The (2,1)-th coefficient of the scattering matrix is used to extract the corresponding effective propagation

constant of a wave traveling through the line,

$$\beta(\boldsymbol{\chi}_{red}^j, \omega)L = \Im[\ln(S_{21}(\boldsymbol{\chi}_{red}^j, \omega))], \quad (6.7)$$

where  $\Im$  denotes the imaginary part.

The corresponding effective permittivity is computed by fitting the propagation constant to the expression

$$\beta^j(\omega) \simeq \left(\frac{\omega}{v_m}\right) \left(\frac{\tilde{\epsilon}_r(\boldsymbol{\chi}_{red}^j)}{\epsilon_{rm}}\right)^{0.5}, \quad (6.8)$$

where  $v_m$  and  $\epsilon_{rm}$  are the known propagation velocity and relative permittivity in the unperturbed line. Once the  $M$  samples of  $\tilde{\epsilon}_r(\boldsymbol{\chi}_{red})$  are collected, the coefficients (6.6) are evaluated and the model is complete.

### 6.3.4 Numerical Validation

Finally, the formulation is evaluated with a numerical example. The inner radius of the cable is  $d = 0.2$  cm and the outer radius,  $D = 0.5$  cm. The capacitance per unit length varies with the permittivity (6.1) according to expression (6.3), while the inductance is constant. The length of the line is 1 m, the correlation length, 0.25 m, mean permittivity,  $\epsilon_{rm} = 4$  and  $\text{std}(\epsilon_{ri}) = 0.15$ . For a maximum frequency of 4 GHz, corresponding to  $\lambda = 37.5$  mm,  $dl = 2.5$  mm is used which results in  $N = 400$  segments. After the application of PCA, a four-dimensional vector of independent Gaussian random variables with zero mean and variances  $\text{Std} = [12.63, 10.79, 8.34, 5.85]$  is obtained. The effective permittivity is expanded in terms of five Hermite polynomials of the reduced-space variables  $\boldsymbol{\chi}_{red}$ ,

$$\tilde{\epsilon}_r = \alpha_o + \alpha_1\chi_{red,1} + \alpha_2\chi_{red,2} + \alpha_3\chi_{red,3} + \alpha_4\chi_{red,4}, \quad (6.9)$$

with constants  $\alpha_o = 3.98$ ,  $\alpha_1 = 0.090$ ,  $\alpha_2 = 0.00$ ,  $\alpha_3 = 0.0156$ ,  $\alpha_4 = 0.00$ . There is no contribution from components 2 and 4. In fact, as Fig. 6.4 shows, the average along the z-direction of such components is 4, meaning that the cumulative effects of components  $\chi_{red,2}$  and  $\chi_{red,4}$  are zero. This suggests that the permittivity can alternatively be estimated with the mean value of the randomly generated profile of the line; therefore, avoiding the electromagnetic

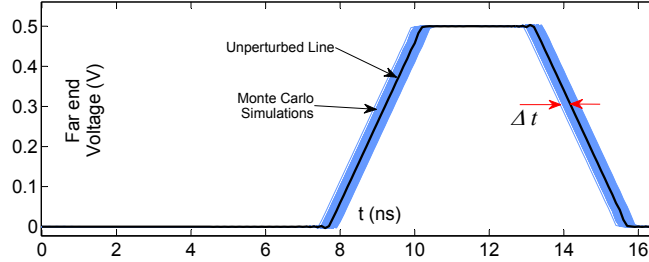


Figure 6.5: Far-end voltage samples for a number of Monte Carlo realizations of a lossless coaxial cable. The distortion in the line is manifested in terms of a random deviation of the time delay,  $\Delta t$ .

simulation. By using the mean of the permittivity of the segments of the line to estimate the effective permittivity for a specific realization of the profile instead of the electromagnetic simulation (6.7), the coefficients of model (6.9) are  $\alpha_0 = 4$ ,  $\alpha_1 = 0.091$ ,  $\alpha_2 = 0.00$ ,  $\alpha_3 = 0.0159$ ,  $\alpha_4 = 0.00$ . Therefore, the mean-based approach provides an accurate and significantly more expeditious way to calculate the effective permittivity.

The impact of the variability in the permittivity of the line is quantified in terms of perturbation in the expected propagation time as observed in Fig. 6.5, where a number of Monte Carlo simulations of the far-end time-domain voltage are pictured for coaxial cables with random permittivity profiles. For each of those iterations, an FEM simulation is performed to obtain the scattering parameters of the entire line with a randomly generated profile which are used to find the time-domain responses for a given load conditions and source. The cable is driven by a voltage source generating a rectangular pulse of amplitude 1 V and turn-on delay time of 1 ns, rise and fall times of 2.5 ns, and width of 3 ns. The source impedance is  $50 \Omega$  and the termination impedance is also  $50 \Omega$ .

The results obtained with the Monte Carlo simulation are used as a reference to validate the model. By employing the homogeneous model, the time deviation is computed as follows:

$$\Delta t(\mathbf{x}_{red}) = \frac{L}{v_m} \left[ 1 - \left( \frac{\tilde{\epsilon}_r(\mathbf{x}_{red})}{\epsilon_{rm}} \right)^{0.5} \right]. \quad (6.10)$$

The probability density function of  $\Delta t$  as a result of the Monte Carlo simulation is compared with the corresponding density obtained with the homogeneous stochastic model and the curves are shown in Fig. 6.6. Very good

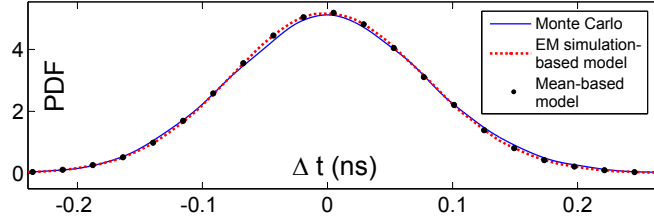
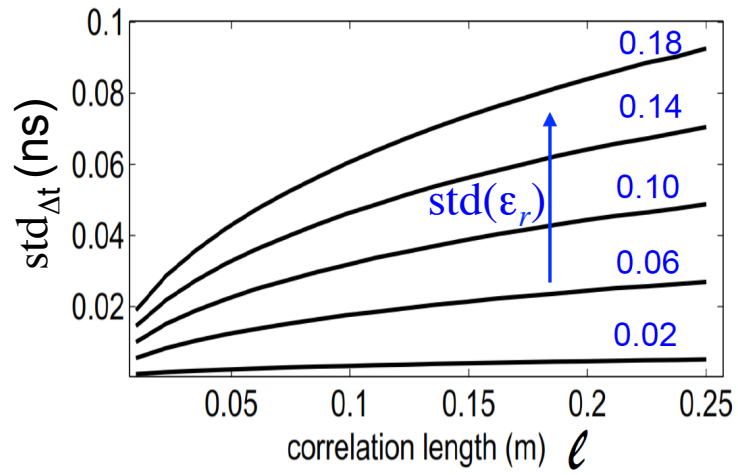


Figure 6.6: Probability density function of the deviation of the time delay induced due to the variability in the permittivity of the line. The methodology based on stochastic collocation is compared with Monte Carlo simulation.

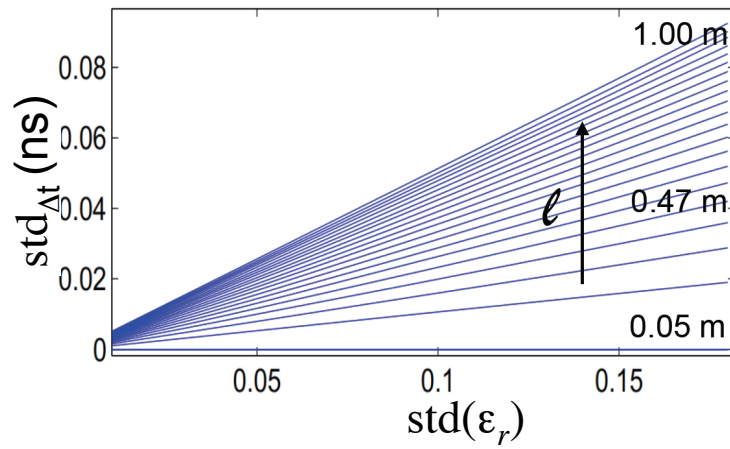
agreement is observed. The advantage of employing the proposed methodology is clear if we consider the computational savings. For the traditional Monte Carlo method, 10,000 FEM simulations were employed to construct the corresponding PDF which took 6.05 hours to implement in a MATLAB<sup>®</sup> code running on a 1.80 GHz Xeon CPU Windows machine, while only 33 simulations corresponding to 2.74 minutes were needed to construct the polynomial chaos interpolation of the effective relative permittivity constant with Smolyak accuracy level of 3 for the electromagnetic-based model. On the other hand, by using the mean-based approach, the time is cut down to  $6 \times 10^{-3}$  seconds.

Figure 6.7 represents the standard deviation of the induced jitter as a function of the variance of the permittivity and the correlation length of the profile. It is expected that the deviation increases as the magnitude of the perturbation of the permittivity increases as Fig. 6.7-(b) demonstrates. The first depicted plot of Fig. 6.7 shows how the standard deviation increases as the correlation length increases which can be explained as follows. In the limit of no correlation (zero correlation length) the jitter is given by a sum of many independent zero-mean random variables and according to the central limit theorem, it tends to zero. On the other hand, when the correlation length is much larger than the length of the line, the random variables behave as one so that the cumulative effect in the jitter is not cancelled by multiple contributions.

In this example the permittivity has been assumed to vary throughout the line. In the next case, the geometry is assumed to vary, specifically the routing of interconnects. The next example is meant for early design stages of PCB boards when a complete information of the routing is available.



(a)



(b)

Figure 6.7: Standard deviation of the jitter as a function of (a) correlation length and (b) variance of the permittivity.

## 6.4 Case Study 2: Interconnect Routing Variability

Transmission properties of high-speed interconnect channels are perturbed by the electromagnetic attributes of the adjacent environment. It is for this reason that, in analyzing the attributes of a channel, additional wiring present in the immediate vicinity of the channel conductors are also included in the electromagnetic model. However, early in the design stage routing information about the neighboring wiring distribution may not be available to inform the specifics of the electromagnetic properties of the environment in which the specific channel will be used. This absence of specificity may be thought of as an uncertainty that could be accounted for in the model in terms of a set of appropriately defined random variables. Predicting the transmission attributes of the channel in the presence of such routing variability, and thus assessing its impact on signal distortion, is the second example of this chapter.

While a variety of Monte Carlo based approaches have been proposed for the solution of the problem subject to specific driving and termination conditions in the presence of uncertainty in the values of per-unit length matrices  $\mathbf{L}$ ,  $\mathbf{R}$ ,  $\mathbf{C}$ ,  $\mathbf{G}$  (see, for example, [40]), these methods tend to be computationally expensive. Thus, and given the fact that, in early design stages rough estimates of the signal degradation due to such routing uncertainty may suffice for the development of guidelines for noise-aware floor-planning and routing, it is the objective of this example to present a computationally more efficient alternative to the aforementioned methods.

More specifically, the proposed approach combines the framework of parametric macromodeling with guaranteed passivity of [50, 49] with the ideas presented in [82, 81] and [114], to develop an expedient manner in which the impact of interconnect routing uncertainty on signal distortion can be computed.

Figure 6.8 presents the design flow of a PCB board where the fast assessment of the random routing is introduced in the early design stage in order to provide with predictive guidelines for the specification of rules that optimize the design.

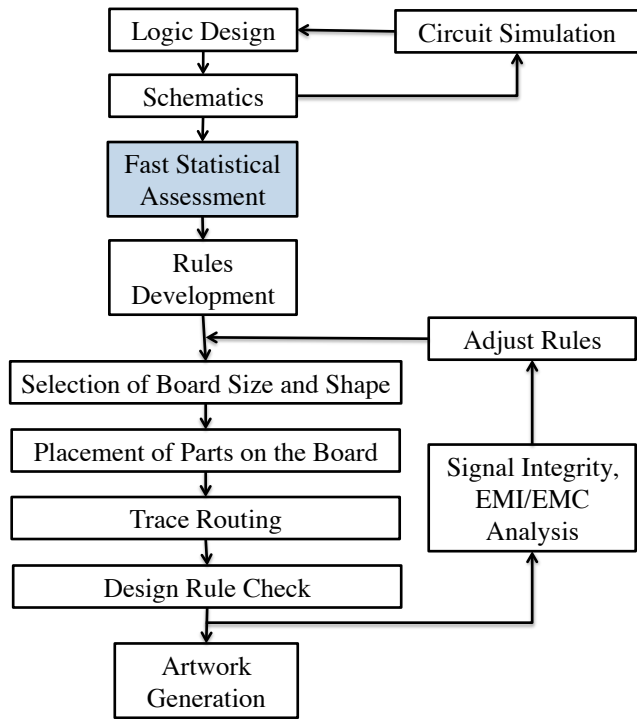


Figure 6.8: Proposed design flow of PCB boards in [2]. Our methodology intends to predict the behavior of the board to provide guiding in the design rules of the board.

### 6.4.1 Statistical Characterization

To fix ideas and without loss of generality, the case of two coupled microstrip lines will be used to describe the way routing uncertainty is described in the model. Figure 6.9 presents a realization of the random structure under consideration, where, in the absence of routing uncertainty, the two signal traces run parallel to each other at a fixed separation distance,  $s$ , as depicted in the cross-sectional view of Fig. 6.10. Routing variability along the length of the interconnect can be described by the random displacement along the  $x$ -axis of the two end points of the bottom signal trace relative to the top trace. Recognizing that the channel formed by the two coupled interconnects may be considered as the concatenation of  $N$  such sections, the random variables assigned the  $x$ -axis relative displacement of the end points of the bottom wire in each section with respect to the top wire in the same section define the random space in which routing uncertainty is defined. There are two approaches that can be considered as shown in Fig. 6.9, depending on the way the overall line is sectioned into smaller pieces. Particularly, the formulation presented focuses on the Approach A due to its simplicity. Clearly, the physical continuity of the channel requires that the same random variable is used to describe the displacement of the connection point of two consecutive sections. Thus, for the two-conductor channel case considered, assuming fixed conductor pitch at the end points of the channel and  $N$  sections, each of the same fixed length,  $\ell$ , used to segment the channel, routing uncertainty requires the introduction of  $N - 1$  random variables,  $\chi_n$ ,  $n = 1, 2, \dots, N - 1$ .

### 6.4.2 Electromagnetic Modeling in the Presence of Routing Uncertainty

With the input uncertainty parameterized in terms of these  $N - 1$  random variables and their associated probability density functions (PDF), a standard Monte Carlo process would consist of the calculation of the broadband electromagnetic response of the channel for a sufficiently large number of model realizations in the  $N - 1$  random space to ensure convergence. For each one of the realizations, a broadband transfer function matrix (e.g., a scattering-parameter matrix) of the interconnect multi-port will be gener-

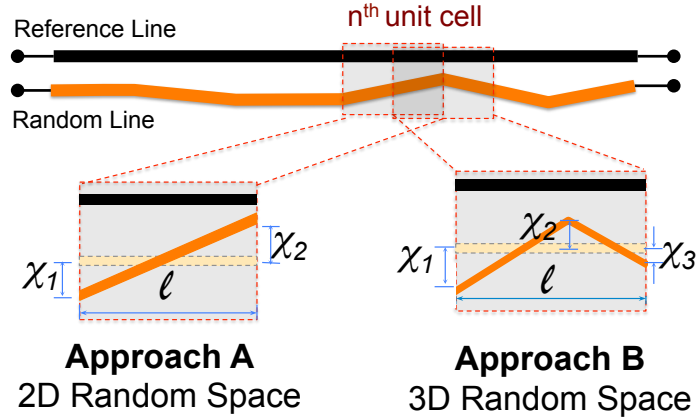


Figure 6.9: Longitudinal view of a section of a planar interconnect structure consisting of two signal traces. Uncertainty in routing is defined in terms of the displacement of the  $x$  coordinate of each of the two end points of the bottom wire.

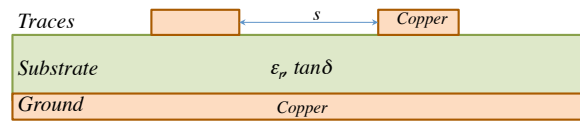


Figure 6.10: Cross section of a coupled microstrip line.

ated. Even with a possible reduction of the computational complexity of the Monte Carlo analysis through the use of sparse sampling of the random space (e.g., [13]), the overall computational complexity is still high because of the cost involved in the broadband electromagnetic analysis of the entire channel. Thus, and given the fact that our interest is in a quantitative assessment of the impact of routing variability on signal degradation early in the design phase when layout specificity is still lacking, it is computational efficiency rather than solution accuracy that should be emphasized in the development of the modeling methodology and the solution algorithm. Such a methodology is described next.

An intuitively more efficient alternative to the Monte Carlo methodology described above is one that substitutes the electromagnetic response of the entire structure with that of the *unit cell* of the structure, understood to be the section depicted in Fig. 6.10. Toward this, it will be assumed that impact on signal degradation due to possible geometric discontinuities at the junction between adjacent sections is of secondary importance to that contributed by the distributed geometric non-uniformity due to routing variability along the

entire channel length. Thus, with the electromagnetic transfer function for each section computed and cast in terms of a transmission matrix that relates the output voltages and currents to the input voltages and currents [115],

$$\begin{bmatrix} \mathbf{v}_{out}^n \\ \mathbf{i}_{out}^n \end{bmatrix} = \mathbf{T}_n(\chi_{n-1}, \chi_n) \begin{bmatrix} \mathbf{v}_{in}^n \\ \mathbf{i}_{in}^n \end{bmatrix}, \quad (6.11)$$

the overall transmission matrix is simply obtained as the multiplication of the  $N$  transmission matrices,  $\mathbf{T}_n$ , for  $n = 1, 2, \dots, N$ ,

$$\mathbf{T}_T = \mathbf{T}_N(0, \chi_{N-1})\mathbf{T}_{N-1}(\chi_{N-1}, \chi_{N-2}) \dots \mathbf{T}_1(\chi_1, 0). \quad (6.12)$$

At this point it is important to stress that the matrices  $\mathbf{T}_n(\chi_n, \chi_{n-1})$  are readily obtained from the more standard matrices (e.g., scattering matrix, impedance matrix or admittance matrix) used for the definition of electromagnetic transfer functions of multi-ports. Once  $\mathbf{T}_T$  has been obtained, its conversion to the scattering matrix,  $\mathbf{S}_T$ , for the overall channel is straightforward. The broadband scattering parameters are, in turn, used to perform time-domain simulations for a given set of source and termination conditions in an expedient way as described in [116]. Each such simulation corresponds to one realization of the overall channel in the  $(N - 1)$ -dimensional random space. Compared to the approach described earlier, any computational savings in this alternative approach appears to be associated with the fact that we have decomposed the numerical electromagnetic analysis of the overall channel to the numerical solution of each of the  $N$  sections, which, in addition to being faster because of the smaller number of degrees of freedom in each section, could also be run in parallel. However, the major gains of such an approach are associated with the fact that we can limit the numerical electromagnetic analysis to only a single section (what we defined earlier as the *unit cell* of the structure) computed for only a set of points on a two-dimensional domain in the random space with boundaries dictated by the extreme values of the channel routing uncertainty. The way this is done is discussed in the next section.

### 6.4.3 Parametric Electromagnetic Macromodeling of the Unit Cell

It is evident from the discussion above that the routing uncertainty in the unit cell of the specific two-conductor channel under consideration is defined in terms of two random variables. The only difference from one section to the next will be the end points of the domains over which each random value is defined and, possibly, the associated pdf. Let  $\chi_{min}$  and  $\chi_{max}$  denote, respectively, the smallest and the largest values of the random perturbations of all random variables involved in the definition of the routing uncertainty. Then the unit square in the two-dimensional random space  $(\chi_1, \chi_2)$  of side  $\chi_{max} - \chi_{min}$  includes all possible values of the random perturbations that define the routing uncertainty in the channel. This, then suggests the use of a parametric macromodel over the two-dimensional random space  $(\chi_1, \chi_2)$  for the scattering matrix of the unit cell as a means for the fast generation of the scattering matrix (and, thus, the transmission matrix) for each unit cell. The way this can be done for the case of the scattering matrix and in a manner that the generated macromodel is passive has been described in [50] and is briefly summarized in the following.

Consider a grid of  $K$  points over the two-dimensional random space  $(\chi_1, \chi_2)$ . More specifically, a Cartesian grid of points is considered, through the definition of properly selected grid points along each one of the two axes. For the specific case of the square random space  $(\chi_1, \chi_2)$  used for our purposes, the same assignment of  $L$  grid points is made along the two axes  $\chi_1$  and  $\chi_2$ ; hence,  $K = L^2$ . Let  $\chi_1^{(1)}, \chi_1^{(2)}, \dots, \chi_1^{(L)}$  denote the grid points along the  $\chi_1$  axis in the domain and  $\chi_2^{(1)}, \chi_2^{(2)}, \dots, \chi_2^{(L)}$  denote the grid points along the  $\chi_2$  axis. For each point  $(\chi_1^{(k_1)}, \chi_2^{(k_2)})$ ,  $k_1, k_2 = 1, 2, \dots, L$ , an electromagnetic field solver is used to calculate the scattering matrix,  $\mathbf{S}(s_m, (\chi_1^{(k_1)}, \chi_2^{(k_2)}))$ ,  $m = 1, 2, \dots, M$ , at a set of  $M$  frequency points over a predetermined frequency range, where  $s = j\omega$  denotes the complex frequency. Subsequently, making use of the vector fitting technique [117] a stable and passive rational macromodel is generated for each one of the  $K$  realizations of the *unit cell* section [46].

These  $K$  macromodels share the same poles and serve as the *root macromodels* used for the subsequent development of a global parametric macromodel of the *unit cell*, as described in [50]. More specifically, a tensor product

bivariate interpolation is used on the square grid with node points the points at which the root macromodels are generated. The resulting interpolant is of the form

$$\mathbf{S}(s, \chi_1, \chi_2) = \sum_{k_1=1}^L \sum_{k_2=1}^L \mathbf{S}(s, \chi_1^{(k_1)}, \chi_2^{(k_2)}) \times w_{k_1}(\chi_1) w_{k_2}(\chi_2), \quad (6.13)$$

where the interpolation functions  $w_{k_i}(\chi_i)$ ,  $i = 1, 2$ , are chosen to be the linear interpolation functions of the form

$$\begin{aligned} & \frac{\chi_{(i)} - \chi_{(i)}^{(k_i-1)}}{\chi_{(i)}^{(k_i)} - \chi_{(i)}^{(k_i-1)}}, \chi_{(i)} \in [\chi_{(i)}^{(k_i-1)}, \chi_{(i)}^{(k_i)}], k_i = 2, \dots, L \\ & \frac{\chi_{(i)}^{(k_i+1)} - \chi_{(i)}}{\chi_{(i)}^{(k_i+1)} - \chi_{(i)}^{(k_i)}}, \chi_{(i)} \in [\chi_{(i)}^{(k_i)}, \chi_{(i)}^{(k_i+1)}], k_i = 1, \dots, L - 1 \\ & 0, \text{ otherwise.} \end{aligned} \quad (6.14)$$

Since these interpolation functions satisfy the constraints

$$\begin{aligned} & w_m(\chi_i) \geq 0, m = 1, 2, \dots, L \\ & w_m(\chi_i = \chi_i^{(n)}) = \delta_{m,n}, m, n = 1, 2, \dots, L \\ & \sum_{m=1}^L w_m(\chi_i) = 1, \end{aligned} \quad (6.15)$$

where  $i = 1, 2$ , the global parametric macromodel of (6.13) is stable and passive [50].

The availability of such a stable, passive, global parametric macromodel allows the fast calculation of the scattering parameters of the *unit cell* of the channel for any values of the routing uncertainty induced perturbation of the  $x$  coordinates of the end points of conductor 2 relative to conductor 1. Since the two-dimensional random domain over which the global macromodel is valid is defined by the extreme values of the relative perturbation along the entire length of the channel, the same macromodel is used to calculate the scattering matrix for each one of the  $N$  sections in which the channel has been segmented for a given realization of the channel on the  $(N - 1)$ -dimensional random space defined by the perturbations of the  $N - 1$  end points. All that is required is the definition of the probability density functions for the random variables associated with each interior point in the segmentation of the channel.

Thus, given the total length of the coupled microstrip interconnect chan-

nel, the geometric attributes of the unperturbed cross-sectional geometry, the electromagnetic properties of the conductors and the insulating dielectrics, and the range of possible relative displacement of one of the conductors with respect to the other, the process described above is used to calculate a global, parametric scattering-parameter macromodel for a section of the channel of length  $\ell$  dictated by the total length of the channel and the number of points  $N$  chosen to introduce either changes in routing direction or changes in the pitch between conductors. The frequency range of validity of the global parametric macromodel is chosen such that it can support the bandwidth of the transient simulations of interest to the analysis. With the global macromodel available a computationally efficient Monte Carlo analysis becomes possible for the prediction of channel routing uncertainty induced signal degradation. Irrespective of the way we sample the  $(N - 1)$ -dimensional random space defined by the random variables associated with the  $N - 1$  interior points used for the segmentation of the channel, the efficiency of the Monte Carlo analysis is provided by the fact that the calculation of the channel transmission matrix – and, thus, the channel scattering matrix – using (6.12) involves the simple matrix multiplications of the transmission matrices for each section, obtained from the *unit cell* global parametric macromodel for the specific values of the perturbations of the end points of each section in each realization.

#### 6.4.4 Numerical Results

To demonstrate the proposed methodology, the case of a coupled microstrip interconnect of total length of 30 cm is considered. The unperturbed cross-sectional geometry of the structure is depicted in Fig. 6.10. The strips are rectangular of width 3 mm and thickness 0.05 mm. The distance  $s$  between them is 7 mm. The substrate of thickness 1.6 mm has relative permittivity of 4.5 and loss tangent of 0.02. The thickness of the ground plane is 0.2 mm. All conductors are copper of conductivity  $5.8 \times 10^7$  S/m. The channel is segmented into 10 sections, each of length 30 mm. Referring to Fig. 6.9, the maximum perturbation from its original value in the spacing between the two traces is  $\pm 6$  mm. Thus, the global parametric macromodel for the *unit cell* of length 30 mm is defined over the square domain in the  $\chi_1, \chi_2$  random space.

A  $5 \times 5$  uniform grid of side length of 12 mm and centered at the origin is used to generate the 25 root macromodels used for the interpolation. Consecutive grid nodes are spaced 0.25 mm. For each grid node, the transmission matrices for the *unit cell* were computed using ANSYS<sup>®</sup> Q3D Extractor<sup>®</sup> [100] at 30 linearly spaced frequency points in the frequency range [0.001, 5] GHz.

With these models a Monte Carlo simulation is performed to calculate the statistics of the transient response of the channel under the following excitation and termination conditions. The top trace is driven by voltage source generating a rectangular pulse of amplitude 1 V and turn-on delay time of 1 ns, rise and fall times of 0.5 ns, and width of 1 ns. The input resistance of the source is  $50 \Omega$ . The resistive termination of the ports is also  $50 \Omega$ .

With regard to the definition of the routing uncertainty, any PDF describing a random variable in the range [-6,6] mm can be utilized for the end points of the segment. For the purposes of this study, we assume a discrete PDF of random variable  $\chi$  given by

$$p(\chi) = \begin{cases} \frac{1}{5}, & \chi = 6, -6 \\ \frac{1}{5}, & \chi = 3, -3 \\ \frac{1}{5}, & \chi = 0 \end{cases} . \quad (6.16)$$

The total number of Monte Carlo iterations was 5000. The near- and far-end voltages are computed for each realization. The variability may be quantified in terms of the mean and the standard deviation (std) of the response, as depicted in Fig. 6.11. Plotted in the figures are the near-end and far-end mean voltage responses for the top line, along with the  $\pm$ std deviations for each one. This is done for Approaches A and B from Fig. 6.9. The response variability due to routing uncertainty both in amplitude and delay is evident. Figure 6.12 presents the PDF of the far-end voltage evaluated at the middle point of the pulse width and it is shown that the second approach results in a larger degradation as a consequence of the bend that is captured in the model.

In summary, a methodology has been proposed for the expedient analysis of the impact of routing uncertainty on the transmission attributes of high-speed, coupled interconnects. Aimed for use in early stages in the design phase where floor planning and layout specificity is still lacking, the proposed methodology achieves its efficiency by combining the ideas of passive multi-

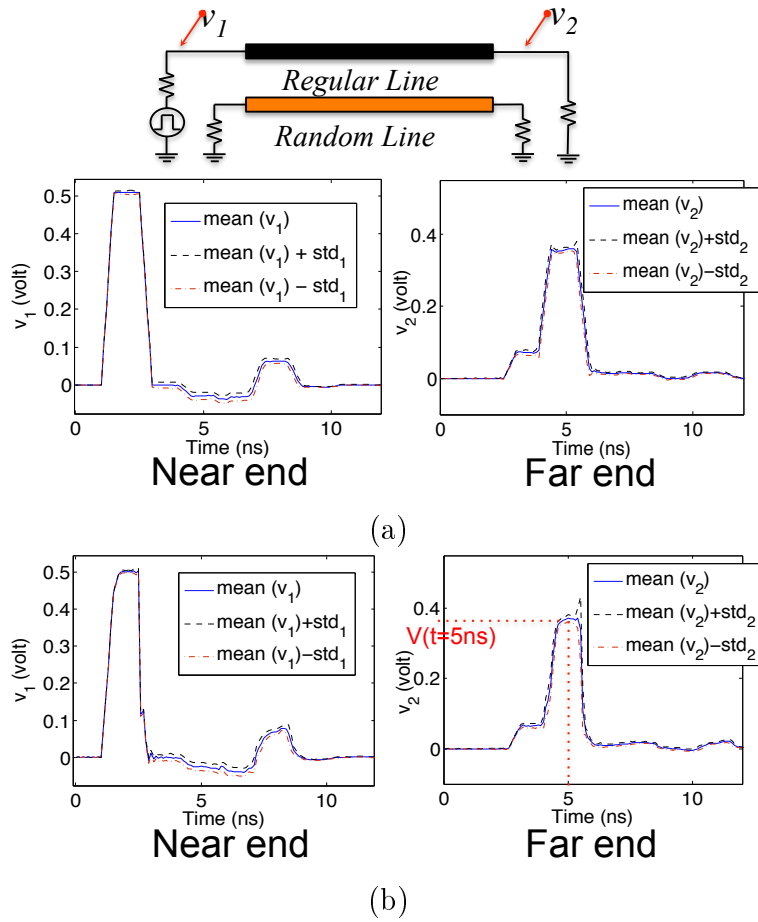


Figure 6.11: Calculated mean value and standard deviation for the near-end and far-end voltages of the unperturbed line using Approach A (top) and Approach B (bottom).

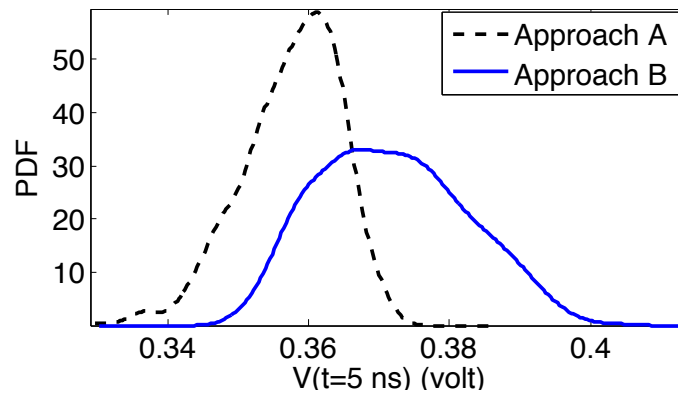


Figure 6.12: Probability density of the far-end voltage at the middle point of the pulse width.

variate parametric macromodeling with a representation of the interconnect channel in terms of a concatenation of several sections with conductor spacing at their end points controlled by the routing uncertainty.

While the proposed methodology was presented, for simplicity, for the case of two coupled wires in a microstrip configuration, its extension to the more general case of a multi-conductor system is straightforward. The only difference is that the number of random variables used for the description of the routing uncertainty in the random cell will increase with the number of coupled wires. In addition, even though the section of the unit cell was assumed fixed for the purposes of this chapter, its value may also be allowed to be random, thus allowing for uncertainty in the length of the channel to be included in the analysis.

## Chapter 7

# MODELING OF DISORDERED PERIODIC WAVEGUIDES

### 7.1 Introduction

The last stochastic modeling application concerns the problem of a periodic waveguides exhibiting statistical variability. Following the assumptions taken in Chapter 6, localized uncertainty is considered. In other words, we assume that the periodic structure exhibits statistical disorder manifested in variability of the geometric and material parameters from one cell to the next.

Periodic waveguides are commonly used for a variety of filtering and other types of electromagnetic signal processing applications [115]. Although these structures are intended to be ideally periodic, manufacturing-induced variability results in random alterations of the geometry and material properties of the structure as it is shown in Fig. 7.1. These, in turn, result in degradation of the intended transmission attributes of the electromagnetic structure. While Monte Carlo methods are the natural candidates for the quantitative assessment of the impact of such statistical variability on the electromagnetic attributes of the structure, their slow convergence is an issue of concern when the computational cost of obtaining the response for each realization of the structure is high. Given the structures of interest, this is the case for our purposes, especially when three-dimensional full-wave electromagnetic solvers are used. Thus, an alternative, more efficient approach is desirable. Such an approach is considered and evaluated in this chapter.

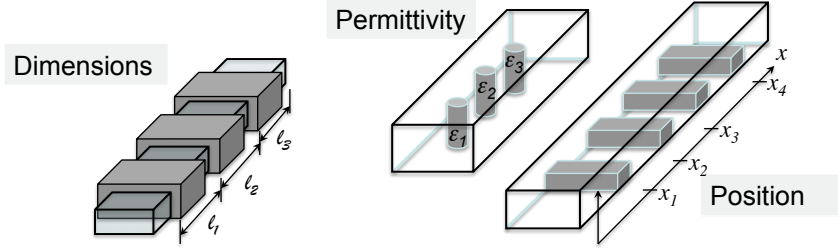


Figure 7.1: Examples of disorder in periodic waveguides.

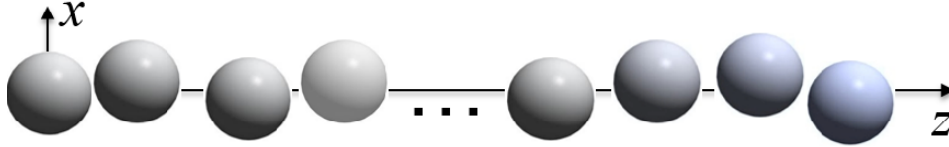


Figure 7.2: Disordered array of silver nanoparticles.

### 7.1.1 Motivation: Disordered Array of Nanospheres

Arrays of nanoparticles are employed in the design of metamaterial structures, nanocircuits, nanoantennas, among others. Most commonly, the modeling of such devices is usually done assuming a perfect periodicity of the array. In reality, however, the manufacturing process yields a disordered pattern of particles due to variability in particle size, placement, and electrical properties as depicted in Fig. 7.2. In view of this, a spherical nanoarray provides an interesting candidate to study the impact of such disorder on the electromagnetic behavior of waveguides composed by such arrays of nanospheres. The investigation of the impact of disorder has been presented in the literature for the case of a periodic chain of nanoparticles using a simple dipole model approximation [118, 78]. Here, a rigorous full-wave solver, Wave3D [119] is used to characterize the impact of such disorder.

The silver spheres in ideal state have radius 10 nm and center-to-center separation of 22 nm. The disorder is assumed to be quantified in terms of a set of independent random variables. For each parameter variation, for example, permittivity or position, there are  $N$  random variables where  $N$  is the number of spheres in the array. Particularly, Gaussian random variables with zero mean and variance 0.5 nm are assumed to define the perturbation in the positions of the spheres along  $z$ - and  $x$ -axes. The operation frequency is 780 THz and the corresponding relative permittivity,  $\epsilon_r = -4.56 - j0.22$ .

Stochastic collocation has been employed to calculate the mean and stan-

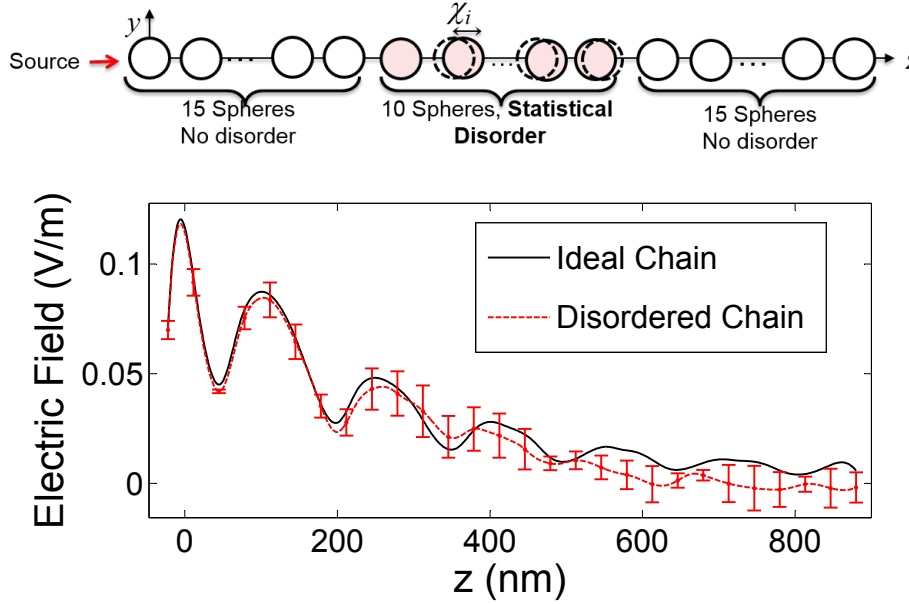


Figure 7.3: Statistical disorder induced in the longitudinal position of the 10 middle spheres (up). Electric field sampled at  $(20 \text{ nm}, 0, z)$ . Error bars have a height of two  $\text{std}(|E|)$  (down).

standard deviation of the electric field for the disordered array of silver nanospheres from Fig. 7.2. Given the high dimensionality associated with this problem only the 10 middle spheres have perturbation in their positions while the 15 first and last spheres are left unperturbed. Two types of perturbations have been introduced, along the axis of the array (*longitudinal*) and perpendicularly to the axis (*transverse*). Figure 7.3 shows the geometry with longitudinal perturbations and the corresponding moments of the fields sampled at a line 20 nm away from the  $z$ -axis while Fig. 7.4 shows the results for the transverse-perturbation case. It is clear that the impact of the longitudinal disorder is much larger than the transverse disorder case. Concerning the sparse grid, for a ten-dimensional random space and accuracy level of 3, 201 full-wave solver simulations were needed.

It is evident that as we increase the number of spheres, the number of random variables increases which means that the dimensionality of the problem and the number of simulations grow too. Additionally, the electrical size of the problem increases. This means that we require more simulations of more computationally expensive structures as the number of spheres increments.

Notice that in the analysis, the propagating modes can be extracted by

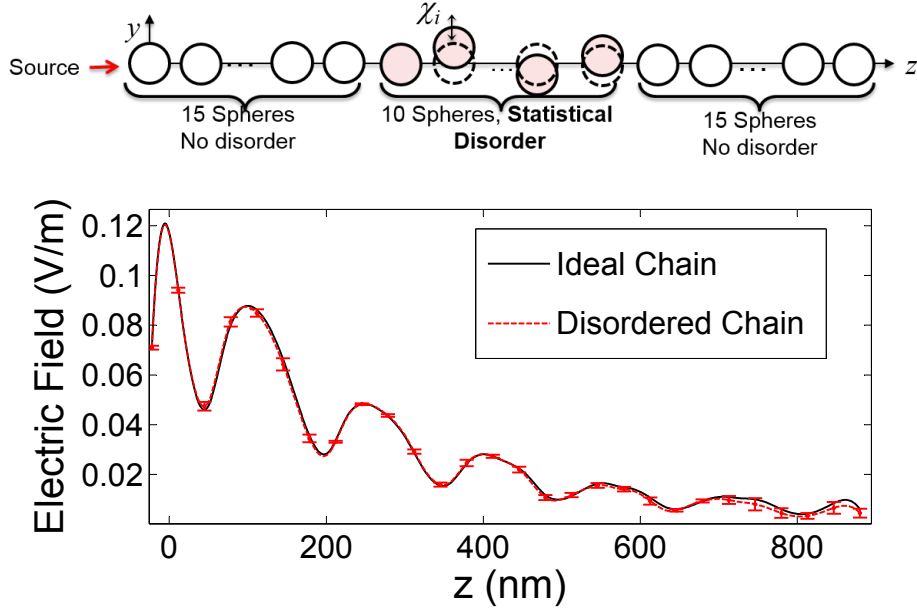


Figure 7.4: Statistical disorder induced in the transverse position of the 10 middle spheres (up). Electric field sampled at  $(20 \text{ nm}, 0, z)$ . Error bars have a height of two  $\text{std}(|E|)$  (down).

sampling the field of a large enough structure such that the reflections from the end of the line are negligible. Even though this is a valid approach and there are existing methods for the modes extraction using the complete structure [120], the more straightforward way to do so is by using Foucault's theory on one single unit cell. In view of this, it is necessary to search for an alternative approach that captures the uncertainty of the problem by focusing on one single unit cell. Such an approach has been investigated in the aerospace community for mechanical waves by Cai and Lin [82]. In this chapter, such methodology is put in the finite element method context to investigate electromagnetic waveguides with disorder.

The proposed approach makes use of the Anderson localization theory [79] for the computationally efficient calculation of an average exponential decay per unit cell for the transmitted wave, also known in the solid-state physics literature as *localization factor*. As already demonstrated through earlier applications of the Anderson localization theory to a variety of periodic dynamic systems (see, for example, [81], [121], and [82]), this average exponential decay has been shown to provide for an accurate quantitative measure of the disorder-induced degradation of the response attributes of

the periodic structure. In earlier studies, it has been demonstrated how this technique can be used to analyze the effects of statistical material/geometric disorder in the electromagnetic properties of transmission-line based meta-material structures, where lumped circuit elements and transmission-lines based structures suffice for their modeling [83]. The way this methodology can be generalized for the case of periodic structures for which a full-wave, vectorial electromagnetic field formulation is needed for their modeling, was presented in [122, 123].

### 7.1.2 Organization

The chapter is organized as follows. In Section 7.2, we consider the uncertainty in the geometric/material disorder of the periodic structure and describe the method we adopt for its description in terms of a probability density function given an appropriate set of experimentally obtained data. In Section 7.3, we make use of the finite element method (FEM) for the electromagnetic modeling of the structure and explain how the FEM model can be combined with the results in [82] to compute the localization factor for a disordered periodic structure. The accuracy of the proposed method, along with some of its key attributes, are examined in Section 7.4 through its application to the analysis of a periodic waveguide. The chapter concludes with a summary of the proposed methodology.

## 7.2 Quantification of Uncertainty in Input Parameters

To fix ideas, consider the case of the  $y$ -invariant, parallel-plate waveguide structure, of the longitudinal section as depicted in Fig. 7.5. Without loss of generality, we consider the case where all materials are lossless and the structure is operated at the fundamental, transverse electromagnetic (TEM) mode, with wave propagation along  $x$ . The intended periodic loading with  $y$ -directed conducting strips of rectangular cross section would result, under ideal conditions of perfect periodicity, in a band-stop filter structure. However, in the presence of uncertainty in the longitudinal positioning of each wire, such ideal behavior is degraded. For example, as depicted in the figure,

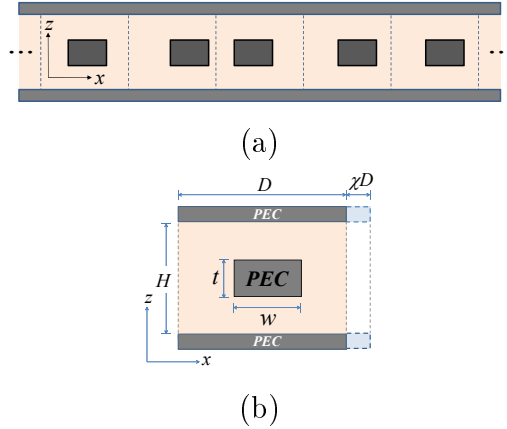


Figure 7.5: (a) Longitudinal cross section of a disordered periodic parallel-plate waveguide. (b) The disorder is caused by a random perturbation in the length of the unit cell.

an uncertainty in the length of the unit cell is readily described in terms of a single random variable,  $\chi$ .

To start with, we need to quantify the uncertainty in terms of the probability density functions (PDF) of the geometric parameters identified as the sources of the uncertainty. Once these PDFs are available, an electromagnetic model of the structure is required to propagate the input uncertainty to the electromagnetic response of the structure. The ultimate result is the quantitative prediction of the impact of input uncertainties on the transmission properties of the structure. A common practice is to assume that the input random parameters follow an arbitrary distribution, most often chosen to be either uniform or Gaussian. However, in several cases, the only information available for the characterization of input uncertainty is a set of data obtained either from the direct measurement of the manufactured devices or from information pertinent to the uncertainty introduced by the manufacturing process. This, then, calls for a systematic way for the estimation of the PDF for an input random variable from a limited set of data.

Without loss of generality, let us assume that input uncertainty is defined in terms of a finite number of independent random variables, and no correlation exists between random variables from one unit cell to the next.

### 7.3 Diffusion Model for Density Estimation

The solution of a stochastic problem requires the statistical characterization of the input random parameters in terms of their probability density functions as the first step of the process. Consider, for example a pair of high-speed links with random separation. Instead of assuming a particular nature for the statistics of the parameter like uniform or Gaussian, a set of measurements for different board structures with different trace separations are obtained and used to extract a probability density of the parameter.

Botev proposes a nonparametric density estimation process that has the attractive attribute that no assumption is made about the randomness of the input data. This method known as the nonparametric diffusion-mixing based estimator presented by Botev [124, 125] and previously employed in the stochastic analysis of micro-electromechanical structures in [126], [127] combines the traditional Kernel Density Estimation (KDE) process with the solution to a generalized diffusion equation for the unknown distribution with point sources associated with the available measured data. Utilizing position-dependent diffusivity and drift terms that are dependent on an estimate of the PDF, a position-dependent diffusion and drift are effected in the solution. More specifically, in regions where the estimated density is low and thus fewer observations are expected, a higher diffusion and drift provide for a smoothing of the initial data. In contrast, for those regions where higher values of the estimated density indicate a higher value of expected observations, the diffusion and drift are lower.

In the heart of this method is the idea that the PDF to be estimated can be computed as the solution of the generalized heat diffusion equation, given by

$$\frac{\partial}{\partial t} \hat{\rho}(\chi, t) = \frac{1}{2} \frac{\partial}{\partial \chi} \left( a(\chi) \frac{\partial}{\partial \chi} \left( \frac{\hat{\rho}(\chi, t)}{p(\chi)} \right) \right), \quad (7.1)$$

for  $\chi \in \mathcal{D}$ ,  $t > 0$ . In equation (7.1),  $a(\chi)$  is a positive function in  $\mathcal{D}$ , and  $p(\chi)$  is the probability density function describing any available prior information. The equation is solved in  $\mathcal{D}$  with boundary conditions  $\rho(L_1, t) = \rho(L_2, t) = 0$ . This restriction in fact allows us to model a density function according to the physical restriction of the problem. The meaning of these boundary conditions is obvious and physically satisfying: the estimated PDF is zero

at the boundaries of the domain, because the range of the allowed values of the parameter under consideration is finite. For example, in the context of the specific example of a periodic waveguide considered in this chapter. In particular, adjacent crossing loading wires in the waveguide are at a finite distance from each other and cannot coincide or superpose partially. Thus, the uncertainty in the distance between them is constrained to a certain range controlled by the intended attributes of the structure. Returning to the functions  $a(\chi)$  and  $p(\chi)$ , it is noted that they provide for smoothing of the density in regions where data is sparse and sharpening in regions of high concentrations of data [127]. Clearly, they have to be specified before the equation can be solved. As already mentioned above, in the absence of any a-priori information about the PDF, its initial value,  $\hat{\rho}_0(\chi)$ , is computed using standard KDE with a Gaussian kernel. Once obtained,  $\hat{\rho}_0(\chi)$  is used for the calculation of  $a(\chi)$  and  $p(\chi)$  through the equations  $a(\chi) = \hat{\rho}_0(\chi)$  and  $p(\chi) = \hat{\rho}_0^\nu(\chi)$ ,  $\nu \in [0, 1]$ . As it has been shown in [126], these choices with a relatively low value of  $\nu$  minimize the mean integrated square error of the estimated distribution. For our purposes a value of  $\nu = 0.1$  is employed.

Concerning the numerical solution of (7.1), a finite difference time domain (FDTD) formulation is used with initial condition taken to be a combination of Dirac delta functions placed at the samples,

$$\rho(\chi, 0) = \frac{1}{M} \sum_{i=1}^M \delta(\chi - \chi_i). \quad (7.2)$$

Similarly to KDE, the optimum value of the simulation time in the solution of (7.1) is chosen such that it maximizes the MLCV score,

$$MLCV(t) = \frac{1}{M} \sum_{i=1}^M \log \rho_{-i}(\chi_i, t), \quad (7.3)$$

where  $\rho_{-i}(\chi, t)$  is the solution of equation (7.1) with the initial condition

$$\rho_{-i}(\chi, 0) = \frac{1}{M-1} \sum_{j=1, j \neq i}^M \delta(\chi - \chi_j), \quad (7.4)$$

which excludes the  $i$ -th sample [128].

Due to these attributes, the diffusion-mixing based estimator has been shown to provide improved accuracy over KDE in the PDF estimate for any

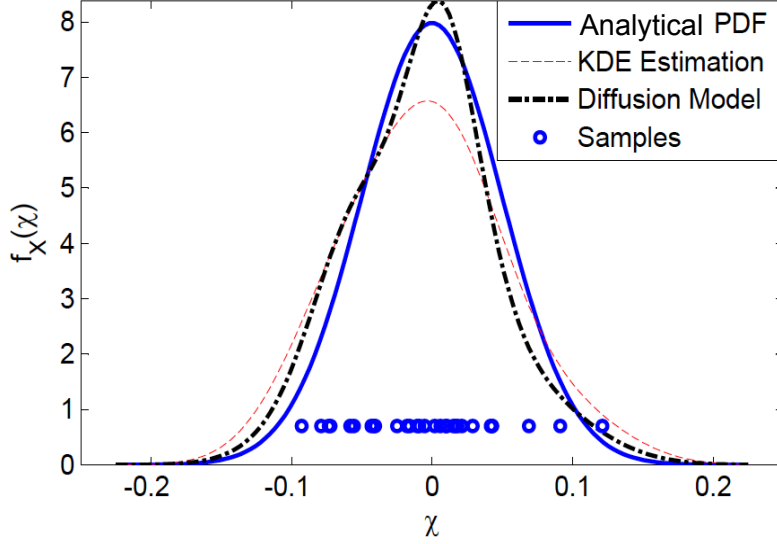


Figure 7.6: Estimated PDF obtained using a diffusion-mixing based estimator and KDE using as input 30 randomly chosen samples that follow a Gaussian distribution.

point in the interval spanned by the input data. This improved accuracy is demonstrated in Fig. 7.6, which compares the estimated PDF using standard KDE and the diffusion-mixing based estimator using as input a set of 30 randomly chosen samples that follow a Gaussian random variable with zero mean and standard deviation 0.05. The attributes of the diffusion-mixing based estimator are evident. In particular, the method captures the behavior of the random variable with higher accuracy in the peaks and valleys of the distribution. A summary of the key steps for the development of an algorithm for the diffusion-mixing based estimator is provided in [126], [127].

## 7.4 Electromagnetic Model for Uncertainty Propagation

Next, we turn our attention to the development of a model for the propagation of the input data uncertainty to the electromagnetic response of the periodic structure. With the structure depicted in Fig. 7.5 as our reference structure, and under the stated assumption that the structure is operated at the fundamental, transverse electromagnetic (TEM) mode with wave propagation along  $x$ , the transmission properties of the structure are quantified

in terms of the propagation constant of the TEM wave. In the case of an ideal structure that exhibits no disorder in its periodicity, the propagation constant can be computed through the application of Floquet analysis [115].

In such an analysis, the electromagnetic model involves the region associated with the unit cell of the periodic structure. Over this region, an approximation of Maxwell's equations in the absence of sources is used to develop the numerical model used for the analysis of the electromagnetic properties of the periodic structure. For our purposes, the finite element method is used for the approximation of Maxwell's equations. In particular, the Floquet-based finite element model in [85] is adopted. Through a standard Galerkin process, the finite element approximation of the vector Helmholtz equation for the electric field over the unit cell of the periodic waveguide results in a linear system of the form,

$$[M_{o1}] \mathbf{x}^r = [M_{o2}] \mathbf{x}^l, \quad (7.5)$$

where  $[M_{o1}], [M_{o2}] \in \mathbb{C}^{M \times M}$ , and the entries of vectors  $\mathbf{x}^r, \mathbf{x}^l \in \mathbb{C}^{M \times 1}$  are the weights of the expansion functions used to approximate the electric and magnetic fields on the left and right boundaries of the unit cell, respectively, which are perpendicular to the direction of wave propagation. Imposing the Floquet periodic boundary condition,  $\mathbf{x}^r = e^{-\gamma_0 D} \mathbf{x}^l$ , on these boundaries, with  $D$  denoting the distance between the two boundaries for the case of the unperturbed unit cell, results in the linear eigenvalue problem

$$e^{-\gamma_0 D} [M_{o1}] \mathbf{x}^l = [M_{o2}] \mathbf{x}^l. \quad (7.6)$$

The solution to (7.6) yields a set of  $M$  eigenvalues and their respective eigenvectors. With the bandwidth of interest of the electromagnetic analysis limited to TEM mode propagation only, the eigenmodes of interest are the ones for the TEM left-propagating and right-propagating waves. Their eigenvectors are sorted in the matrix  $[V_o] \in \mathbb{C}^{M \times 2}$ .

Consider, next, a small disorder in the position of the wire in the  $n$ -th cell, described in terms of a statistical variability in the length of the cell as follows,

$$D_n = D (1 + \chi_n). \quad (7.7)$$

The random variable  $\chi_n$  is assumed to follow a given probability distribution,  $\rho(\chi)$ , with zero mean and standard deviation denoted std. Furthermore, it is assumed that variables  $\chi_n$ , one for each cell that exhibits disorder, are independent and identically distributed. In a manner similar to the case of the ideal unit cell, the finite element model describing propagation through the  $n$ -th cell is of the form

$$[M_{n1}] [V_o] \mathbf{y}^r = [M_{n2}] [V_o] \mathbf{y}^l. \quad (7.8)$$

In the above equation, use was made of the fact that the vectors  $\mathbf{x}^{l,r}$  at the left and right ends of the  $n$ -th cell can be expressed in terms of the eigenvectors of the fundamental eigenmodes  $\mathbf{x}^{l,r} = [V_o] \mathbf{y}^{l,r}$ , where  $\mathbf{y} \in \mathbb{C}^{2 \times 1}$ . Multiplying both sides of (7.8) on the left by  $([M_{n1}] [V_o])^H$ , where the superscript  $H$  denotes complex-conjugate transposition, and inverting the resulting  $2 \times 2$  matrix yields the transmission matrix relationship,

$$\mathbf{y}^r = [T_n] \mathbf{y}^l. \quad (7.9)$$

The transmission matrix  $[T(n)]$  relates the modes on the left boundary of the unit cell to the modes on its right boundary. Clearly, for the unperturbed unit cell (7.9) is of the form

$$\mathbf{y}^r = \begin{bmatrix} e^{-\gamma_o D} & 0 \\ 0 & e^{\gamma_o D} \end{bmatrix} \mathbf{y}^l = [T_o] \mathbf{y}^l. \quad (7.10)$$

Finally, the assumption is made that the transmission matrix  $[T_n]$  of the  $n$ -th perturbed cell can be expressed as the product of the ideal transmission matrix,  $[T_o]$  and a perturbation matrix,  $[Q_n]$  [82],

$$[T_n] = [Q_n] [T_o]. \quad (7.11)$$

Since we can compute matrix  $[T_n]$  for each realization of the geometry in the random space and  $[T_o]$  for the unperturbed case, matrix  $[Q_n]$  is computed directly from (7.11).

With all the aforementioned matrices defined, standard microwave network analysis techniques are used to calculate the transmission characteristics of a structure consisting of the cascade of  $N$  cells exhibiting disorder. Under the

assumption that cells with index  $n > N$  exhibit no disorder, such an analysis may be used to obtain an effective propagation factor per cell that quantifies the transmission attributes of the structure and is defined as follows [82],

$$\gamma D = \lim_{N \rightarrow \infty} \frac{1}{N} \ln(t_{22}), \quad (7.12)$$

where  $t_{22}$  is the element (2,2) of the matrix  $[T_T]$  that represents the overall transmission of a wave traveling from left to right from the input of perturbed cell 1 to the output of perturbed cell  $N$ ,

$$[T_T] = [T_N] [T_{N-1}] \cdots [T_1]. \quad (7.13)$$

While standard Monte Carlo analysis may be used for the calculation of the propagation factor in the presence of statistical variability, under the assumption of an infinitely long disordered period structure (i.e., for the case  $N \rightarrow \infty$ ), closed-form expressions for its calculation are possible under the assumption of small, moderate, and even strong reflections between adjacent cells, as detailed in [82] and in the Appendix C. In particular, for the case of small reflections it is,

$$\gamma_s D = \gamma_o D - \int \ln(q_{22}(\chi)) \rho(\chi) d\chi, \quad (7.14)$$

where the subscript  $s$  in  $\gamma_s$  is used to indicate that this value of the propagation constant is the one obtained under the assumption of small reflections. For the case of moderate reflections, the closed-form expression becomes

$$\begin{aligned} \gamma_m D = & \gamma_s D - \int \ln(q_{22}(\chi)) \rho(\chi) d\chi + \\ & \int \int \ln\left(1 + \frac{e^{-2\gamma_o D} q_{12}(\chi_2) q_{21}(\chi_1)}{q_{22}(\chi_2) q_{22}(\chi_1)}\right) \rho(\chi_1) \rho(\chi_2) d\chi_1 d\chi_2. \end{aligned} \quad (7.15)$$

The subscript  $m$  in  $\gamma_m$  indicates that this value of the propagation constant is the one obtained under the assumption of moderate reflections. In the above equations,  $q_{ij}$  ( $i, j = 1, 2$ ) denote the elements of the perturbation matrix  $[Q_n]$  defined in (7.11).

Under the approximation of small reflections, it is understood that the impact of multiple reflections between adjacent cells can be assumed negligible. In this case, the integration in (7.14) is carried out over the random domain of  $\chi$ , and it is done by using a quadrature rule.

For such purposes, we need to perform a number of FEM simulations to compute matrix  $[Q_n]$  and its element  $q_{22}$  for each node of a sparse grid in the random space. Once the samples of  $q_{22}$  are found we can approximate integral (7.14) with a simple weighted sum of  $R$  evaluations of the integrand.

The case of moderate reflections is understood to represent the situation where reflections between adjacent cells are not negligible and must be accounted for in the calculation of the perturbed propagation constant. Thus, in this case the random space is two-dimensional, defined in terms of the two random variables  $\chi_1$  and  $\chi_2$  in (7.15), associated with unit cells  $n$  and  $n - 1$ , and contributing the impact of the inter-cell reflection to the value of the effective propagation factor. Since perturbation in one unit cell is assumed to be described by statistics independent from the perturbation in other cells, these two variables correspond to the same random variable  $\chi$  and share the same distribution. Therefore, even though a two-dimensional quadrature rule is involved in this case for the calculation of the integral in (7.15), the points on the tensor grid utilized for this purpose involves the points of the one-dimensional quadrature along each dimension. Thus, the matrix  $[Q]$  whose elements appear in (7.15) needs to be computed for the same values of the one-dimensional quadrature rule. Consequently, the same number,  $R$ , of finite element solutions is needed for the calculation of  $[Q]$  for both the case of small reflections and the case of moderate reflections.

#### 7.4.1 Chain of Unit Cells

As already mentioned, (7.14) and (7.15) are meant to be used for structures of a sufficiently large number of unit cells to approximate the case of an infinite disordered periodic structure. Their simplicity begs the question whether they can be used as approximations to the propagation factor per unit cell of finite disordered periodic structures involving a small number of unit cells. This possibility can be assessed in a straightforward fashion through the approximation of equation (7.12) by the mean value of  $\ln(t_{22})$  for the case of the matrix  $[T_T]$  computed from (7.13) for a finite structured involving a small number of cells.

With  $N$  being the number of cells, the pertinent integral is

$$\gamma D = \int d\boldsymbol{\chi} \ln(t_{22}(\boldsymbol{\chi})) \rho(\boldsymbol{\chi}), \quad (7.16)$$

where  $\boldsymbol{\chi}$  is the vector of the random variables  $\chi_i$ ,  $i = 1, 2, \dots, N$ , that quantify the disorder in each unit cell and  $\rho(\boldsymbol{\chi})$ , their joint probability distribution. For the special case of  $N = 1$ , the above equation reduces to the small-reflections equation one (7.14). An advantage of (7.16) is that we can prescind of assumption (7.11), necessary for the moderate-reflections approach presented by Cai. Instead of a brute-force Monte Carlo scheme, an efficient multivariate quadrature rule, based on the sparse Smolyak algorithm [89, 41] is employed for the numerical calculation of (7.16). In this manner, the approximation of (7.16) through the weighted sum of function evaluations,

$$\gamma D \approx \sum_{r=1}^R \ln(t_{22}(\boldsymbol{\chi}_r)) \rho(\boldsymbol{\chi}_r) w_r, \quad (7.17)$$

involves a number of nodes,  $R$ , over the random space that is significantly smaller than the one involved in a tensor product grid and is determined by the Smolyak accuracy level. The details on the selection of the Smolyak grid nodes,  $\boldsymbol{\chi}_r$ , and the associated weights,  $w_r$ , for a given level of accuracy can be found in [41].

The evaluation of (7.17) requires the computation of the transmission matrix for the chain of  $N$  unit cells. From the point of view of the finite element solution of this problem, the number of degrees of freedom in the discrete model for the entire structure is roughly  $N$  times that of the discrete model for a single unit cell. Clearly, the computational cost of such an approach is significant, especially considering that the dimension of the random space is  $N$ . Thus, a more computationally efficient alternative is desired.

Such an alternative is offered by computing, instead, the transmission matrices of the  $N$  single unit cells involved in the structure and then applying (7.13) to obtain the overall matrix for each realization of the structure in the random space. This approach allows us not only to reduce the computational cost associated with the finite element solution of the  $N$ -cell structure, but also to reduce the number of solutions needed. More specifically, the assumption that the variables of each unit cell are identically distributed allows us to employ a multidimensional Kronrod-Patterson quadrature rule

[41] whose  $N$ -tuples nodes are different combinations of the nodes associated with a much simpler one-dimensional quadrature rule. Therefore, similarly to the calculation of the two-dimensional integral in (7.15), we only need to obtain finite element solutions for the unit cell at the nodes of the one-dimensional grid. Thus, the bulk of computational cost of this alternative is approximately the same to the one for (7.14).

## 7.5 Validation Studies

In this section, we use the presented methodology to compute the localization factor,  $\gamma D$  of the disordered waveguide as shown in Fig. 7.5. Its real part represents the exponential decay per unit cell that the wave suffers as it travels through the disordered structure. For its calculation using integrals (7.14) and (7.15), a one-dimensional quadrature rule with Smolyak accuracy of level 3 is utilized. Thus, the finite element solver used to compute matrices  $[T]$  for a single unit cell needs to be run only three times for each frequency, corresponding to the grid points in the random space given by the quadrature rule. This should be contrasted to the calculation of (7.17) with  $N = 4$ , where the finite element solver for the four-cell disordered geometry had to be run 33 times for each frequency. Once the transmission matrices have been found and the corresponding distribution of the random variable characterized, the localization factor,  $\gamma D$  is numerically computed with a summation as shown in (7.17).

Referring to the geometry of Fig. 7.5, a structure with  $H/D = 1$  and  $w = t = 0.2D$  was analyzed. A Gaussian random variable with zero mean and standard deviation 0.05 was employed to quantify the cell length disorder. Figure 7.7 depicts the calculated decay per unit cell, plotted versus  $k_o D = \omega D/c$ , where  $\omega$  is the angular frequency and  $c$  is the speed of light in vacuum. In the figure, a comparison is offered of the ideal case of a perfect periodic structure exhibiting zero attenuation in the pass band, with results obtained using four different approaches: (a) the small-reflection formula (7.14) (black dashed lines); (b) the moderate-reflection formula (7.15) (gray asterisks); (c) the calculation of (7.17) for  $N = 4$  with the chain-of-cells approach (red circles); (d) the calculation of (7.17) for  $N = 4$  with the overall transmission matrix obtained as the product of the four transmission matrices for the four

unit cells with each cell modeled individually (white circles).

As mentioned in the introduction, we have previously considered the use of the ideas from Anderson localization to the expedient analysis of the impact of disorder of a transmission line-based metamaterial on its transmission properties [83] and validated their accuracy using a brute-force Monte Carlo analysis. Because of the increased computational cost of brute-force Monte Carlo when finite element models are necessary for the numerical analysis of the structures of interest, we have relied on the use of sparse grid sampling of the random space [13] for the Monte Carlo analysis of the four-unit-cells structure.

It is clear from Fig. 7.7 that the computed attenuation (real part of  $\gamma$ ) using (7.14) under the assumption of small reflections is in agreement with the results obtained from the more expensive calculation using (7.17) as well as the alternatives moderate reflections and matrix-concatenation approach, especially for frequencies to the left of the stop-band. The simulation times of a MATLAB<sup>®</sup> code running on a 2.50 GHz Xeon CPU Windows machine for the small reflections approach for different number of unit cells are compared in Fig. 7.8. The advantage of using a reduced number of unit cells in terms of computational time is evident. If higher accuracy is desired, the more computationally expensive approach (chain of unit cells) is recommended to be used.

Also depicted in Fig. 7.7 is the result from the evaluation of expression (7.14) using the distribution depicted in Fig. 7.6 that was estimated using the nonparametric diffusion-mixing based KDE from 30 randomly chosen samples (blue dotted line). It is evident from Fig. 7.7 that the computed results are in excellent agreement with the other approaches that use analytical Gaussian distribution for the random variable describing the disorder. This suggests that the proposed nonparametric diffusion-mixing based KDE approach is a promising candidate for the description of uncertainty in input parameters from a limited set of experimentally obtained data.

Figure 7.9 depicts the average perturbation in the imaginary part of the propagation constant caused by the disorder for a range of standard deviation values. As expected, the cases with larger disorder, described in terms of a larger standard deviation, result in higher perturbation in the pass band. While the real part of  $\gamma$  describes field attenuation per unit cell, the perturbation in the imaginary part of  $\gamma$  quantifies the resulting change in the phase

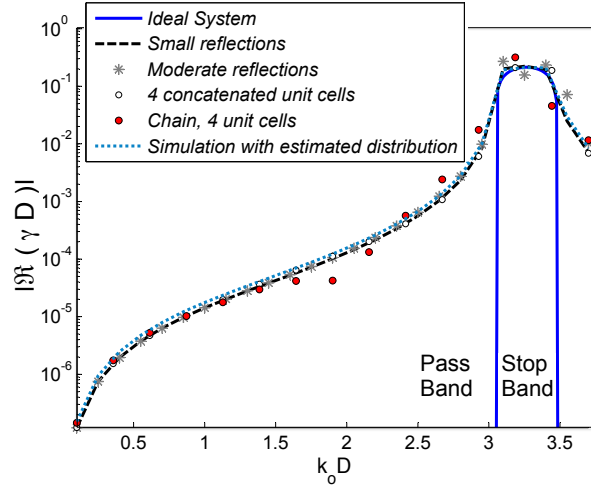


Figure 7.7: Localization factor for the periodic structure of Fig. 7.5, due to a random perturbation in the length of the unit cell following a Gaussian distribution of zero mean and standard deviation of  $\text{std} = 0.05$ .

shift per unit cell of the transmitted wave.

## 7.6 The Case of Multiple Random Variables

Thus far, the discussion has focused on the case where the disorder in the unit cell is described in terms of a single random variable. In the general case, several random variables may be required for the description of geometric and material uncertainty. Each of these variables contributes to the perturbation in the propagation factor per unit cell. The resulting perturbation can be computed using a slightly modified version of (7.16),

$$\Delta\gamma D = -\gamma_o D + \int d\boldsymbol{\chi} \ln(t_{22}(\boldsymbol{\chi})) \rho(\boldsymbol{\chi}), \quad (7.18)$$

where  $\boldsymbol{\chi}$  is a vector containing the  $m$  random variables,  $\chi_i$ ,  $i = 1, 2, \dots, m$ , describing the random disorder. Assuming that these variables are independent, their joint PDF,  $\rho(\boldsymbol{\chi})$ , is simply the product of the  $m$  PDFs. Again, by making use of a sparse grid integration algorithm, the number of full-wave simulations needed for the calculation of the integral over the random domain can be reduced.

As an alternative to the aforementioned approach for calculating the change

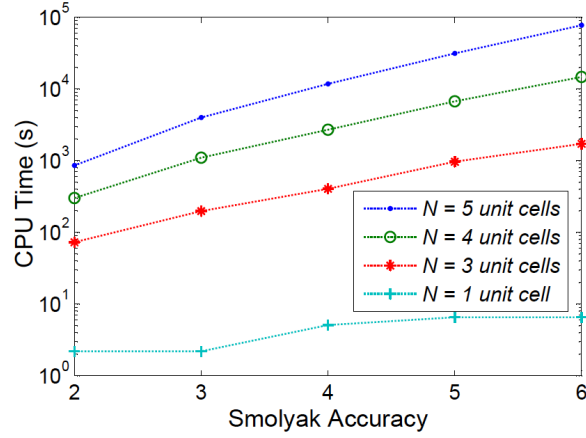


Figure 7.8: Simulation times of a MATLAB code running in a 2.50 GHz Xeon CPU machine per frequency point for chains of 5, 4, 3 and 1 unit cells as a function of the sparse grid algorithm accuracy.

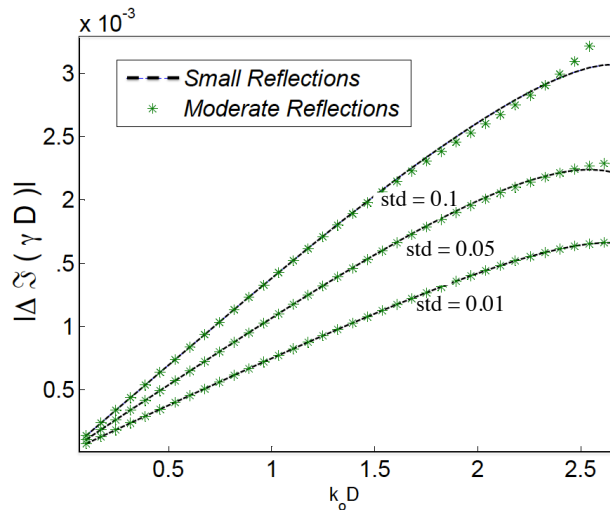


Figure 7.9: Perturbation in the imaginary part of the propagation constant per unit cell for the periodic structure of Fig. 7.5, due to a random perturbation in the length of the unit cell following a Gaussian distribution of zero mean and standard deviation of value  $\text{std} = 0.01, 0.05, \text{ and } 0.1$ .

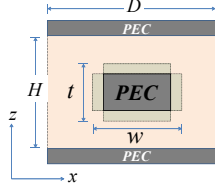


Figure 7.10: The case of a unit cell with two sources of disorder, namely, the width and the thickness of the  $y$ -directed conducting strips.

in the propagation factor per unit cell, Kissel proposed in [80] that the localization factor due to several sources of random disorder may be computed as the sum of the individual localization factors obtained by considering each source by itself,

$$\Delta\gamma = \sum_{i=1}^m \Delta\gamma_i. \quad (7.19)$$

Clearly, the advantage of this alternative is that it results in a small number of finite element solutions per frequency point, equal to  $mR$ , where  $R$  is the number of nodes in a one-dimensional quadrature grid over the interval of each random variable.

To examine the validity of this assertion, we consider the case of a periodic waveguide of the type depicted in Fig. 7.5 where the disorder in the unit cell is described in terms of two parameters, namely, the width and the thickness of the cross-sectional geometry of the  $y$ -directed wires. More specifically, we have

$$w = w_o(1 + \chi_1), \quad (7.20)$$

and

$$t = t_o(1 + \chi_2), \quad (7.21)$$

as shown in Fig. 7.10. In the above equations  $w_o = t_o = 0.2D$ , and the random variables,  $\chi_1, \chi_2$  follow Gaussian distributions with zero mean and standard deviations of 0.2 and 0.1, respectively.

For the evaluation of equation (7.18), a two-dimensional Smolyak grid is utilized involving 37 points and of accuracy level of 5. Thus, 37 finite element solutions per frequency point are needed. In contrast, by considering separately each one of the two sources disorder and then adding up the calculated perturbations in the propagation factor to calculate the overall

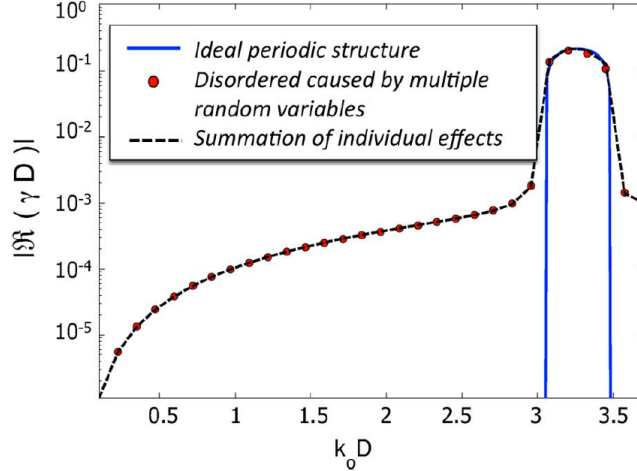


Figure 7.11: Real part of propagation constant per unit cell for the disordered structure of Fig. 7.10 involving two sources of random disorder.

change according to (7.19), nine finite element solutions per frequency point are required for each source. Figures 7.11 and 7.12 contrast the results from the two approaches. Shown in Fig. 7.11 is the real part of the propagation constant per unit cell, plotted versus  $k_o D = \omega D/c$ , while the imaginary part of the change in the propagation constant per unit cell is shown in Fig. 7.12. Very good accuracy is observed, supporting Kissel’s conjecture and the merits of (7.19) as an expedient, yet accurate, means for computing the change in the propagation constant of the wave due to multiple sources of random disorder in the periodicity of the waveguide structure.

## 7.7 Concluding Remarks

In summary, a methodology has been presented for the calculation of the impact of random disorder in periodic electromagnetic waveguides on their transmission characteristics. Rather than using a Monte Carlo scheme where the entire structure, which may consist of several disordered unit cells, is solved using an electromagnetic field solver for each realization in the random space, the proposed method makes use of ideas from the Anderson localization theory to limit the numerical modeling to the unit cell only. More specifically, under appropriate conditions that are expected to hold in many of the applications of interest, closed-form expressions are used to calculate a disorder-induced attenuation factor per unit cell. The accuracy of these

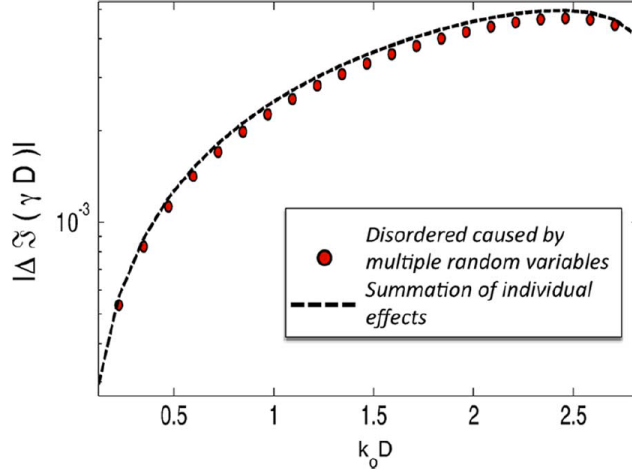


Figure 7.12: Imaginary part of the change in the propagation constant per unit cell for the disordered structure of Fig. 7.10 involving two sources of random disorder.

expressions has been assessed through the use of more general, yet computationally more expensive models, and has been found to be sufficient for the cases studied.

Also addressed in the chapter is the issue of the proper modeling of the random disorder in the structure for those cases where a probability density function for its description is not readily available and its modeling has to rely upon experimentally obtained data. For such cases it was shown that the diffusion-mixing based kernel density estimator of [125] can be used reliably to obtain the probability density function for the random variables that describe geometric uncertainty.

For the case where the random disorder in the structure requires multiple random variables for its description, the possibility of computing the overall change in the propagation constant per unit cell as the sum of the changes computed by considering each random variable individually was examined. Very good accuracy was obtained for the structures considered, suggesting that such an approach has merit and should be used as a first option, especially for cases where the dimension of the random space describing the disorder is large.

While the proposed method was demonstrated in the context of a two-dimensional waveguide, its extension to the general case of three-dimensional waveguides exhibiting periodicity along the direction of wave propagation is

straightforward. It is emphasized that the electromagnetic modeling in the proposed approach relies upon the calculation of the transmission matrix for the unit cell of the structure, which, in turn, can be carried out using any appropriate electromagnetic field solver.

## Chapter 8

# CONCLUSIONS

The work presented in this dissertation is a compilation of original contributions for the efficient assessment of stochastic electromagnetic applications. The proposed methodologies are based on the Stochastic Collocation (SC) method and the Smolyak algorithm, discussed in the second chapter, that reduces the computational effort of the statistical simulation in comparison with traditional Monte Carlo simulation by interpolating the desired output in terms of a set of basis functions which results in an efficient multivariate quadrature rule allowing the fast calculation of the corresponding probability density function of the output of interest. The following is an itemized list of the new stochastic-collocation based contributions presented in this dissertation.

1. **Development of a random space dimensionality reduction technique for the expedient statistical assessment of structures with manufacturing variability and estimation of production yield.** Even though sparse grid collocation is an efficient alternative to reduce the number of iterations in statistical simulations in comparison with traditional Monte Carlo simulation, its efficiency is challenged when the dimensionality of the random space becomes relatively large. In view of this, an approach to reduce the dimensionality of the input random space and thus the number of simulations associated with the SC simulation was proposed. More specifically, we propose a modified Principal Component Analysis (PCA) that constructs a new, reduced random space by taking into account not only the interdependencies of the input random variables but also the sensitivity of the output response on each one of the input random variables by introducing an a-priori sensitivity analysis that improves the accuracy of the simulation. In the next step of our proposed methodology, Adaptive Sparse Grid Collocation (ASGC) is employed to sample the reduced space and

obtain an interpolation of the output in terms of the reduced-space parameters. In this way, the number of simulations is reduced two to three times in comparison with the full-order case in the considered numerical examples. Additionally, a technique based on the cross entropy algorithm was employed to expedite the calculation of the production yield of structures and systems exhibiting manufacturing variability. It was demonstrated that the cross-entropy algorithm offers an efficiency 10 times higher than the Monte Carlo simulation for estimating the yield.

2. **Development of a stochastic macromodel boundary condition for the efficient random electromagnetic simulation of structures with uncertain subdomains.** A methodology based on the impedance/admittance matrix concept was proposed to construct a stochastic macromodel of subdomains exhibiting geometric and/or material randomness that are part of a group of targets exhibiting variability. The model of the sub-region is defined in terms of a fixed mathematical boundary expanded in terms of orthogonal polynomials of the random variables that parameterize the subdomain. This approach simplifies the complexity of a stochastic collocation numerical solution, compounded by the need to generate a discrete numerical model for each one of the geometries resulting from the sampling of the multidimensional random space defining the randomness of the structure. The simplification is achieved by imposing a fixed circular boundary surrounding each subdomain where the corresponding impedance/admittance boundary condition is evaluated for each sample of the random space. Consequently, the approach is specially useful for complicated geometries with intricate details and disparities in feature size between scatterers. The proposed macromodel technique was extended next to characterize the broadband response of a random subdomain by means of the application of a Krylov-subspace model order reduction technique. Besides, the use of a recursive algorithm based on the addition theorem, allows the application of the transition matrix to solve scattering problems with multiple scatterers.
3. **Development of statistical framework for the study of interconnects with random permittivity profile.** We propose a method-

ology to assess the impact of statistical variability on the transmission properties of interconnects. Such uncertainty is assumed to be localized, in the sense that non-uniform changes in material properties occur throughout the structure under consideration. Specifically, we present the example of a transmission line with a random permittivity profile. The result is an effective homogeneous permittivity model is constructed in terms of orthogonal polynomials. The construction of the model has been expedited by using a dimensionality reduction algorithm and an efficient multivariate integration technique based on the Smolyak algorithm. The resulting homogeneous model was used to estimate the impact on the propagation time of a wave when it travels through the interconnect structure, which predicts the distortion of the signal and desynchronization of the system quantified in terms of an induced random jitter.

4. **Statistical assessment of the impact of routing uncertainty in the early design stages of printed circuit board interconnects.**

A methodology, aimed for use in early stages in the design phase where floor planning and layout specificity is still lacking, is proposed as an efficient predictive analysis of the impact of the uncertainty in the routing of interconnects on their transmission attributes. The technique achieves its efficiency by combining the ideas of passive multi-variate parametric macromodeling with a representation of the interconnect channel in terms of a concatenation of several sections with conductor spacing at their end points controlled by the routing uncertainty.

5. **Efficient assessment of statistical disorder on the filtering properties of periodic waveguides.**

A methodology for the quantification of the impact of random disorder in periodic electromagnetic waveguides on their transmission properties is developed. The proposed method makes use of ideas from the Anderson localization theory to limit the numerical modeling to the unit cell only. More specifically, under appropriate conditions that are expected to hold in many of the applications of interest, closed-form expressions are used to calculate a disorder-induced attenuation factor per unit cell. The accuracy of these expressions has been assessed through the use of more general, yet computationally more expensive models, and has been found to be

sufficient for the cases studied. For the case where the random disorder in the structure requires multiple random variables for its description, the possibility of computing the overall change in the propagation constant per unit cell as the sum of the changes computed by considering each random variable individually was examined. Very good accuracy was obtained for the structures considered, suggesting that such an approach has merit and should be used as a first option, especially for cases where the dimension of the random space describing the disorder is large.

In a summary, a number of stochastic modeling applications has been developed in the context of computational electromagnetics. The models allow the treatment of multidimensional problems by interpolating the output of interest as a function of the input random variables, propagating the uncertainty in the computational process. Considering that some electromagnetic simulations are computationally expensive, it was demonstrated that these techniques are excellent alternatives to the brute-force Monte Carlo approach by keeping the number of simulations considerably small while the accuracy of the approximation is preserved. The stochastic collocation-based techniques are utilized not only in examples where global uncertainty occurs but also in examples presenting localized uncertainty for which macromodeling methodologies have been employed to expedient the statistical assessment of structures. The studied stochastic problems are important technology applications and their stochastic modeling is crucial for the correct assessment of the impact of uncertainties on their electromagnetic behavior.

## 8.1 Future Work

This dissertation presents efficient techniques for the statistical assessment of electromagnetic systems and structures. Here we describe some potential extensions of the proposed methodologies to solve a broader range of problems as well as additional research opportunities in the field of stochastic modeling in computational electromagnetics.

First, the dimensionality reduction methodology can be extended by employing nonlinear principal components analysis (PCA), which has been

broadly researched in the last couple of decades [129, 130], to reduce the input random space when the relations between random variables are not linear.

Another important extension of our stochastic collocation method concerns the yield estimation methodology that, if combined with optimization techniques can be used to derive an optimal set of ranges of the manufacturing tolerances of the design parameters of electromagnetic structures that optimizes the manufacturing cost. That optimization technique must take into account the number of units that fail a certain performance criterion as well as the cost of demanding such tolerances for the input random parameters.

Regarding the topic of stochastic macromodeling, the stochastic admittance/impedance boundary condition methodology needs to be extended to analyze three-dimensional structures with surrounding boundaries of arbitrary shape. For such a purpose, spherical wave functions need to be used instead of cylindrical harmonics to expand the fields and characterize the boundary condition. As a result, a more versatile methodology can be applied to the context of EMI (electromagnetic interference) and EMC (electromagnetic compatibility) applications to simplify the extraction of the statistics of the electromagnetic field in cavities and electronic structures presenting variability.

As for the signal integrity applications, we recognize an interesting application of practical importance for the computer industry, namely, the modeling of the fiber weave effect that is introduced due to non-homogeneous nature of the dielectrics of printed circuit boards caused by the fiberglass weave pattern. Such variability is specially important for bit rates higher than 5 GB/s and for differential pair traces, that introduces timing skew and mode conversions leading to the detriment of the intended performance and EMI radiation [131]. Instead of focusing in the worst case scenarios as it has traditionally been done, some of the proposed stochastic modeling techniques can be used to assess the impact on the transmission properties of high-speed interconnects.

Finally, an obvious extension for the problem of disordered periodic structure is the study of periodic arrays and structures in two or three dimensions. Another extension of the methodology concerns the case of multimode propagation. In such scenario, the impact of disorder is not only on each individual propagating mode but also in the mode conversion between them. Such ef-

fects need to be quantified for a complete assessment of disorder in periodic structures.

# Appendix A

## INTEGRAL EQUATION SOLVER

The mathematical framework of the method of moments is described in this appendix. The integral equation solver is employed to study the two-dimensional scattering of a dielectric cylinder with arbitrary shape in Chapter 2. This study assumes an homogeneous infinite dielectric cylinder immersed in free space. The formulation has been detailed in [91, 104], where a combination of the Helmholtz wave equation and Green's function is integrated inside and outside the cylinder's domain to get an integral equation of the fields at the boundary of the cylinder. Specifically, for the transverse magnetic (TMz) mode the integral equation is

$$\frac{1}{2}E_z(\rho) - \int_{S_o-s} \left[ E_z(\rho') \frac{\partial G_o(\rho, \rho')}{\partial n'} - jk_o Z_o G_o(\rho, \rho') H_t(\rho') \right] dS' = E_z^{inc}(\rho), \quad (\text{A.1})$$

$$\frac{1}{2}E_z(\rho) + \int_{S_o-s} \left[ E_z(\rho') \frac{\partial G_i(\rho, \rho')}{\partial n'} - jk_o Z_o \mu_r G_i(\rho, \rho') H_t(\rho') \right] dS' = 0, \quad (\text{A.2})$$

where the continuity condition of the fields has been imposed. Also, in (A.1) and (A.2),  $G_i(\rho, \rho')$  is the Green's function of the region inside the cylinder, and  $S_o$  is the boundary of the cylinder. Notice that the integration domain excludes the singularity ( $s$ ) of the Green's function that arises when  $\rho = \rho'$ . Similarly, for the transverse electric (TEz) mode we have

$$\frac{1}{2}H_z(\rho) - \int_{S_o-s} \left[ H_z(\rho') \frac{\partial G_o(\rho, \rho')}{\partial n'} + jk_o Z_o G_o(\rho, \rho') E_t(\rho') \right] dS' = H_z^{inc}(\rho) \quad (\text{A.3})$$

and

$$\frac{1}{2}H_z(\rho) + \int_{S_o-s} \left[ H_z(\rho') \frac{\partial G_i(\rho, \rho')}{\partial n'} + jk_o Z_o \varepsilon_r G_i(\rho, \rho') E_t(\rho') \right] dS' = 0, \quad (\text{A.4})$$

for  $\rho \in S_o$ .

Equations (A.3) and (A.4) are reduced to a linear set of equations by sectioning the boundary into smaller segments. Then, by assuming that the fields are constant on each section of the boundary, a matrix equation is obtained. For the TM case it is

$$\left( \frac{1}{2} [I] - [A_o] \right) [E_z] + jk_o Z_o [B_o] [H_t] = [E_z^{inc}], \quad (\text{A.5})$$

$$\left( \frac{1}{2} [I] + [A_i] \right) [E_z] - jk_o Z_o [B_i] [H_t] = 0, \quad (\text{A.6})$$

where vectors  $[E_z]$  and  $[H_t]$  represent the interpolation values of the fields on each section of the boundary. Besides,

$$A_{mn} = \frac{1}{4j} \frac{\hat{n}(\rho_n) \cdot (\rho_m - \rho_n)}{|\rho_m - \rho_n|} H_1^{(2)}(k|\rho_m - \rho_n|) l_n, \quad m \neq n, \quad (\text{A.7})$$

$$B_{mn} = \begin{cases} \frac{1}{4j} H_o^{(2)}(k|\rho_m - \rho_n|) l_n & m \neq n \\ \frac{1}{4j} \left( 1 + \frac{2}{j\pi} \ln \left( \frac{\gamma k l_m}{4e} \right) \right) l_m & m = n \end{cases}, \quad (\text{A.8})$$

where vector  $\hat{n}$  is the unitary normal vector on each segment of the boundary of length  $l_n$ .

## Appendix B

### CROSS ENTROPY ALGORITHM

The Cross-Entropy (CE) algorithm presented in [99, 97] provides an efficient methodology to estimate the probability of rare events. This algorithm, shown below is used in this manuscript to estimate the yield of microwave structures under manufacturing uncertainty.

For a given random parameter  $u = u(\boldsymbol{\chi})$ , where  $\boldsymbol{\chi}$  is a multidimensional random variable with PDF  $f(\boldsymbol{X}; \boldsymbol{\mu})$  and mean vector  $\boldsymbol{\mu}$ . The present algorithm finds the probability of  $u$  to be larger than a threshold  $\gamma$ .

1. Define  $\boldsymbol{v}_0 = \boldsymbol{\mu}$ . Set  $t = 1$ .
2. Generate a sample  $\{\boldsymbol{\chi}_i\}_{i=1}^M$  from the PDF  $f(\boldsymbol{X}, \boldsymbol{v}_{t-1})$ , sort them and evaluate the output  $u$ . If  $u(\boldsymbol{\chi}_{\lceil(1-\rho)M\rceil}) < \gamma$ , assign the  $\lceil(1-\rho)M\rceil$ -th largest value of the output,  $u$  to  $\gamma_t$ . Otherwise set  $\gamma_t = \gamma$ .
3. Evaluate the following expression to find  $\boldsymbol{v}_t$ .

$$v_{t,j} = \frac{\sum_{i=1}^M I_{\{u(\boldsymbol{\chi}) \geq \gamma_t\}} W(\boldsymbol{\chi}_i; \boldsymbol{\mu}, \boldsymbol{v}_{t-1}) \chi_{ij}}{\sum_{i=1}^M I_{\{u(\boldsymbol{\chi}) \geq \gamma_t\}} W(\boldsymbol{\chi}_i; \boldsymbol{\mu}, \boldsymbol{v}_{t-1})}, \quad (\text{B.1})$$

where  $W(\boldsymbol{\chi}_i; \boldsymbol{\mu}, \boldsymbol{v}) = f(\boldsymbol{X}; \boldsymbol{\mu})/f(\boldsymbol{X}; \boldsymbol{v})$  is the ratio between the original and the modified PDF.

4. If  $\gamma_t < \gamma$ , set  $t = t + 1$  and reiterate from step 2. Otherwise proceed with step 5.
5. Estimate the rare-event probability  $y$  using the *likelihood ratio* estimator

$$y = \frac{1}{M_1} \sum_{i=1}^{M_1} I_{\{u(\boldsymbol{\chi}) \geq \gamma_t\}} W(\boldsymbol{\chi}_i; \boldsymbol{\mu}, \boldsymbol{v}_T), \quad (\text{B.2})$$

Notice that in the algorithm the mean values of the PDF changes in each iteration. Other parameters can be assigned to change similarly. Besides, the parameter  $M$  is normally chosen to be  $10^3$  and  $\rho$  between 0.1 and 0.005.

## Appendix C

# LOCALIZATION TECHNIQUE FOR ONE-DIMENSIONAL PERIODIC STRUCTURES

This localization technique has been proposed in [82] and it is described in this appendix for completeness purposes. Consider the  $n$ -th unit cell of a periodic structure. The transmission properties of the cell can be quantified in terms of the transfer matrices relating the output to the input modal fields. It is assumed that the transmission matrix of the modes is given by the product of an ideal section  $[T_o]$  of the structure without variability, while  $[Q_n]$  is used to capture the perturbation of the unit cell as depicted in Fig. C.1.

Referring to Fig. C.1, the modal wave vectors are  $[a_n, b_n]$ , where  $a_n$  represents a wave traveling to the right, while  $b_n$  represents a wave traveling to the left. Following the formulation presented by Cai and Lin [82], the overall transfer matrix  $[T_T]$  for a chain of  $N$  cell units is obtained by a consecutive product of  $N$  matrices  $[T_o][Q_n]$ .

$$[T_T] = [Q_N] [T_o] [Q_{N-1}] [T_o] \dots [Q_1] [T_o], \quad (\text{C.1})$$

where  $[T_o]$  is a diagonal matrix whose components relate the wave at the output of the ideal unit cell with the input wave, introducing a magnitude and phase change,

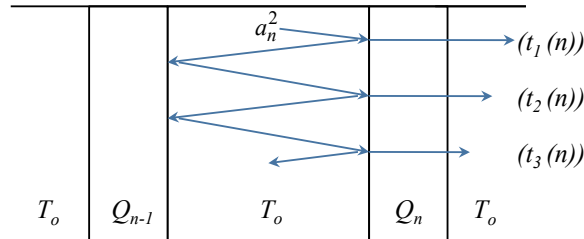


Figure C.1: Schematic representation of reflections in the  $n$ -th cell due to perturbation.

$$[T_o] = \begin{bmatrix} \lambda & 0 \\ 0 & \lambda^{-1} \end{bmatrix}. \quad (\text{C.2})$$

Scattering matrix  $[S_T]$ , defined in [82], provides a relevant physical insight into the problem since its coefficients correspond to the reflection and transmission coefficients of the propagating waves for the overall structure. The overall scattering matrix is

$$\begin{bmatrix} b_1 \\ a_{N+1} \end{bmatrix} = [S_T] \begin{bmatrix} a_1 \\ b_{N+1} \end{bmatrix} = \begin{bmatrix} S_{11} & S_{12} \\ S_{21} & S_{22} \end{bmatrix} \begin{bmatrix} a_1 \\ b_{N+1} \end{bmatrix}. \quad (\text{C.3})$$

Assuming there are no reflections for cells  $n \geq N + 1$ , the second row of (C.3) results in

$$a_{N+1} = S_{21}a_1, \quad (\text{C.4})$$

where  $S_{21}$  represents the transmission of the wave moving to the right. A propagation factor of the wave is then defined through the equation

$$\gamma = \lim_{N \rightarrow \infty} \frac{1}{N} \ln(S_{21}). \quad (\text{C.5})$$

Clearly, this propagation factor represents a measure of the phase shift and attenuation in the disordered structure per unit cell. While standard Monte Carlo analysis may be used for the calculation of the propagation factor in the presence of statistical variability, closed-form expressions for their calculation under the assumption of small, moderate and strong reflections are possible, as detailed in [82] and described next.

## C.1 Small Reflections

Considering the schematics of Fig. C.1, and assuming that the reflections from the perturbation is small, the only transmitted part of the incident wave  $a_n^2$  would be  $t_1(n)$  and is given by

$$t_1(n) = s_{21}(n) a_n^2, \quad (\text{C.6})$$

where  $s_{21}(n)$  is the scattering parameter corresponding to the  $n$ -th perturbation section.

Then, the overall transmission coefficient  $S_{21}$  is approximated by the product of transmission coefficients of each perturbation section,  $s_{21}(n)$ , and  $\lambda$  corresponding to each ideal section of the cell, resulting in

$$S_{21} \approx \prod_{n=1}^N s_{21}(n) \lambda, \quad (\text{C.7})$$

that expressed in terms of the coefficients of matrices  $[Q(n)]$  is

$$S_{21} \approx \prod_{n=1}^N q_{22}^{-1}(n) \lambda. \quad (\text{C.8})$$

Plugging (C.8) into (7.12), a summation of independent and identically distributed random variables is obtained which can be estimated with the mean of the random variables, [82]

$$\gamma d = \ln \lambda - \int \ln(q_{22}(\chi)) \rho(\chi) d\chi, \quad (\text{C.9})$$

where  $\rho(\chi)$  is the PDF of the random variables  $\chi$ .

## C.2 Moderate Reflections

The next approximation, called moderate reflections, considers reflections inside each unit cell but no interactions with adjacent cells are considered. The total transmitted wave in each unit cell is the summation of terms  $t_1(n)$ ,  $t_2(n)$ ,  $t_3(n)$ ,... of Fig. C.1. The first three such coefficients are given by

$$\begin{aligned} t_1(n) &= s_{21}(n) a_n^2, \\ t_2(n) &= s_{21}(n) [\lambda^2 s_{11}(n-1) s_{11}(n)] a_n^2, \\ t_3(n) &= s_{21}(n) [\lambda^2 s_{11}(n-1) s_{11}(n)]^2 a_n^2. \end{aligned} \quad (\text{C.10})$$

The transmitted wave in each unit cell  $n$  is given by the summation of coefficients  $t_i(n)$  [82]

$$t(n) = \sum_{i=1}^N t_i(n) a_n^2 = \frac{s_{21}(n) \lambda}{1 - \lambda^2 s_{11}(n-1) s_{11}(n)} a_n^2, \quad (\text{C.11})$$

while the reflected wave in each unit cell is

$$r(n) = \frac{s_{11}(n) s_{21}(n-1) \lambda}{1 - \lambda^2 s_{11}(n-1) s_{11}(n)} a_n^2. \quad (\text{C.12})$$

Then, the overall transmission coefficient,  $S_{21}$  of (C.5) is approximately given by [82]

$$S_{21} \approx \prod_{n=1}^N \frac{s_{21}(n) \lambda}{1 - \lambda^2 s_{11}(n-1) s_{11}(n)}. \quad (\text{C.13})$$

Plugging (C.13) into (7.12) and expressing factors  $s_{ij}(n)$  in terms of coefficients  $q_{ij}(n)$  ( $i, j = 1, 2$ ) of perturbation matrix  $[Q_n]$ , we get [82]

$$\gamma = \ln \lambda - \int \ln(q_{22}(\chi)) p(\chi) d\chi + \iint \ln \left( 1 + \frac{\lambda^2 q_{12}(\chi_2) q_{21}(\chi_1)}{q_{22}(\chi_2) q_{22}(\chi_1)} \right) p(\chi_1) p(\chi_2) d\chi_1 d\chi_2. \quad (\text{C.14})$$

# BIBLIOGRAPHY

- [1] “Getting started with HFSS: A bandpass filter,” Tutorial, Ansoft, May 2010.
- [2] EngineersGarage, “Printed circuit boards (PCBs),” 2013. [Online]. Available: <http://www.engineersgarage.com/articles/printed-circuit-boards-pcb-design-manufacturing?page=6>
- [3] S. Velamparambil, W. C. Chew, and J. Song, “10 million unknowns: Is it that big? [computational electromagnetics],” *IEEE Ant. and Prop. Magazine*, vol. 45, no. 2, pp. 43–58, 2003.
- [4] J. Jackson, *Classical Electrodynamics*. New York: Wiley, 1998.
- [5] B. Butrylo, F. Musy, L. Nicolas, R. Perrussel, R. Scorretti, and C. Voltaire, “A survey of parallel solvers for the finite element method in computational electromagnetics,” *COMPEL: The Int. J. for Computation and Math. in Electrical and Electronic Eng.*, vol. 23, no. 2, pp. 531–546, 2004.
- [6] W. Chew, A. Cangellaris, J. Schutt-Aine, H. Braunisch, Z. Qian, A. Aydiner, K. Aygun, L. Jiang, Z. Ma, L. Meng, and M. Naeem, “Fast and accurate multiscale electromagnetic modeling framework: An overview,” in *Proc. Workshop on Signal and Power Integrity*, 2013, pp. 1–4.
- [7] A. Ishimaru, *Wave Propagation and Scattering in Random Media*. New York: Academic Press, 1978, vol. 2.
- [8] S. Smoljak, “Quadrature and interpolation formulas for tensor products of certain classes of functions,” *Soviet Mathematics*, vol. 4, pp. 240–243, 1963.
- [9] T. Ullrich, “Smolyak’s algorithm, sparse grid approximation and periodic function spaces with dominating mixed smoothness,” Ph.D. dissertation, Friedrich-Schiller-University Jena, Schmalkalden, 1980.
- [10] E. Novak and K. Ritter, “High dimensional integration of smooth functions over cubes,” *Numerische Mathematik*, vol. 75, no. 1, pp. 79–97, 1996.

- [11] W. Sickel and T. Ullrich, “The Smolyak algorithm, sampling on sparse grids and function spaces of dominating mixed smoothness,” Friedrich-Schiller-University Jena, Tech. Rep., Oct. 2007.
- [12] G. Wasilkowski and H. Woźniakowski, “Explicit cost bounds of algorithms for multivariate tensor product problems,” *J. Complexity*, vol. 11, no. 1, pp. 1–56, 1995.
- [13] D. Xiu and J. Hesthaven, “High-order collocation methods for differential equations with random inputs,” *SIAM J. Sci. Computing*, vol. 27, no. 3, pp. 1118–1139, 2005.
- [14] D. Xiu, “Fast numerical methods for stochastic computations: A review,” *Communications in Computational Physics*, vol. 5, no. 2-4, pp. 242–272, 2009.
- [15] W. A. Klimke, “Uncertainty modeling using fuzzy arithmetic and sparse grids,” Ph.D. dissertation, Universität Stuttgart, 2006.
- [16] K. Lee, *EMP Interaction: Principles, Techniques, and Reference Data*. Washington: Taylor & Francis/Hemisphere, 1986.
- [17] D. A. Hill, *Electromagnetic Fields in Cavities: Deterministic and Statistical Theories*. Hoboken: John Wiley & Sons, 2009, vol. 35.
- [18] J. G. Kostas and B. Boverie, “Statistical model for a mode-stirred chamber,” *IEEE Trans. on Electromagnetic Compatibility*, vol. 33, no. 4, pp. 366–370, 1991.
- [19] M. L. Crawford and G. H. Koepke, “Design, evaluation, and use of a reverberation chamber for performing electromagnetic susceptibility/vulnerability measurements,” U.S. Nat. Bur. Stand. Tech., Tech. Rep. 1092, April 1986.
- [20] M. Crawford, T. Loughry, M. Hatfield, and G. Freyer, “Band-limited white Gaussian FMQ excitation for reverberation chambers and applications to radiated susceptibility testing,” U.S. Nat. Inst. Stand. Technol. Tech., Tech. Rep. 1375, 1996.
- [21] D. Hill, “Electronic mode stirring for reverberation chambers,” *IEEE Trans. on Electromagnetic Compatibility*, vol. 36, no. 4, pp. 294–299, 1994.
- [22] R. Holland and R. S. John, *Statistical Electromagnetics*. Philadelphia: Taylor & Francis, 1999.
- [23] T. H. Lehman, “A statistical theory of electromagnetic fields in complex cavities,” *Interaction Notes, Note*, vol. 494, 1993.

- [24] R. Price, H. Davis, and E. Wenaas, "Determination of the statistical distribution of electromagnetic-field amplitudes in complex cavities," *Physical Review E*, vol. 48, no. 6, p. 4716, 1993.
- [25] D. A. Hill, "Plane wave integral representation for fields in reverberation chambers," *IEEE Trans. on Electromagnetic Compatibility*, vol. 40, no. 3, pp. 209–217, 1998.
- [26] D. A. Hill and J. M. Ladbury, "Spatial-correlation functions of fields and energy density in a reverberation chamber," *IEEE Trans. on Electromagnetic Compatibility*, vol. 44, no. 1, pp. 95–101, 2002.
- [27] R. H. Myers and D. C. Montgomery, *Response Surface Methodology: Process and Product Optimization Using Designed Experiments*. New York: Wiley, 2002.
- [28] L. Eriksson, E. Johansson, N. Kettaneh-World, C. Wikstrom, and S. Wold, *Design of Experiments: Principles and Applications*. Umea, Sweden: Umetrics Academy, 2008.
- [29] E. Matoglu, N. Pham, D. De Araujo, M. Cases, and M. Swaminathan, "Statistical signal integrity analysis and diagnosis methodology for high-speed systems," *IEEE Trans. Advanced Packaging*, vol. 27, no. 4, pp. 611–629, 2004.
- [30] E. Felt, S. Zanella, C. Guardiani, and A. Sangiovanni-Vincentelli, "Hierarchical statistical characterization of mixed-signal circuits using behavioral modeling," in *Proc. Int. Conf. Computer-Aided Design*, 1996, pp. 374–380.
- [31] S. Koziel, J. Bandler, A. Mohamed, and K. Madsen, "Enhanced surrogate models for statistical design exploiting space mapping technology," in *Proc. Int. Microw. Symp.*, 2005, pp. 12–17.
- [32] D. Xiu and G. Karniadakis, "The Wiener–Askey polynomial chaos for stochastic differential equations," *SIAM J. Sci. Computing*, vol. 24, no. 2, pp. 619–644, 2002.
- [33] A. Klimke and B. Wohlmuth, "Algorithm 847: Spinterp: Piecewise multilinear hierarchical sparse grid interpolation in MATLAB," *ACM Trans. on Mathematical Software*, vol. 31, no. 4, pp. 561–579, 2005.
- [34] A. Klimke, "Sparse grid interpolation toolbox," January 2006. [Online]. Available: <http://www.ians.uni-stuttgart.de/spinterp/>
- [35] T. Gerstner and M. Griebel, "Dimension-adaptive tensor-product quadrature," *Computing*, vol. 71, no. 1, pp. 65–87, 2003.

- [36] R. Ghanem and P. Spanos, *Stochastic Finite Elements: A Spectral Approach*. New York: Dover Publications, 2003.
- [37] I. S. Stievano, P. Manfredi, and F. G. Canavero, "Parameters variability effects on multiconductor interconnects via Hermite polynomial chaos," *IEEE Trans. Comp. Pack. Manufact. Technology*, vol. 1, no. 8, pp. 1234–1239, Aug. 2011.
- [38] P. Manfredi, I. S. Stievano, and F. G. Canavero, "Parameters variability effects on microstrip interconnects via Hermite polynomial chaos," in *Proc. Elec. Perform. of Electronic Pack. and Syst.*, 2010, pp. 149–152.
- [39] P. Manfredi, D. V. Ginste, D. De Zutter, and F. G. Canavero, "Frequency- and time-domain stochastic analysis of lossy and dispersive interconnects in a SPICE-like environment," in *Proc. Elec. Perform. of Electronic Pack. and Syst.* IEEE, 2012, pp. 65–68.
- [40] A. Rong and A. Cangellaris, "Interconnect transient simulation in the presence of layout and routing uncertainty," in *Proc. Elec. Perform. of Electronic Pack. and Syst.*, Oct. 2011, pp. 157–160.
- [41] F. Heiss and V. Winschel, "Likelihood approximation by numerical integration on sparse grids," *Journal of Econometrics*, vol. 144, no. 1, pp. 62–80, May 2008.
- [42] X. Ma and N. Zabaras, "An adaptive high-dimensional stochastic model representation technique for the solution of stochastic partial differential equations," *J. Comput. Phys.*, vol. 229, no. 10, pp. 3884–3915, May 2010.
- [43] A. Ishimaru, "Wave propagation and scattering in random media and rough surfaces," *Proceedings of the IEEE*, vol. 79, no. 10, pp. 1359–1366, 1991.
- [44] C. Chauviere, J. Hesthaven, L. Wilcox et al., "Efficient computation of RCS from scatterers of uncertain shapes," *IEEE Trans. Ant. and Prop.*, vol. 55, no. 5, pp. 1437–1448, 2007.
- [45] Z. Zeng and J.-M. Jin, "Efficient calculation of scattering variation due to uncertain geometrical deviation," *Electromagnetics*, vol. 27, no. 7, pp. 387–398, 2007.
- [46] B. Gustavsen and A. Semlyen, "Fast passivity assessment for S-parameter rational models via a half-size test matrix," *IEEE Trans. Microwave Theory Tech.*, vol. 56, no. 12, pp. 2701–2708, Dec. 2008.
- [47] B. Gustavsen, "Fast passivity enforcement for S-parameter models by perturbation of residue matrix eigenvalues," *IEEE Trans. on Advanced Packaging*, vol. 33, no. 1, pp. 257–265, Feb. 2010.

- [48] I. S. Stievano, F. Canavero, Z. Chen, G. Katopis, and I. Maio, "Parametric macromodels of drivers for SSN simulations," in *Proc. Int. Symp. on Electromagnetic Compatibility*, vol. 2, 2003, pp. 616–621.
- [49] F. Ferranti, L. Knockaert, and T. Dhaene, "Guaranteed passive parameterized admittance-based macromodeling," *IEEE Trans. Advanced Packaging*, vol. 33, no. 3, pp. 623–629, Aug. 2010.
- [50] F. Ferranti, L. Knockaert, and T. Dhaene, "Parameterized S-parameter based macromodeling with guaranteed passivity," *IEEE Microw. and Wireless Comp. Letters*, vol. 19, no. 10, pp. 608–610, Oct. 2009.
- [51] T. El-Moselhy and L. Daniel, "Variation-aware interconnect extraction using statistical moment preserving model order reduction," in *Design, Automation & Test in Europe Conference & Exhibition*. IEEE, 2010, pp. 453–458.
- [52] P. Sumant, "Stochastic multiphysics modeling of RF MEMS switches," Ph.D. dissertation, University of Illinois at Urbana-Champaign, Urbana, IL, 2010.
- [53] D. Vande Ginste, D. De Zutter, D. Deschrijver, T. Dhaene, P. Manfredi, and F. Canavero, "Stochastic modeling-based variability analysis of on-chip interconnects," *IEEE Trans. Comp. Pack. Manufact. Tech.*, vol. 2, no. 7, pp. 1182–1192, 2012.
- [54] A. Zadehgo, "Probabilistic finite-difference time-domain simulations using stochastic electromagnetic macro-models," Ph.D. dissertation, University of Illinois at Urbana-Champaign, Urbana, IL, 2012.
- [55] R. Ghanem and P. D. Spanos, "Polynomial chaos in stochastic finite elements," *Journal of Applied Mechanics*, vol. 57, pp. 197–202, 1990.
- [56] P. Beckmann and A. Spizzichino, "The scattering of electromagnetic waves from rough surfaces," *Artech House, Inc.*, vol. 1, 1987.
- [57] Q. H. Spencer, B. D. Jeffs, M. A. Jensen, and A. L. Swindlehurst, "Modeling the statistical time and angle of arrival characteristics of an indoor multipath channel," *IEEE Journal on Selected Areas in Communications*, vol. 18, no. 3, pp. 347–360, 2000.
- [58] L. C. Andrews and R. L. Phillips, *Laser Beam Propagation through Random Media*. SPIE Press, 2005, vol. 152.
- [59] R. Wagner, J. Song, and W. Chew, "Monte Carlo simulation of electromagnetic scattering from two-dimensional random rough surfaces," *IEEE Trans. Ant. and Prop.*, vol. 45, no. 2, pp. 235–245, 1997.

- [60] F. G. Bass and I. M. Fuks, "Wave scattering from statistically rough surfaces," *Oxford Pergamon Press International Series on Natural Philosophy*, vol. 93, 1979.
- [61] A. G. Voronovich, *Wave Scattering from Rough Surfaces*. Berlin: Springer, 1999, vol. 2.
- [62] Z.-Q. Tian, B. Ren, and D.-Y. Wu, "Surface-enhanced raman scattering: from noble to transition metals and from rough surfaces to ordered nanostructures," *The Journal of Physical Chemistry B*, vol. 106, no. 37, pp. 9463–9483, 2002.
- [63] M. Nieto-Vesperinas and J. Soto-Crespo, "Monte Carlo simulations for scattering of electromagnetic waves from perfectly conductive random rough surfaces," *Optics Letters*, vol. 12, no. 12, pp. 979–981, 1987.
- [64] E. Mendez and K. O'Donnell, "Observation of depolarization and backscattering enhancement in light scattering from Gaussian random surfaces," *Optics Communications*, vol. 61, no. 2, pp. 91–95, 1987.
- [65] M.-J. Kim, J. Dainty, A. Friberg, and A. Sant, "Experimental study of enhanced backscattering from one- and two-dimensional random rough surfaces," *JOSA A*, vol. 7, no. 4, pp. 569–577, 1990.
- [66] A. Ishimaru, "Experimental and theoretical studies on enhanced backscattering from scatterers and rough surfaces," *Scattering in Volumes and Surfaces*, pp. 1–15, 1990.
- [67] J. Li, L.-X. Guo, and H. Zeng, "FDTD method investigation on the polarimetric scattering from 2-D rough surface," *Progress in Electromagnetics Research*, vol. 101, pp. 173–188, 2010.
- [68] Z.-H. Lai, J.-F. Kiang, and R. Mittra, "Two-dimensional domain-decomposition FDTD method to simulate wave scattering by rough surfaces," in *Proc. European Conference on Antennas and Propagation*. IEEE, 2013, pp. 3839–3842.
- [69] S. P. Morgan, "Effect of surface roughness on eddy current losses at microwave frequencies," *Journal of Applied Physics*, vol. 20, no. 4, pp. 352–362, 1949.
- [70] E. Hammerstad, *Microstrip Handbook*, ser. ELAB report, F. Bekkadal, Ed. Trondheim, Norway: Norwegian Institute of Technology, 1975.
- [71] C. Holloway and E. F. Kuester, "Power loss associated with conducting and superconducting rough interfaces," *IEEE Trans. Microwave Theory Tech.*, vol. 48, no. 10, pp. 1601–1610, 2000.

- [72] L. Tsang, X. Gu, and H. Braunisch, "Effects of random rough surface on absorption by conductors at microwave frequencies," *IEEE Microw. and Wireless Comp. Letters*, vol. 16, no. 4, pp. 221–223, 2006.
- [73] X. Gu, L. Tsang, and H. Braunisch, "Modeling effects of random rough interface on power absorption between dielectric and conductive medium in 3-d problem," *Microwave Theory and Techniques, IEEE Transactions on*, vol. 55, no. 3, pp. 511–517, 2007.
- [74] H. Braunisch, X. Gu, A. Camacho-Bragado, and L. Tsang, "Off-chip rough-metal-surface propagation loss modeling and correlation with measurements," in *Proc. Electronic Comp. and Tech. Conf.*, 2007, pp. 785–791.
- [75] X. Gu, L. Tsang, and H. Braunisch, "Estimation of roughness-induced power absorption from measured surface profile data," *IEEE Microw. and Wireless Comp. Letters*, vol. 17, no. 7, pp. 486–488, 2007.
- [76] L. Tsang, H. Braunisch, R. Ding, and X. Gu, "Random rough surface effects on wave propagation in interconnects," *IEEE Trans. Advanced Packaging*, vol. 33, no. 4, pp. 839–856, 2010.
- [77] R. Ding, L. Tsang, H. Braunisch, and W. Chang, "Wave propagation in parallel plate metallic waveguide with finite conductivity and three-dimensional roughness," *IEEE Trans. Ant. and Prop.*, vol. 60, no. 12, pp. 5867–5880, 2012.
- [78] A. Alù and N. Engheta, "Effect of small random disorders and imperfections on the performance of arrays of plasmonic nanoparticles," *New Journal of Physics*, vol. 12, no. 1, 2010.
- [79] P. W. Anderson, "Absence of diffusion in certain random lattices," *Physical Review*, vol. 109, no. 5, pp. 1492–1505, Mar. 1958.
- [80] G. Kissel, "Localization in disordered periodic structures," Ph.D. dissertation, Mass. Inst. Technol., Cambridge, 1988.
- [81] G. J. Kissel, "Localization and the invariant probability measure for a structural dynamic system," *Int. Symp. Smart Struct. and Mat. & Nondestructive Evaluation and Health Monitoring*, vol. 7286, no. 1, April 2009.
- [82] G. Cai and Y. Lin, "Localization of wave propagation in disordered periodic structures," *AIAA J.*, vol. 29, no. 3, pp. 450–456, Mar. 1991.
- [83] J. Ochoa and A. Cangellaris, "Analysis of the impact of statistical variations on transmission-line based metamaterial structures," in *Proc. Eur. Microw. Symp.*, September 2010, pp. 1397–1400.

- [84] K. V. Mardia, J. T. Kent, and J. M. Bibby, *Multivariate Analysis*. London: Academic Press, 1979.
- [85] Y. Zhu and A. Cangellaris, *Multigrid Finite Element Methods for Electromagnetic Field Modeling*. Hoboken, New Jersey: Wiley & Sons, Inc., 2006.
- [86] P. Sumant, H. Wu, A. Cangellaris, and N. Aluru, “Reduced-order models of finite element approximations of electromagnetic devices exhibiting statistical variability,” *IEEE Trans. Ant. and Prop.*, vol. 60, no. 1, pp. 301–309, 2012.
- [87] P. Sumant, H. Wu, A. Cangellaris, and N. Aluru, “A sparse grid based collocation method for model order reduction of finite element approximations of passive electromagnetic devices under uncertainty,” in *Proc. Int. Microw. Symp.*, 2010, pp. 1652–1655.
- [88] N. Agarwal and N. Aluru, “Stochastic analysis of electrostatic MEMS subjected to parameter variations,” *J. Microelectromechanical Systems*, vol. 18, no. 6, pp. 1454–1468, Dec. 2009.
- [89] E. Novak and K. Ritter, “High dimensional integration of smooth functions over cubes,” *Numerische Mathematik*, vol. 75, pp. 79–97, 1996.
- [90] Z. Zeng and J.-M. Jin, “An efficient quantification of scattering variation due to uncertain geometrical deviation,” in *Proc. Ant. and Prop. Soc. Int. Symp.*, 2007, pp. 4805–4808.
- [91] J. Jin, *The Finite Element Method in Electromagnetics*. New York: John Wiley & Sons, Inc., 2002.
- [92] T. El-Moselhy and L. Daniel, “Variation-aware interconnect extraction using statistical moment preserving model order reduction,” in *Proc. Design, Automation & Test Conference*. IEEE, 2010, pp. 453–458.
- [93] J. Carroll, K. Whelan, S. Pritchett, and D. Bridges, “FET parameter orthogonalization with principal components,” in *Proc. Int. Microw. Symp.*, 1994, pp. 409–412.
- [94] J. Swidzinski and K. Chang, “Nonlinear statistical modeling and yield estimation technique for use in Monte Carlo simulations [microwave devices and ICs],” *IEEE Trans. Microwave Theory Tech.*, vol. 48, no. 12, pp. 2316–2324, 2000.
- [95] J. Ochoa and A. Cangellaris, “Random-space dimensionality reduction scheme for expedient analysis of microwave structures with manufacturing variability,” in *Proc Int. Microw. Symp.*, 2013.

- [96] J. Ochoa and A. Cangellaris, “Random-space dimensionality reduction for expedient yield estimation of passive microwave structures,” *Submitted to IEEE Trans. Microwave Theory Tech.*, 2013.
- [97] P.-T. De Boer, D. P. Kroese, S. Mannor, and R. Y. Rubinstein, “A tutorial on the cross-entropy method,” *Annals of Operations Research*, vol. 134, no. 1, pp. 19–67, 2005.
- [98] S. Asmussen, P. Dupuis, R. Rubinstein, and H. Wang, “Importance sampling for rare events,” Aarhus University, Aarhus, Tech. Rep., 2011.
- [99] D. P. Kroese, “Cross-entropy method,” *Wiley Encyclopedia of Operations Research and Management Science*, 2011.
- [100] ANSYS, “Q3D extractor,” Release 14.0.
- [101] J. S. Ochoa and A. C. Cangellaris, “Macro-modeling of electromagnetic domains exhibiting geometric and material uncertainty,” *Applied Comp. Electromag. Soc. J.*, vol. 27, no. 2, pp. 80–87, 2012.
- [102] H. Bagci, A. Yucel, J. Hesthaven, and E. Michielssen, “A fast Stroud-based collocation method for statistically characterizing EMI/EMC phenomena on complex platforms,” *IEEE Trans. Electromag. Compatibility*, vol. 51, no. 2, pp. 301–311, 2009.
- [103] A. Yucel, H. Bagci, and E. Michielssen, “Efficient stochastic EMC/EMI analysis using HDMR-generated surrogate models,” in *Proc. General Assembly and Scientific Symp. URSI*. IEEE, Aug. 2011, pp. 1–4.
- [104] W. C. Chew, *Waves and Fields in Inhomogeneous Media*. New York: IEEE Press, 1995.
- [105] K. Petras, “Smolyak cubature of given polynomial degree with few nodes for increasing dimension,” *Numerische Mathematik*, vol. 93, no. 4, pp. 729–753, 2003.
- [106] S. K. Chang and K. Mei, “Application of the unimoment method to electromagnetic scattering of dielectric cylinders,” *IEEE Trans. Ant. and Prop.*, vol. 24, no. 1, pp. 35–42, Jan. 1976.
- [107] W. Chew, “An N2 algorithm for the multiple scattering solution of N scatterers,” *Microwave and Optical Technology Letters*, vol. 2, no. 11, pp. 380–383, 1989.
- [108] H. Wu, “Methodologies and algorithms for finite element analysis of electromagnetic devices and systems,” Ph.D. dissertation, University of Illinois at Urbana-Champaign, Urbana, IL, 2007.

- [109] C. A. Balanis, *Advanced Engineering Electromagnetics*. New York: Wiley, 1989, vol. 205.
- [110] J. Chung, “Efficient and physically consistent electromagnetic macro-modeling of high-speed interconnects exhibiting geometric uncertainties,” Ph.D. dissertation, University of Illinois at Urbana-Champaign, Urbana, IL, 2013.
- [111] J. S. Ochoa and A. C. Cangellaris, “Homogenization technique for transmission lines with random permittivity profiles,” in *Proc. Workshop on Signal and Power Integrity*, 2013, pp. 1–4.
- [112] J. S. Ochoa and A. C. Cangellaris, “Fast analysis of the impact of interconnect routing variability on signal degradation,” in *Proc. Electrical Perform. Electronic Pack. and Syst.* IEEE, 2012, pp. 315–318.
- [113] S. Yamamoto, T. Azakami, and K. Itakura, “Coupled nonuniform transmission line and its applications,” *IEEE Trans. Microwave Theory Tech.*, vol. 15, no. 4, pp. 220–231, April 1967.
- [114] H. Furstenberg, “Noncommuting random products,” *Trans. American Math. Society*, vol. 108, no. 3, pp. 377–428, 1963.
- [115] R. E. Collin, *Foundations for Microwave Engineering*. New York: McGraw-Hill, Inc., 1992.
- [116] J. Schutt-Aine, P. Goh, Y. Mekonnen, J. Tan, F. Al-Hawari, P. Liu, and W. Dai, “Comparative study of convolution and order reduction techniques for blackbox macromodeling using scattering parameters,” *IEEE Trans. Comp. Pack. Manufact. Tech.*, vol. 1, no. 10, pp. 1642–1650, Oct. 2011.
- [117] B. Gustavsen and A. Semlyen, “Rational approximation of frequency domain responses by vector fitting,” *IEEE Trans. Power Delivery*, vol. 14, no. 3, pp. 1052–1061, July 1999.
- [118] F. Rütting, “Plasmons in disordered nanoparticle chains: Localization and transport,” *Physical Review B*, vol. 83, no. 11, p. 115447, 2011.
- [119] “Wave3D,” CEMWorks, 2013. [Online]. Available: <https://www.cemworks.com>
- [120] V. I. Okhmatovski, J. Morsey, and A. C. Cangellaris, “On deembedding of port discontinuities in full-wave cad models of multiport circuits,” *IEEE Trans. Microwave Theory Tech.*, vol. 51, no. 12, pp. 2355–2365, 2003.

- [121] C. Pierre, “Weak and strong vibration localization in disordered structures: A statistical investigation,” *Journal of Sound and Vibration*, vol. 139, no. 1, pp. 111–132, May 1990.
- [122] J. Ochoa and A. Cangellaris, “Expedient electromagnetic analysis of the impact of statistical disorder in periodic waveguides,” *IEEE Trans. Microwave Theory Tech.*, vol. 60, no. 12, December 2012.
- [123] J. Ochoa and A. Cangellaris, “A methodology for expedient analysis of the impact of disorder in periodic waveguides,” in *Proc Int. Microw. Symp.*, June 2012, pp. 1–3.
- [124] Z. I. Botev, “Nonparametric density estimation via diffusion mixing,” The University of Queensland, Tech. Rep., Nov. 2007. [Online]. Available: <http://espace.library.uq.edu.au/view/UQ:120006>
- [125] Z. I. Botev, J. F. Grotowski, and D. P. Kroese, “Kernel density estimation via diffusion,” *Ann. Statist.*, vol. 38, no. 5, pp. 2916–2957, 2010.
- [126] N. Agarwal and N. R. Aluru, “A data-driven stochastic collocation approach for uncertainty quantification in MEMS,” *Int. J. Numer. Methods Eng.*, vol. 83, pp. 575–597, Mar. 2010.
- [127] A. Alwan and N. Aluru, “Uncertainty quantification of MEMS using a data-dependent adaptive stochastic collocation method,” *Comput. Methods Appl. Mech. Eng.*, vol. 200, pp. 3169–3182, 2011.
- [128] R. Duin, “On the choice of smoothing parameters for Parzen estimators of probability density functions,” *IEEE Tran. on Computers*, vol. C-25, no. 11, pp. 1175–1179, Nov. 1976.
- [129] J. Karhunen and J. Joutsensalo, “Representation and separation of signals using nonlinear PCA type learning,” *Neural Networks*, vol. 7, no. 1, pp. 113–127, 1994.
- [130] E. Oja, “The nonlinear PCA learning rule in independent component analysis,” *Neurocomputing*, vol. 17, no. 1, pp. 25–45, 1997.
- [131] L. Simonovich, “Practical fiber weave effect modeling,” LAMSIM Enterprises Inc., White paper 3, Feb. 2012.